



Escola de Camins
Escola Tècnica Superior d'Enginyeria de Camins, Canals i Ports
UPC BARCELONATECH

**An experimental and numerical
study on the cyclic response of
austenitic stainless steel.**

Treball realitzat per:

Mauricio Daniel De Marco

Dirigit per:

Rolando Chacón

Esther Real Saladrigas

Màster en:

Enginyeria Estructural i de la Construcció

Barcelona, **maig 2018**

Departament d' Enginyeria Civil i Ambiental

TREBALL FINAL DE MÀSTER

Abstract

Stainless steel is a metal alloy that is being used more often in the construction industry thanks to its corrosion and heat resistance which allows it to withstand highly aggressive and corrosive environments. However, the chromium content that is responsible for the corrosion resistance, also modifies its mechanical behaviour resulting in a non-linear material. The lack of information, its high unitary price and its non-linearity, reduce the confidence in using stainless steel as a structural material and encourage conservative designs.

The main objective of this work consists of understanding the cyclic behaviour and low-cycle fatigue of grade 1.4301 austenitic stainless steel in order to introduce it to earthquake-resistant structures. Experimental tests and numerical models were performed.

The tests performed were low-cycle fatigue tests at strain amplitudes ranging from $\pm 0.5\%$ to $\pm 5\%$, and the numerical models were executed in the general-purpose Software Abaqus using combined isotropic/kinematic hardening model based on the Chaboche model.

Analytical parameters that establish the Chaboche model were obtained from the tests data and proposed for further research.

Acknowledgements

First of all, I am grateful to my tutors, Rolando Chacón and Esther Real, who have supported me throughout this research project with their knowledge and guidance. Their contributions are sincerely appreciated and gratefully acknowledged. Without them, this master's thesis would not have been possible.

I also thank Itsaso Arrayago for her incredible support in all possible ways. Her contributions were exceptionally important and much appreciated.

I offer my gratitude to all the laboratory technicians, particularly to Carlos and Jordi. Their aid was key to the correct and safe execution of the tests. I also thank Miguel Angel for all his help.

Especial thanks to my parents, Cristina and Pietro, for all their wisdom and guidance; and to Mafe for her patience and support throughout this research project.

Finally, I want to thank Acerinox and Roldan for providing the coupons and the UPC for giving me this opportunity.

This work was developed in the frame of the Project BIA2016-75678-R, AEI/FEDER, UE "Comportamiento estructural de pórticos de acero inoxidable. Seguridad frente a acciones accidentales de sismo y fuego", funded from the MINECO (Spain).

Index

1. INTRODUCTION AND OBJECTIVES	9
1.1. Introduction	9
1.2. Objectives	10
1.3. General objective	10
1.4. Specific objectives	10
1.5. Content of work	10
2. LITERATURE REVIEW	12
2.1. Stainless steel	12
2.1.1. Types of stainless steels	12
2.1.2. Life cycle cost and environmental impact	14
2.1.3. Examples of structural applications	15
2.1.4. Material response	16
2.1.5. Material models	18
2.1.6. Stainless steel standards and guidelines	21
2.2. Cyclic plasticity	22
2.2.1. Strain Hardening	22
2.2.2. Bauschinger Effect	23
2.2.3. Isotropic and kinematic hardening	24
2.2.4. Low-cycle fatigue (LCF) and Cyclic Stress-Strain Curve	25
2.2.5. Ratcheting	28
2.3. Previous studies about cyclic plasticity in stainless steel	28
3. NUMERICAL MODELLING	32
3.1. A brief introduction to the finite element method (FEM)	32
3.2. Software	32
3.3. Modelling Specifications	33
3.4. Obtaining the results	38
4. EXPERIMENTAL TEST	39
4.1. Coupon Design	39
4.2. Instrumentation	46
4.3. Test set up	50
4.3.1. Graphical user interface (GUI) of the testing machine software	55
4.3.2. Loading protocols	55
5. EXPERIMENTAL RESULTS	58
5.1. Test results	58
5.2. Results discussion	71

5.3.	Cyclic stress-strain curve	72
5.4.	Young's modulus and proof stress	72
5.5.	The Ramberg-Osgood parameters and Mirambell-Real two-stage model.....	73
5.5.1.	Combined isotropic/kinematic hardening model	74
6.	NUMERICAL TEST SIMULATION.....	82
6.1.	Material properties	82
6.3.	Correlation between FE models and experimental tests.....	91
6.4.	Results discussion	98
7.	CONCLUSIONS AND RECOMMENDATIONS.....	99
7.1.	Conclusions	99
7.2.	Recommendations for future research.....	100
	References.....	101

1. INTRODUCTION AND OBJECTIVES

1.1. Introduction

Stainless steel is a kind of a corrosion and heat-resistant steel that comes from an alloy of iron with a minimum of 10.5% of chromium [1]. Although this alloy was first implemented in applications like culinary equipment in the early 1910s, it wasn't long before it was used as a structural material. This alloy is attractive in the construction industry due to its low maintenance requirements, aesthetics, recyclability, favourable strength, high ductility and the mentioned corrosion and heat resistance [1]; as a result, its use is continuously increasing, despite its high cost.

There are five different families of stainless steel, namely austenitic, duplex, ferritic, martensitic and precipitation hardening. Austenitic and duplex stainless steels are the most commonly used for structural application; these two families exhibit high corrosion resistance, high strength and ductility which makes them suitable for seismic applications. Hence, it is important to study their behaviour thoroughly, in order to implement it efficiently and reduce costs.

The corrosion resistance property of stainless steel is attributed to the percentage of chromium, but this component also modifies its structural behaviour resulting in a non-linear material. As a result of its complex behaviour and its relatively new appearance in construction, stainless steel as a structural material, has several uncertainties. A particular uncertain behaviour, and main subject of this study, is the inelastic response of austenitic stainless steel when subjected to periodic load i.e. the cyclic plasticity of austenitic stainless steel. This problem limits the potential of exploiting the high ductility of stainless steel in earthquake-resistant structures.

When a structure suffers periodic loads such as the ones resulting from earthquakes, its structural members may experience very large displacement cycles and their response is controlled by their geometry and by the hysteretic behaviour of the material [2] [3]. Also, these displacements create inelastic deformations that lead to non-linear and cyclic plasticity models which are complex to recreate. Therefore, in order to introduce austenitic stainless steel in earthquake-resistant structures, it is necessary to understand its cyclic behaviour and determine the structural performance of structural members made of this alloy.

In this research project, Low-cycle fatigue tests will be carried out to study the properties of 1.4301 austenitic stainless steel and subsequently, a parameter correlation of the constitutive model for cyclic plasticity of stainless steel and numerical models will be established. For this reason, the finite element software Abaqus is employed. Abaqus supports the input of several parameters that define the plastic behaviour of the material including cyclic behaviour; these parameters, along with the experimental tests, will be compared and studied.

1.2. Objectives

The main objectives of this work consist of understanding the behaviour of stainless steel subjected to large displacement cycles. These displacement cycles may be present in a structure during an earthquake, therefore this study helps to the introduction of stainless steel structures under seismic events. The objectives are subdivided into general and specific objectives.

1.3. General objective

This study has been focused towards the general objective of understanding the cyclic behaviour and low-cycle fatigue of austenitic stainless steel by performing experimental tests that describe the cyclic plasticity of this material and identifying an analytical model that adequately simulates the strain hardening and the Bauschinger effect in this highly nonlinear material.

1.4. Specific objectives

- Obtain the stainless steel mechanical properties by performing a monotonic tensile test of a round coupon.
- Define the optimal cyclic tests typology for this study.
- Perform Low-cycle fatigue tests.
- Understand the procedure for obtaining data from tests used in the analytical model and in numerical simulations.
- Perform numerical finite element models using ABAQUS software.
- Establish a comparison between the experimental data and the numerical results.
- Calibrate parameters for the most appropriate analytical model previously identified.

1.5. Content of work

In this first chapter, a brief introduction about the research project along with the objectives is presented.

In chapter 2, a brief review of the literature is presented. Starting with a description of stainless steel as a material emphasizing on its mechanical response. Material models for monotonic behaviour and for cyclic behaviour are exhibited. And finally, a compilation of previous studies about cyclic behaviour of stainless steel is provided.

Chapter 3 summarizes information about the finite element method (FEM) and a description about the analyses conducted in this project using the computer software ABAQUS-Simulia.

Chapter 4 contains all the information regarding the experimental tests. First a coupon design is made to prevent buckling when subjected to compression, then the equipment and test set up are described along with the loading protocols, formerly a description of each test is presented and finally, the results are shown.

In chapter 5 the experimental results are analysed and formerly, relevant information and properties are extracted.

In chapter 6 the numerical models using test data are made and compared with the experimental tests. First, the material input is described and then, a comparison between FEM and experimental test is performed.

Conclusions, recommendations and possible areas for future research are presented in chapter 7.

2. LITERATURE REVIEW

2.1. Stainless steel

Stainless steel is an alloy resulting from the mixture of mostly iron and a minimum of 10.5% chromium. When exposed to oxygen, the chromium forms a self-repairing chromium-rich thin oxide surface, protecting the steel from additional interaction with an oxidising agent and hence, attributing its corrosion resistance property. This layer is known as “passive film”, is stable and non-porous, with a thickness of approximately 5×10^{-6} mm [1]. As a result, stainless steel is a highly attractive structural material mainly because it overcomes the carbon steel foremost weakness i.e. corrosion.

There are other major alloying elements like Nickel, Copper, Molybdenum and Titanium; that modifies some mechanical and physical properties generating a family of stainless steels. These modifications can produce an alloy more weldable, formable and tough, can improve resistance to chlorides, improve strength, corrosion resistance, high-temperature performance as well as other properties. This family of stainless steels is categorized into five groups: austenitic, duplex, ferritic, martensitic and precipitation hardening.

Each group of stainless steel adjusts to different applications and requirements. In most cases, corrosion resistance is a key factor to determine a stainless steel group, followed by service life and the capacity to tolerate crevice, pitting, abrasion and intergranular corrosion.

2.1.1. Types of stainless steels

Stainless steels are classified into five basic groups according to their metallurgical structure: austenitic, ferritic, martensitic, duplex and precipitation-hardening [1]. In figure 1 it is possible to identify the content of chromium and nickel for each type of stainless steel, in the case of austenitic stainless steel, it is clearly the type with the highest nickel content, this being the main reason for its high price.

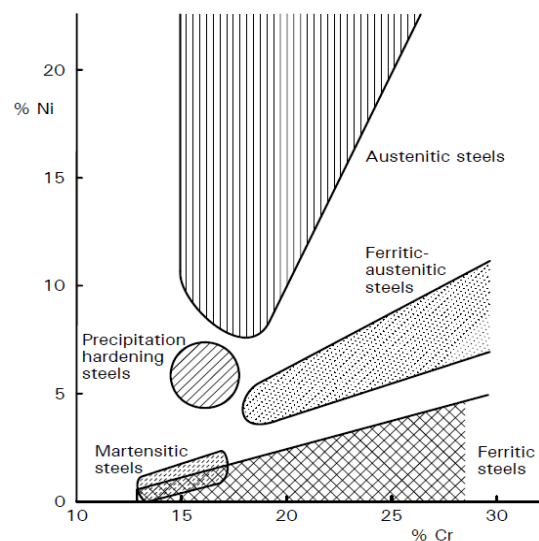


Fig. 1. Classification of stainless steels according to nickel and chromium content [4].

Each type has different properties and their corrosion resistance varies from one to another. Some of them are ideal for structures in a specific environment and some are not appropriate for structural applications, especially when welding is expected. Each type is separated into branches and categorised by grades.

Austenitic stainless steels

These stainless steels, as well as duplex stainless steels, are the most commonly used. They have a chromium content of 17 to 18%, a nickel content between 8 and 11% and an austenitic microstructure at room temperature (which means that the crystal structure is a face-centred cubic system rather than a body-centred cubic system present in the ferritic crystal structure of carbon steels). They offer high ductility in a wide temperature range, non-magnetic properties, impact resistance, heat resistance, favourable forming properties and weldability in addition to their good corrosion resistance. In general, austenitic stainless steels have greater corrosion resistance than ferritic and martensitic stainless steels; and similar to duplex stainless steel. Their strength is fairly good and it can only be hardened by cold-working. [1]

The most common standard austenitic grades are 1.4301 and 1.4401 (also known as 304 and 316 in ASTM standards), these grades also come in low carbon versions: 1.4307 and 1.4404 (304L and 316L respectively). Other relevant grades are the austenitic stainless steels: 1.4541 and 1.4571. They contain around 17 to 19.5% chromium, 8 to 13.5% nickel [5]. Grade 1.4301 is suitable for rural, urban and light industrial sites, grade 1.4401 for marine and industrial sites, low carbon grades and the stabilised grades are used when corrosion performance is important in welded members. [1]

Ferritic stainless steels

These materials have a ferritic microstructure (body-centred cubic crystal system) and relatively low cost due to low nickel content. Ductility, strength, formability and weldability are inferior to those of austenitic steels. They are magnetic, prone to become brittle at low temperatures, their strength can only be increased by cold working, they have very good cold forming properties and, unlike austenitic stainless steels, they are insensitive to stress corrosion cracking. Ferritic stainless steels offer an adequate performance/cost ratio for several applications and therefore their use is increasing. [1]

Grades 1.4003, 1.4016 and 1.4512 are the only ones classified as structural stainless steels in EN 1993-1-4 [6]. Both grades 1.4003 and 1.4512 contain around 10.5 to 12.5% chromium and less than 0.03% carbon, but grade 1.4003 contains 0.3 to 1% Nickel whilst grade 1.4512 lacks Nickel. Grade 1.4016 has 16 to 18% chromium less than 0.08% carbon and no Nickel [5]. The low content of nickel makes ferritic stainless steels available at a lower and more stable market price and, adding the fact that they have a higher resistance than austenitic steels, it can be said that ferritic stainless steels are an attractive alternative for many applications. [1]

Martensitic stainless steels

Martensitic steels are formed from austenite during heat treatment or by cold working. They are magnetic and show high strength. Traditional martensitic steels made with 0.08% to 1% Carbon are air hardened, but may be strengthened by a quenching heat treatment; their ductility is good, but have limitations when welding. [1]

These materials are not normally used due to their difficulty to weld, they offer high strength but in other properties, they are inferior to other stainless steels. [1]

Duplex stainless steels

Austenitic-ferritic stainless steel often known as Duplex, have a well-balanced mixed microstructure and a combination of austenitic and ferritic stainless steels properties. They typically have a chromium content between 20 to 26%, a nickel content from 1 to 8%, 0.05 to 5% of molybdenum and between 0.05 and 0.3% of nitrogen. Compared to austenitic stainless steels, duplex stainless steels have higher strength properties and similar weldability, need higher power for cold deformation and show higher resistance to stress corrosion cracking. They may be hardened by cold working. [1]

Duplex stainless steels are one of the most commonly used due to their combination of the best of the properties of austenitic and ferritic groups. In the EN 1993-1-4 [6], there are only two grades listed: 1.4462 and 1.4362.

Precipitation-hardening stainless steels

Precipitation-hardening stainless steels can acquire three different microstructure groups, namely martensitic, semi-austenitic and austenitic. They can be strengthened by a heat treatment and their corrosion resistance is similar to that of austenitic stainless steels, with around 18% of chromium and 8% nickel. They are commonly used in aerospace industry. [1]

2.1.2. Life-cycle cost and environmental impact

Selecting a corrosion-resistant material in the construction industry is very determinant in a matter of life cycle cost, mainly because future maintenance could be avoided and costs associated with element replacement and downtime can also be reduced. Stainless steels represent a high initial cost but may result in a lower life-cycle cost. [1]

Structural stainless steel, in comparison with carbon steel, has a considerably higher cost, although there can be initial cost savings associated with corrosion-resistant and fire-resistant coatings, and with the reduction of material weight if using high strength stainless steel. With the lack of coatings and the corrosion resistance, stainless steel highly reduces the cost of maintenance and the inspection frequency.

Stainless steel recycling ratio is around 80% [7], and it has a high value at the end of the structure life (scrap value). This means that most of the structural material can be

recycled which results in a low environmental impact compared to other structural materials. Nevertheless, scrap availability is limited due to the material high service life and relatively recent appearance in the construction industry [1].

2.1.3. Examples of structural applications

Stainless steels have several applications in the construction industry, but most of them involve facades, roofs, decorations or plumbing. In this section, some of the stainless steel applications that involve structural members will be described.

It is appropriate to start with the first stainless steel road bridge in Europe [8]. The Cala Galdana Bridge (see fig. 2) is a 55m span bridge built in Menorca in 2005 with the purpose of replacing the existing reinforced concrete bridge that was significantly deteriorated by the marine atmosphere. Different grades of carbon steel and stainless steel were considered and Duplex stainless steel was eventually selected for the structure.



Fig. 2. Cala Galdana Bridge, Final phase (left), construction phase (right). [8]

Besides the Cala Galdana Bridge, there are more stainless steel bridges in Spain, like Sant Fruitos Pedestrian Bridge (Catalonia) and Padre Arrupe Bridge (Bilbao).

Another structural application of stainless steel is the Aeration building in the Edmonton Composting Facility (Canada). This building is the largest stainless steel building in North America (23000m²) and it is made of austenitic stainless steel grade 1.4301. [9]

The Station Sint Pieters in Ghent (Belgium), exhibit a glass roof held by a stainless steel structure at its gate (see fig. 3).



Fig. 3. Sint Pieters Station transparent roof [7].

There are also important buildings that have stainless steels as part of the structure: La Grande Arche and La Lentille de Saint-Lazare, Paris (France) (see fig.4), Torno Internazionale S.P.A. Headquarters, Milan (Italia), among others.

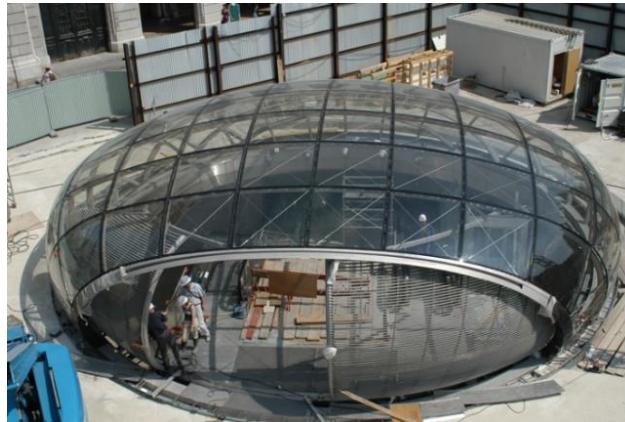


Fig. 4. La Lentille de Saint-Lazare. [7]

2.1.4. Material response

Unlike carbon steel, stainless steels have a rounded stress-strain curve with no plateau and with no well-defined yield point [1]. In fig. 5 and fig. 6, a comparison of stress-strain characteristics between various stainless steels and carbon steel is shown. Another significant difference between these materials is that stainless steel exhibits a considerable strain hardening and high ductility, this means that it is able to absorb impact without fracturing and reach strains of 40-60% at fracture [10]. Also, it presents an anisotropic behaviour, therefore their mechanical response varies depending on the rolling direction.

A “yield” point in non-linear materials such as stainless steel is generally determined as a proof strength for a particular offset permanent strain; in the case of stainless steel, the yield point is conventionally the proof stress for a 0.2% offset strain [1].

It is worth pointing out that, compared to carbon steels, the metallurgy of stainless steels is more complex and the manufacturing process has a higher impact on their final properties [1]. Therefore, there are factors that affect the stress-strain behaviour: Cold working which enhances the strength levels of stainless steel and Strain-rate sensitivity which means that a greater strength can be realised at fast strain rates.

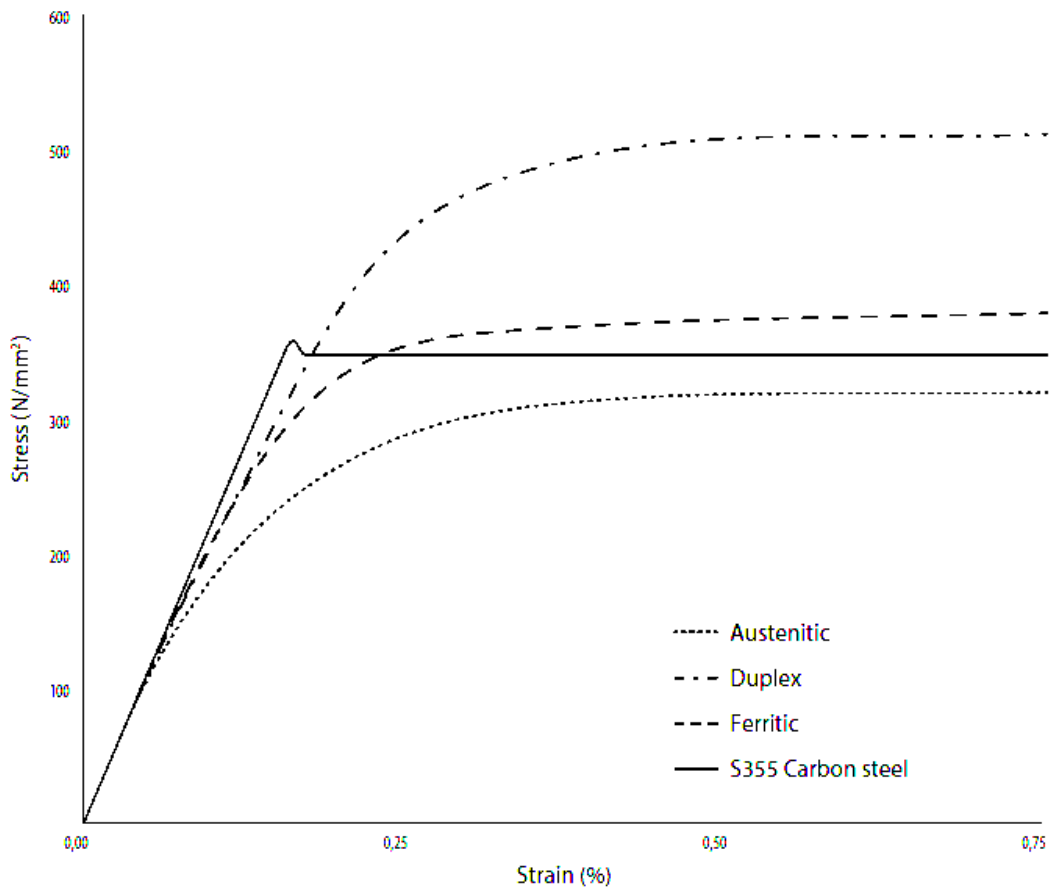


Fig. 5. Stress-strain curves for stainless steel and carbon steel from 0 to 0,75 % strain [1].

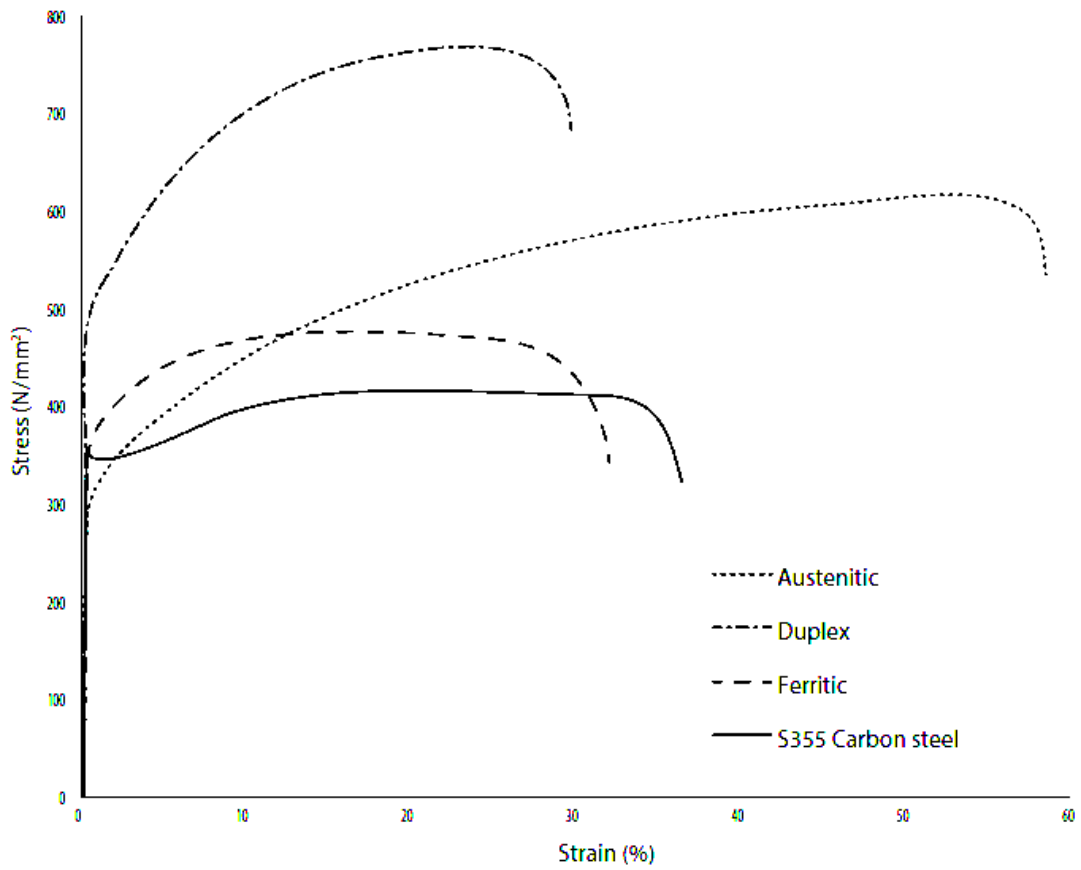


Fig. 6. Full range stress-strain curves for stainless steel and carbon steel [1].

There have been several researchers that have made experimental studies and numerical analyses in order to develop models to simulate the non-linear behaviour of stainless steel. In the following section, a brief description of these models and analytical expression is presented.

2.1.5. Material models

Monotonic response

As a difference from carbon steels, stainless steel alloys presents a non-linear stress-strain behaviour, this requires more complex material model than the bilinear model that rules carbon steels. In the last decades, several material models have been developed starting with the general Ramberg-Osgood proposal [11]. These models are built from parameters obtained from experimental tests and their objective is to provide a safe and accurate representation of the material behaviour in order to better comprehend its non-linear nature.

The Ramberg-Osgood expression was modified by Hill [12] as given in Eq. (1), where E is Young's modulus, $\sigma_{0.2}$ is the 0.2% proof stress and n is a strain hardening exponent that characterizes the roundedness of the stress-strain curve [10].

The Ramberg-Osgood formulation is able to accurately represent the stress-strain curve of the material until the 0.2% proof stress, however it has been shown to be unable to accurately represent the whole curve with a single value on n . Due to this, two-stage Ramberg-Osgood models have been developed to provide a continuous representation of the complete stress-strain curve of stainless steel. Mirambell and Real [13] proposed a two-stage model defining a second curve for stresses above the 0.2% proof stress, this curve is given by Eq. (2) where $E_{0.2}$ is the tangent modulus at 0.2% proof stress, σ_u and ε_u are the ultimate strength and strain, $\varepsilon_{0.2}$ is the total strain at 0.2% proof stress, and m is an additional parameter that characterizes the roundedness of the second stage [10].

$$\varepsilon = \frac{\sigma}{E} + 0.002 \left(\frac{\sigma}{\sigma_{0.2}} \right)^n \quad \text{for } \sigma \leq \sigma_{0.2} \quad (1)$$

$$\varepsilon = \frac{\sigma - \sigma_{0.2}}{E_{0.2}} + \left(\varepsilon_u - \varepsilon_{0.2} - \frac{\sigma_u - \sigma_{0.2}}{E_{0.2}} \right) * \left(\frac{\sigma - \sigma_{0.2}}{\sigma_u - \sigma_{0.2}} \right)^m + \varepsilon_{0.2} \quad \text{for } \sigma \geq \sigma_{0.2} \quad (2)$$

This model was later simplified by Rasmussen [14] reducing the input parameters in the second stage of the model producing a new expression given in Eq. (3) and also developing expressions to determine the parameter m , the ultimate strain and strength (σ_u and ε_u). With this simplification, the only input parameters required to apply the model are the basic Ramberg-Osgood parameters i.e. Young's modulus (E), 0.2% proof stress ($\sigma_{0.2}$) and n . This proposal was included in EN 1993-1-4, Annex C for the modelling of stainless steel material behaviour.

$$\varepsilon = 0.002 + \frac{\sigma_{0.2}}{E} + \frac{\sigma - \sigma_{0.2}}{E_y} + \varepsilon_u * \left(\frac{\sigma - \sigma_{0.2}}{\sigma_u - \sigma_{0.2}} \right)^m \quad \text{for } \sigma_{0.2} < \sigma \leq \sigma_u \quad (3)$$

Cyclic response

For cyclic behaviour, a material model capable of simulating cyclic material properties such as the Baushinger effect and expansion of the yield surface representation is needed. In the literature and in previous studies, it is shown that defining the characteristics of the material by a combined isotropic/kinematic hardening using the Chaboche model [15] proves adequate to fulfil these criteria.

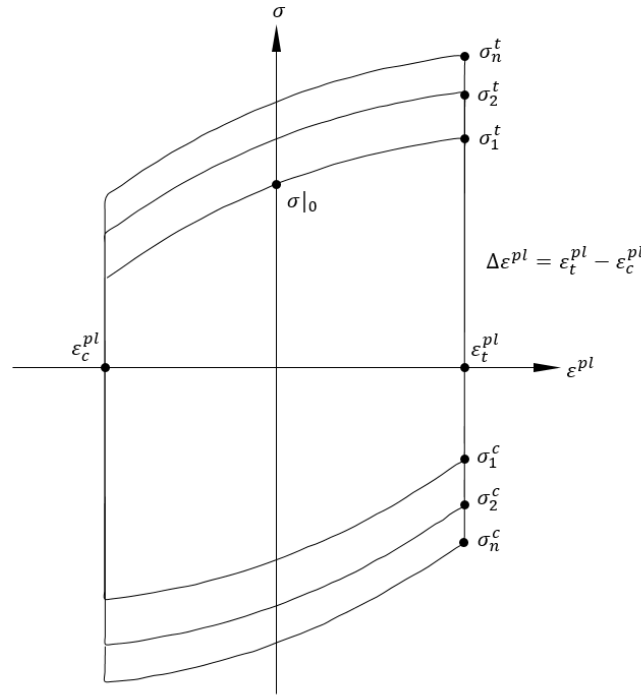


Fig. 7. Calibration of isotropic hardening component. [16]

The model consists of a non-linear kinematic hardening component and an isotropic hardening component. The **isotropic** hardening behaviour defines the evolution of the yield surface size (σ^0), as a function of the equivalent plastic strain (ε^p), given in Eq. (4) where $\sigma|_0$ is the yield stress at zero plastic strain and (defined in this study as 0.2% proof stress), Q_∞ is the maximum change in the size of the yield surface and b is a parameter that defines the rate at which the size of the yield surface changes as plastic straining increases.

When the equivalent stress defining the size of the yield surface remains constant ($\sigma^0 = \sigma|_0$), the model reduces to a nonlinear kinematic hardening model. [16]

$$\sigma^0 = \sigma|_0 + Q_\infty(1 - e^{-b\varepsilon^p}) \quad (4)$$

The size of the yielding surface σ_i^0 and the plastic strain ε_i^p in i^{th} cycle are defined by Eq.(5) and Eq.(6), respectively. Where σ_i^t is the maximum tensile stress and σ_i^c is the

maximum compressive stress in the elastic range as shown in the figure 7. $\Delta\varepsilon^p$ is the plastic strain which is defined according to Eq. (7).

$$\sigma_i^0 = (\sigma_i^t - \sigma_i^c)/2 \quad (5)$$

$$\varepsilon_i^p = \frac{1}{2}(4i - 3)\Delta\varepsilon^p \quad (6)$$

$$\Delta\varepsilon^p \approx \Delta\varepsilon - 2\sigma_1^t/E \quad (7)$$

A series of $(\sigma_i^0, \varepsilon_i^p)$ data values are used in the model to obtain the parameters Q_∞ and b . The simplest way to obtain these data is from a stabilized loop from a symmetric strain-controlled cyclic experiment [16]. A stabilized cycle or loop means that the material reached steady-state condition

It is important to mention that in order to obtain representative cyclic hardening data, the calibration experiment should be performed at a strain range, $\Delta\varepsilon$, that corresponds to the strain range anticipated in the analysis because the material model does not predict different isotropic hardening behaviour at different strain ranges. [16]

The change of backstress α is defined according to the **kinematic** component of the model shown in Eq. (8), where C_k and γ_k are constants that can be calibrated by test data from a stabilised cycle. C_k is the initial kinematic hardening modulus and γ_k determine the rate at which the kinematic hardening moduli decrease with increasing plastic deformation. The ratio C_k/γ_k is the maximum variation in backstresses. A backstress is the stress coordinate of a point midway between the yield stress in tension and the yield stress compression.

$$\alpha = \frac{C_k}{\gamma_k}(1 - e^{-\gamma\varepsilon^p}) + \alpha_1 e^{-\gamma\varepsilon^p} \quad (8)$$

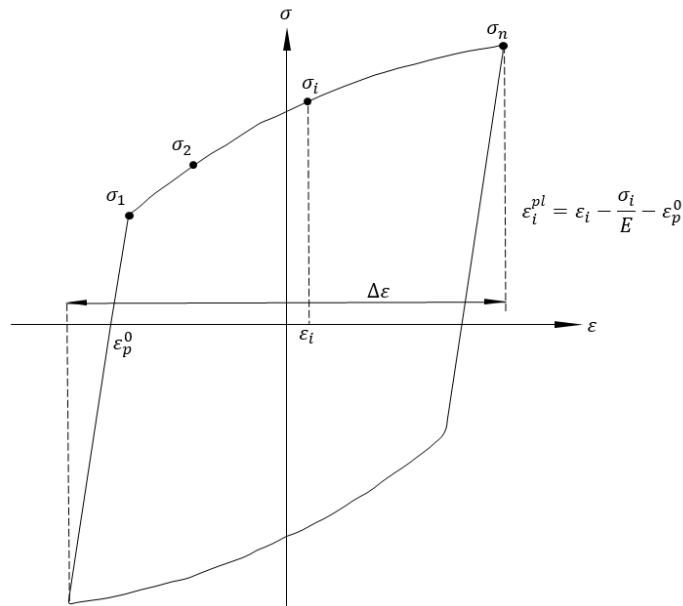


Fig. 8. Calibration of kinematic hardening component. [16]

Each data pair $(\sigma_i^0, \varepsilon_i^p)$ is obtained from test data. The plastic strain ε_i^p is defined as Eq. (9), where ε_p^0 is the strain when the curves intercept with the strain axis, $\varepsilon_1^p = 0$. α_i can be obtained as Eq. (10), where σ^s is the average of the first and last data points, σ_1 and σ_n respectively, in a stabilised cycle, which are shown in fig 8.

$$\varepsilon_i^p = \varepsilon_i - \frac{\sigma_i}{E} - \varepsilon_p^0 \quad (9)$$

$$\alpha_i = \sigma_i - \sigma^s \quad (10)$$

A series of $(\varepsilon_i^p, \alpha_i)$ values are used for data fitting and parameters C_k and γ_k in Eq. (8) can be obtained.

2.1.6. Stainless steel standards and guidelines

In this research project, the standards used as a reference are divided into two sections: the standards for stainless steel design and the standards for experimental tests (see table 1).

Table 1. Standards and normative.

Design of stainless steel structures	
SEI/ASCE 8-02 [17]	Specification for the Design of Cold-Formed Stainless Steel Structural Members
EN 1993-1-4 [6]	Eurocode 3 - Design of steel structures - Part 1-4: General rules - Supplementary rules for stainless steels
AS/NZS 4673 [18]	Cold-Formed Stainless Steel Structures
Experimental Test Methods	
ASTM E8 / E8M [19]	Standard Test Methods for Tension Testing of Metallic Materials
ASTM E606 / E606M [20]	Standard Test Method for Strain-Controlled Fatigue Testing
EN 10002-1 [21]	Metallic materials - Tensile testing - Part 1: Method of test at ambient temperature.

It is important to mention the **Design Manual for Structural Stainless Steel** [1] which was the first design guide for this alloy in Europe and was the basis for the Part 1-4 of the Eurocode 3 [6].

Also the EN10088-1 [5] “Stainless steels – Part 1: List of stainless steels” was useful for obtaining the chemical composition of different stainless steel grades.

2.2. Cyclic plasticity

In order to study cyclic plasticity, first, it is important to introduce plasticity in its broad sense.

Several materials, especially metal alloys, exhibit reversible and irreversible deformation behaviour such that when a load is applied, a fraction of strain is recovered and the rest remain deformed. The fraction of reversible deformation is known as elastic range and the fraction of irreversible deformation as plastic range (see fig. 9).

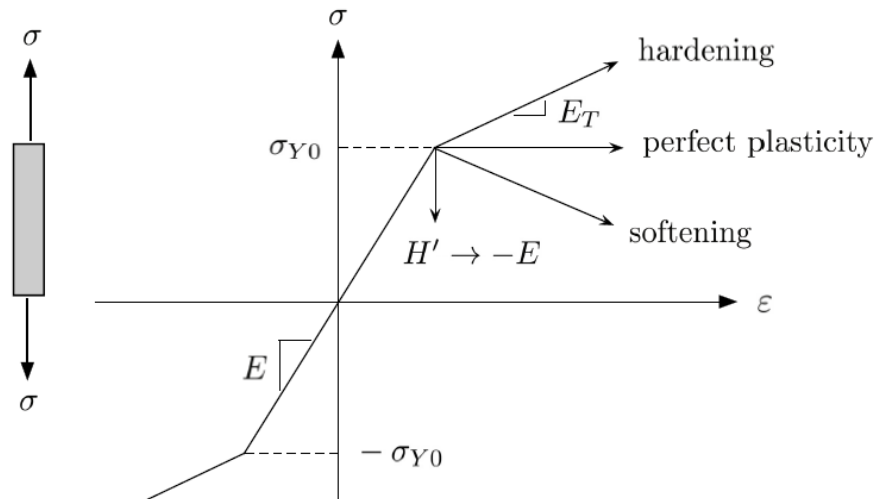


Fig. 9. Uniaxial loading of an elastoplastic bar: hardening when $H' > 0$, perfect plasticity when $H' = 0$, and softening when $H' < 0$. [22]

When a metal is elastically deformed, the load only alters the force balance of the atomic bonds, and the atoms assume new equilibrium positions, when the load is removed, the atoms return to their original position. On the other hand, in plastic deformation, the atoms slide over one another to produce a permanent shift of atom positions. As a result, a permanent change in the shape occurs. This plastic behaviour is due crystal dislocations in crystalline structures. [22]

Plasticity has an important role in structural engineering, specifically in places where a structure may be subjected to extreme loading condition, such as earthquakes. Plastic deformation of structural members helps dissipate energy from earthquakes and enhance the structural performance of the building.

2.2.1. Strain Hardening

When metals are deformed in plastic range, they become harder and stronger, this phenomenon is called strain hardening. If a stress produces plastic deformation, an even greater stress will be required to continue the deformation. [23]

To better represent this phenomenon, a stress-strain chart is given (see fig. 10). In the chart, it is shown how a ductile metal will behave when subjected to slow loading and unloading.

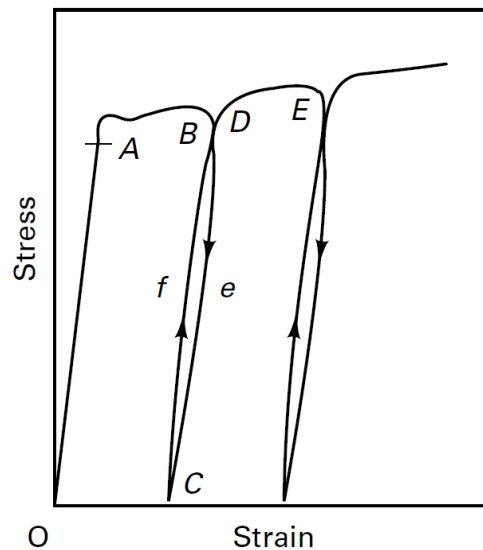


Fig. 10. Stress-strain diagram obtained by unloading and reloading a specimen. [23]

When loading, plastically deform and unloading a specimen, the curve follows a path through points O, A, B and C. Upon reloading from point C, an elastic behaviour is observed as the stress follows the line C-D with a slightly different path from that of unloading. Point D is now the yield point for the material. When comparing point A with point D it is noticeable that the plastic deformation made the material stronger. This can be repeated and a new yield point (point E) is obtained. [23]

When a material is strain-hardened and then subjected to reverse loading, the Bauschinger effect may occur.

2.2.2. Bauschinger Effect

For certain materials, the mechanical behaviour varies if the element was previously submitted to a history of deformations and this is reflected in the stress-strain curve. When certain elements are submitted to a reversal loading, the yield stress in compression decreases with initial yielding tension, and vice versa, this phenomenon is known as Bauschinger Effect. In fig. 11, this phenomenon is shown in a stress-strain curve.

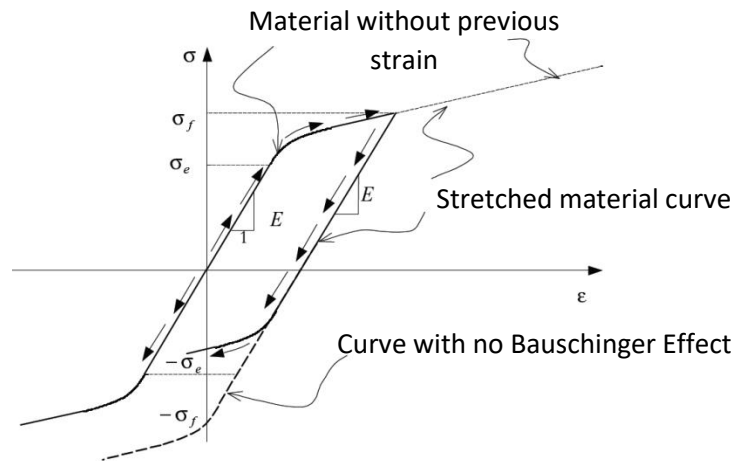


Fig. 11. Bauschinger Effect. [24]

The mechanism behind the Bauschinger effect is attributed to a particular kind of residual stresses that form on the grain boundaries of polycrystals, and is related to the dislocation structure in a cold worked metal [22].

2.2.3. Isotropic and kinematic hardening

In this section, an explanation of the analytical models that adequately take into account the phenomena explained in the previous sections is presented.

An isotropic hardening law implies that the yield stress in compression increases by the same amount as the yield stress in tension, this means that for every incremental change in the yield stress $\Delta\sigma_y$, the range of the elastic region changes by $2\Delta\sigma_y$. As a consequence isotropic hardening cannot capture the hysteretic response of a material subjected to cyclic loading [22].

In order to model the cyclic behaviour of the material, a kinematic hardening law is implemented. A kinematic hardening law indicates that for every incremental change $\Delta\sigma_y$, there is an incremental change $-\Delta\sigma_y$ in compression and vice versa. Therefore the elastic range does not change, it translates.

Kinematic and isotropic hardening generate the same initial incremental plastic strain, the difference is in the predicted yield stresses on reverse loading (See fig. 12). As it can be seen, kinematic hardening predicts a lower yield stress in compression i.e. takes into account the Bauschinger effect.

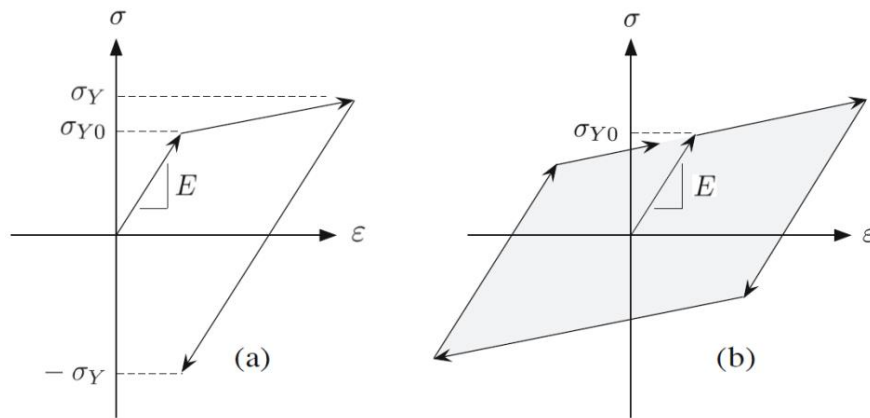


Fig. 12. Types of hardening: (a) isotropic, and (b) kinematic. [22]

A combined Isotropic/kinematic hardening can be used to describe a cyclic behaviour using an isotropic component and a kinematic component. With this type of hardening, it is possible to change and translate the elastic range of the material.

2.2.4. Low-cycle fatigue (LCF) and Cyclic Stress-Strain Curve

Unlike high-cycle fatigue which is related to an elastic phenomenon, low-cycle fatigue consists of repeatedly applied loads at high amplitudes, with plastic deformation in every cycle and with a number of cycles to failure from around 10^2 to 10^4 [25] [2]. This kind of fatigue may occur in structures that are subjected to small numbers of large displacement like earthquake-resistant buildings. When understanding the cyclic behaviour of a material subjected to low-cycle fatigue, it is not necessary to keep all the stress levels below a fatigue limit, as it would lead to an inefficient design.

Low-cycle fatigue under constant-amplitude loading leads to a high plastic deformation in the first cycle followed by much smaller strain amplitudes in following cycles. Therefore it is important to impose constant strain cycles when studying this phenomenon in the laboratory [25].

At constant strains, the stress amplitudes can increase or decrease. When increasing the material shows **cyclic strain hardening** and when decreasing it shows **cyclic strain softening** (see fig. 13). In both cases, the material stabilizes to a constant level after a number of cycles.

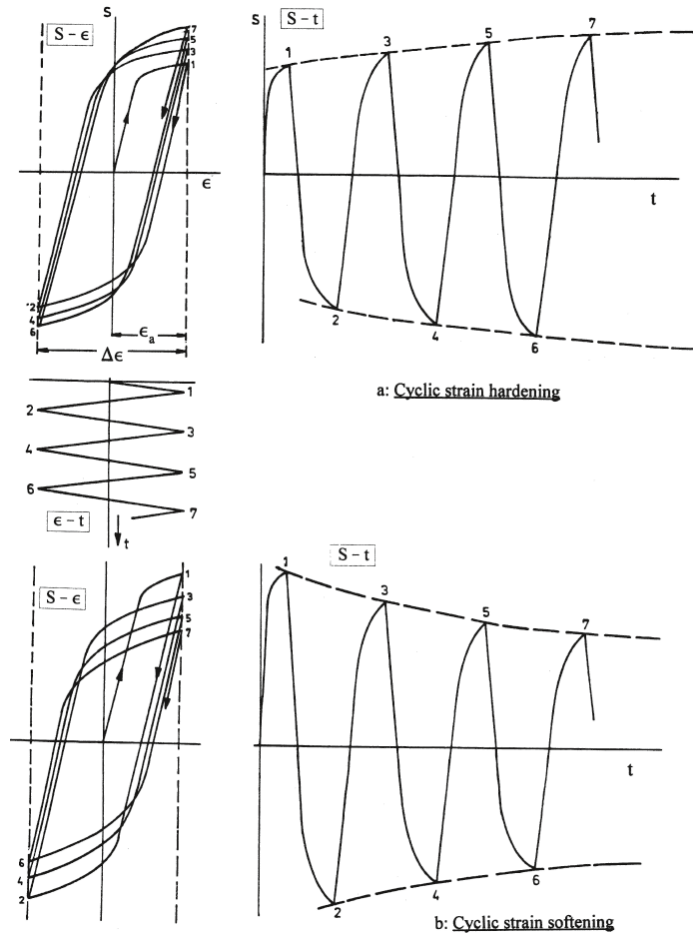


Fig. 13. Stress-strain loops during constant strain cycles of low-cycle fatigue and stress history charts. [25]

Coffin and Manson [26] [27] observed that plastic strain-life data from low-cycle fatigue test indicates a linear relationship if plotted on a log-log scale. This observation forms the basis of the Coffin-Manson relationship shown in Eq. 11.

$$\frac{\Delta\epsilon_p}{2} = \epsilon'_f (2N_f)^c \quad (11)$$

Where $\Delta\epsilon_p/2$ is the plastic strain amplitude, ϵ'_f the fatigue ductility factor coefficient, c the fatigue ductility exponent and $2N_f$ the number of reversals to failure.

To determine a cyclic stress-strain curve, there are different test methods proposed in the literature; namely the companion, multiple-step and incremental-step methods [28] [29]. The most suitable is **the companion method**, this method consists of testing several specimens, each one at a constant strain amplitude until failure (see fig. 14). Test data from this method allows the construction of the cyclic stress-strain curve of the material and it also allows obtaining its strain-life relationship. However, this method requires numerous quantity of coupons, long testing times and it may give ambiguous results as a consequence of constructing the curves with different specimens [27].

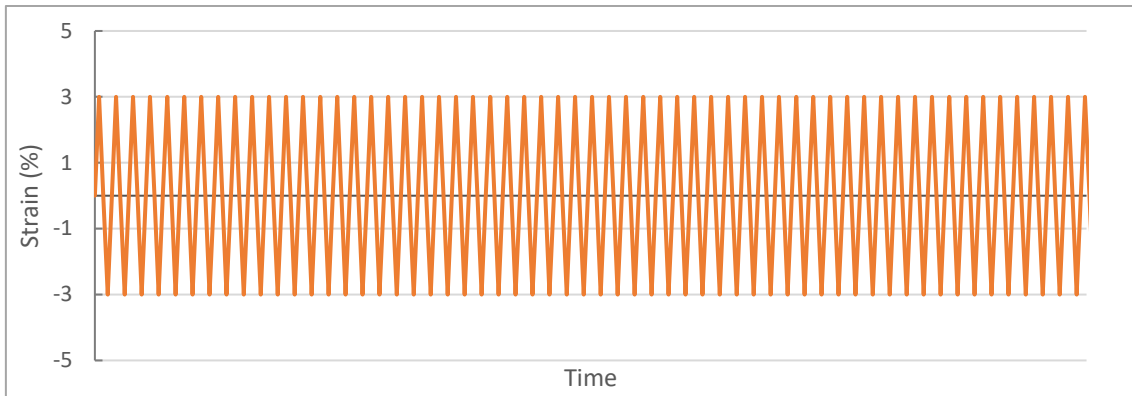


Fig. 14. Example of a strain history used in the companion test method.

The multiple-step method consists of testing a single specimen at a constant strain amplitude until it stabilises and then increasing the strain amplitude. This process is repeated until a sufficient number of hysteresis loops is recorded to construct the cyclic stress-strain curve (see fig. 15). This method appears to be better suited for earthquake engineering studies [28] and has the advantage of constructing the cyclic stress-strain curve with a single coupon. Its use becomes restricted at large strain amplitudes because specimens are likely to fail prematurely before stabilisation is achieved.

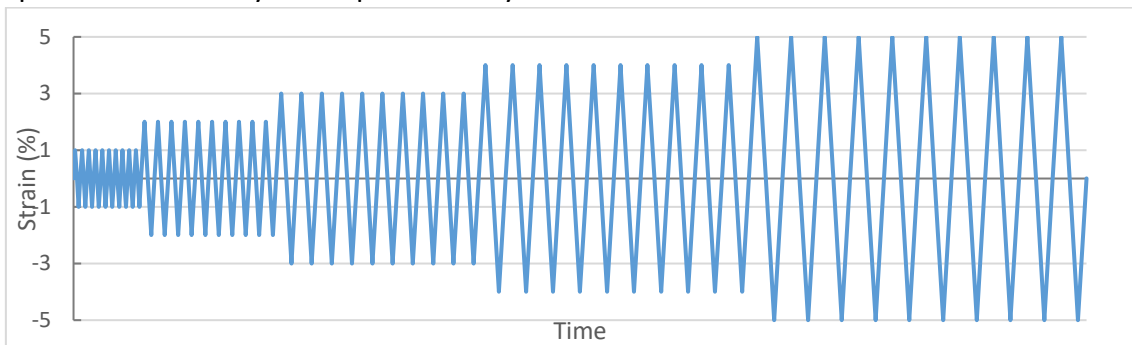


Fig. 15. Example of strain blocks used in the multiple-step test method.

In **the incremental-step method**, a single specimen is subjected to repeated blocks of cycles that increase at each cycle until a certain strain amplitude is recorded and then decrease to the starting point (see fig.16). As well as the multiple-step method, this method has the advantage of constructing the cyclic stress-strain curve with a single coupon, but its use also becomes restricted due to premature failure. Nevertheless, the incremental-step method is not recommended because it is observed that the results from this method may deviate from the true cyclic stress-strain curve [28].

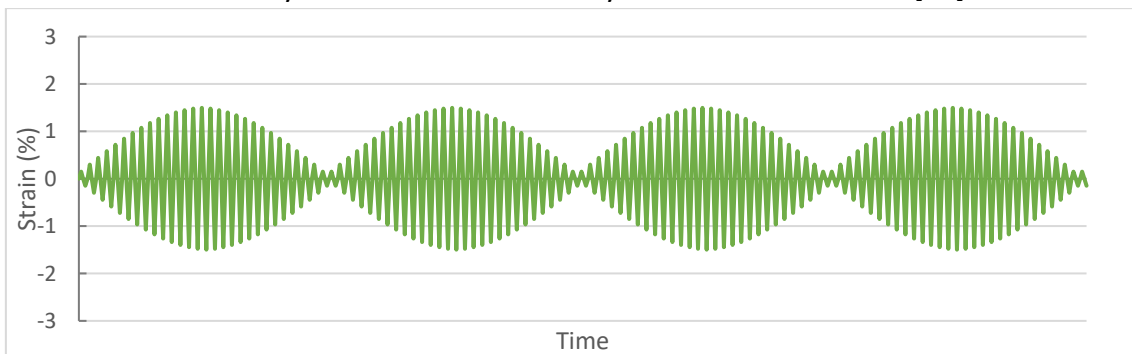


Fig. 16. Example of strain blocks used in the incremental-step method.

It is worth noticing that test with variable amplitude cannot be used to obtain the Coffin-Manson parameters.

2.2.5. Ratcheting

Ratcheting is a progressive incremental plastic deformation resulting from stress-controlled cyclic loading and it is divided in material ratcheting and structural ratcheting.

Material ratcheting is related to the characteristic of the material and its response at a microstructural level. In practice, the residual strain that persists after cyclic loading can be seen as a measure of the ratcheting strain [30]. For material ratcheting to occur, a mean stress deviating from zero is necessary. When a material is subjected to stress controlled cycles, it starts accumulating strain and it increases in a cycle-by-cycle manner [30]. Typical material ratcheting is shown in fig. 17.

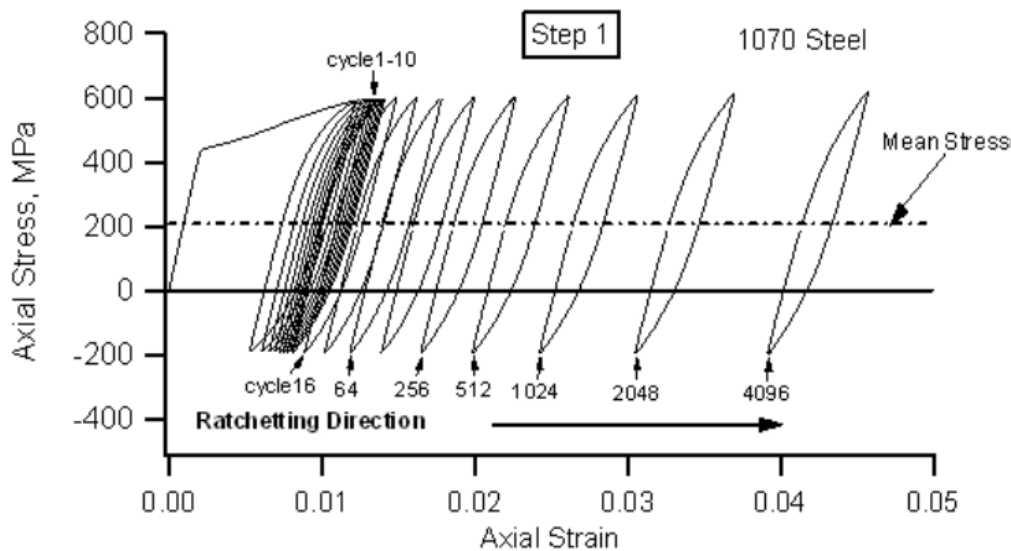


Fig. 17. Experimental cyclic ratcheting for a uniaxial loading. [31]

Material ratcheting is a phenomenon that must be taken into account when structures are subjected to plastic deformation in cyclic loading. Chaboche kinematic hardening model is an efficient model for ratcheting prediction [32].

Structural ratcheting is governed by the inhomogeneous stress state and it can occur without the influence of material ratcheting [30].

2.3. Previous studies about cyclic plasticity in stainless steel

There are numerous studies that have served as a reference for this research project. In this section, important aspects of these studies will be summarized and key elements will be compared between the different studies.

Previous studies performed experimental tests to obtain the mechanical properties of stainless steel, these test involved monotonic tensile tests and cyclic axial tests among others. In general, monotonic tensile tests were performed to obtain properties such as Young's modulus and yield strength; as well as strain hardening data. On the other hand

cyclic axial tests were strain controlled in order to obtain representative cyclic hardening data. Most of the studies have carried out cyclic axial tests of round and/or flat coupons using the companion method and/or multiple-step method.

The studies agree that, in order to establish analytical models and perform numerical simulations of the cyclic plasticity of stainless steel, cycle tests involving companion method are necessary. These tests were strain controlled and the coupons were subjected to cycles of strain amplitudes ranging from $\pm 0.3\%$ to $\pm 7\%$ (covering the low-cycle and extremely low-cycle fatigue) at strain rates ranging from 0.0005s^{-1} to 0.005s^{-1} .

The cyclic tests results were used to construct cyclic stress-strain curves, as well as to obtain cyclic hardening data which is necessary to establish the analytical model. The cyclic stress-strain curves were plotted along with the monotonic tensile stress-strain curves in order to compare them and show the strain hardening.

When using a FEM Software to simulate the cyclic plasticity, all the studies agree with a combined isotropic/kinematic model known as Chaboche model [15]. In order to use this model, data from hysteresis loops are extracted and used as input as explained in section 2.2.5. Subsequently, the parameters that define this model ($\sigma|_0, Q_\infty, b, C_k, \gamma_k$) are calibrated. The experimental and FE simulated hysteresis curves were plotted for comparison and validation.

Some of the conclusions from those papers that are relevant for this research project are presented as follows:

- Combined isotropic-kinematic hardening model is proved more accurate in simulating the cyclic stress-strain behaviour of various steel grades in comparison to Ramberg-Osgood model. [33]
- Cyclic stress response of the material was characterized by initial hardening followed by softening near failure. [34]
- The Ramberg-Osgood model gave excellent agreement with monotonic stress-strain curves. Under cyclic loading, stainless steel exhibited remarkable cyclic hardening and excellent hardening behaviour. The simulated curves agreed with the test and the cyclic hardening parameters obtained can be used in engineering practice. [35]
- Cyclic hardening rate increases with strain amplitudes. [36]
- The strength of duplex steel is increased by 10% by cyclic hardening. [37]
- Stainless steel, which displays substantial strain hardening in monotonic tensile tests, also demonstrated a much larger degree of cyclic hardening than two carbon steel materials. [2]
- The hysteresis loops of structural stainless steels are plump, stable and symmetric to the origin. [3]
- The austenitic stainless steel type 304 has larger cyclic hardening level compared to lean duplex stainless steel LDX2101. [3]

It is convenient to construct a comparative table in which key elements from different previous studies are shown.

In table 2, basic specifications of the test performed are shown. The test methods, the strain amplitudes, the strain rates and the kind of coupon that were used in the cyclic tests are compared. The strain rates vary markedly, the highest rate is 10 times higher than the lower rate, nevertheless, these strain rates are low and prevent heat from altering the results.

Table 2. Comparative table of previous studies (part1).

Previous Study	Methods	Amplitude	Strain rate	Coupon
K.H. Nip et al. [2]	Companion	$\pm 1\%$, $\pm 3\%$, $\pm 5\%$, $\pm 7\%$	$0.005s^{-1}$	Flat
F. Zhou, L. Li [3]	Multiple-step, Cyclic alternate and Cyclic tensile	From $\pm 0.5\%$ to $\pm 2\%$	$0.0005s^{-1}$	Flat and round
A. Dutta et al. [36]	Companion	From $\pm 0.3\%$ to $\pm 1.2\%$	$0.001s^{-1}$	-
S. Chandra Roy et al. [34]	Companion	From $\pm 0.3\%$ to $\pm 1\%$	$0.003s^{-1}$	Round
Y.Q. Wang et al. [35]	Companion, multiple-step, among others	From $\pm 0.4\%$ to $\pm 1\%$	0.05Hz	Flat

In table 3, results from tests regarding the parameters that define the characteristics of the material are presented. The parameters obtained from the monotonic test like Young's modulus and yield strength are fairly similar, on the other hand, the combined Kinematic/isotropic hardening parameters vary even in the same study.

Table 3. Comparative table of previous studies (part2).

Previous Study	Steel Grade EN	E (N/mm ²)	Yield strength ($\sigma_{0.2}$) (N/mm ²)	Combined hardening parameters					
				Amp	$\sigma _0^*$	Q_∞^*	b	C_k^*	γ_k
K.H. Nip et al. [2]	1.4301 and 1.4307	201 300	419	$\pm 1\%$	224.5	431.5	0.1625	175450	420.5
		197 730	483	$\pm 3\%$	236.8	516.8	1.165	82675	185.5
		197 960	552	$\pm 5\%$	246	418.4	2.164	88520	179.6
		191 690	538	$\pm 7\%$	224.5	593.5	1.7625	125600	215.5
F. Zhou, L. Li [3]	1.4301	204300	310.7	No data available					
	1.4162	204700	470						
A. Dutta et al. [36]	1.4401	200000	-	$\pm 0.6\%$	225	60	9.71	42096	594.5
S. Chandra Roy et al. [34]	1.4404	-	-	$\pm 0.5\%$	211	42.3	21.6	57805	619.04
Y.Q. Wang et al. [35]	1.4401	209500	356.5	$\pm 0.4\%$	234	77	10.5	56760	420

*Values in (N/mm²).

Bold indicates mean values from different coupons.

As mentioned before, some results are plotted as a cyclic stress-strain curve that can be obtained from half of a stable block, each data pair is obtained from a cyclic test at different amplitudes. A typical plot of the cyclic stress-strain curve along with the monotonic tensile stress-strain curve is shown in fig. 18.

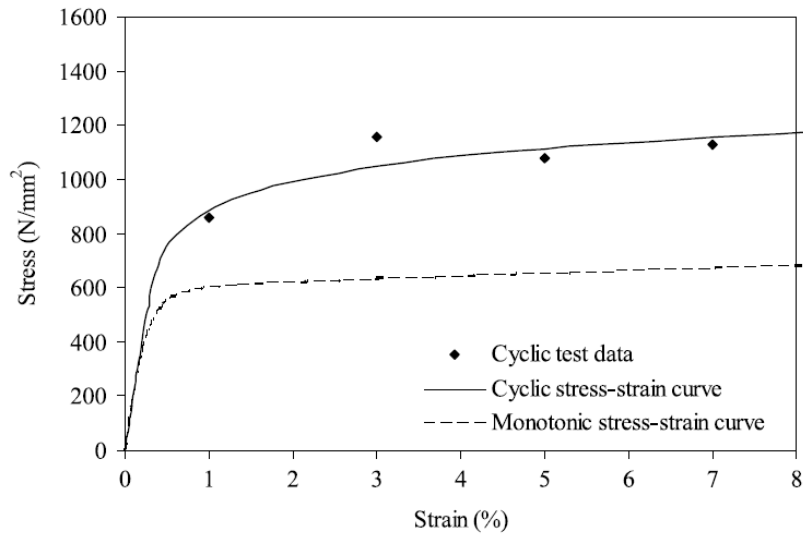


Fig. 18. Example of comparison of cyclic and monotonic stress-strain curves for cold-formed stainless steel 50 x 50 x 3 specimens. [2]

Another interesting result is the plot of hysteresis loops obtained from a test in contrast with the FE model simulated with the parameters obtained from the same test. A typical plot is exhibited in fig. 19.

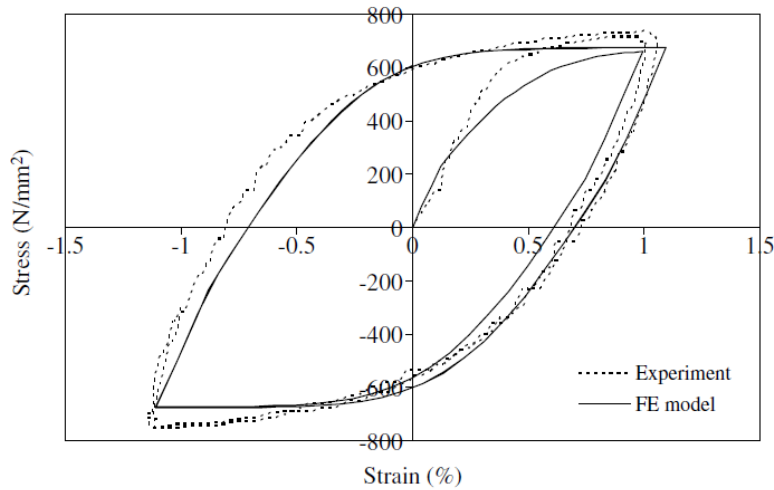


Fig. 19. Example of experimental and FE simulated stress-strain hysteresis curves of a cold-formed stainless steel specimen in the first 2 cycles of 1% strain amplitude tests. [2]

3. NUMERICAL MODELLING

In engineering, a common numerical method is the finite element method (FEM) which is able to perform a structural analysis by subdividing large structures into smaller and simpler elements.

3.1. A brief introduction to the finite element method (FEM)

Since the beginning of the development of the FEM in the 1940s, throughout the years it has become a reliable method for the resolution of different kinds of engineering problems including structural analysis. Its use has risen in the last decades due to the great development of computer hardware and software. [38]

The finite element method is a method for solving problems involving engineering and mathematical physics concerning many fields of application like structural analysis, fluids flow, acoustics, aerodynamics, geophysics, oceanography, meteorology, electromagnetics, plasma physics, among others [39]. To solve these problems, the method uses a program to subdivide a continuous system into simpler discrete elements (finite elements), each element has equations that rule its behaviour, and therefore this produces a large number of algebraic equations that the method resolve using a numerical approximation.

The set of the subdivided elements is called mesh. The mesh consists of all the finite elements and nodes that shape the problem, the nodes connect the elements to each other. The elements can be one-dimensional, two-dimensional or three-dimensional, with different shapes (like hexahedron or wedge Elements) and different order (first-order or second-order) depending on the complexity of the engineering problem, the information to extract and the computational capacity. Once the mesh is generated, numerical methods are implemented and the equation system is solved.

After this step comes a phase called post-processing. In the post-processing phase, a large number of results are organized such that they are easily understandable and be compared to the physical phenomenon. It is important to recall that the FEM shows an approximate solution and therefore the model has to be precise and carefully meshed with the possibility of being compared with a known problem as a sort of calibration.

3.2. Software

The computer software ABAQUS-Simulia was used to carry out the numerical simulations. ABAQUS is a commercial software that uses FEM to resolve all kinds of engineering and mathematical physics problems. The software has two parts:

- Abaqus standard is the one that solves problems applying the finite element method (FEM). To execute any kind of analysis, the program requires an input file (.INP) that contain the commands in Phyton programming language.

- Abaqus-CAE is a user-friendly user interface (UI) from which the input file can be generated easily, also the UI is very convenient to show the results more interpretable in the post-processing.

The feature of using Python programming language is advantageous since it adds versatility in a way that it is possible to create protocols of parametric studies with several vectors of variables and, with the help of macros, the results of the parametric studies are extracted automatically.

It is important to highlight that Abaqus does not work with a specific unit system, this means that the input must have consistency in all the units. In this research project, the international unit system was used when employing Abaqus software, the detailed unit are shown in table 4.

Table 4. Unit system used in Abaqus software.

	Unit
Distance	Millimetre (mm)
Force	Newton (N)
Mass	Ton (ton)
Tension	(N/mm ²)
Density	(ton/mm ³)
Time	Seconds (s)

3.3. Modelling Specifications

In this section, general aspects of the numerical model are described in order to show how the problem is represented in the software and how the analysis is executed.

Analyses

In this research project there are 3 different analyses:

- Buckling: in this analysis, the model is subjected to axial load or displacement and the eigenvalues are determined. This analysis is used for the Coupon design (section 4.1).
- Monotonic tensile: in this analysis, the model is subjected to a monotonic tensile displacement simulating the tensile test. This analysis is used in the convergence analysis (section 3.3).
- Cyclic axial: in this analysis, the model is subjected to a periodic axial load or displacement that follows certain amplitude. This analysis is used in the comparison between FEM and experimental tests (chapter 6).

These analyses are defined in the model **steps**, this is explained later in this section.

Model

The three-dimensional geometry of the element of study is delineated with Abaqus-CAE sketcher tool. The adequate tool to draw cylindrical objects is with the Sweep-type sketch. The features of the model are set as a deformable solid.

The geometry of the element consists of a cylindrical solid with a reduced cross-section length in the middle (see fig. 20). For more details of the geometry and the coupon design, see section 4.1.

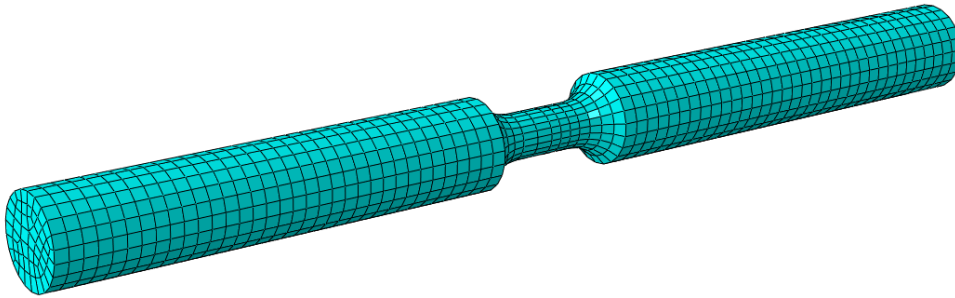


Fig. 20. Simulated coupon.

After creating the geometry of the model, the material is defined. In order to do so, one general property and two mechanical proprieties are necessary:

- Density: consist of the mass-volume ratio in ton/mm^3 .
- Elastic behaviour: the Young's Modulus and Poisson's ratio are defined.
- Plastic behaviour: the hardening and cyclic hardening behaviour are defined.

As for the plastic behaviour, it is important to highlight that one of the objectives of this research project is to determine parameters that would simulate the actual cyclic plasticity of the stainless steel, therefore several hardening parameters will be taken into account. The details about the material model used are explained in chapter 6.

The section of the model is defined as a solid and homogeneous section with the properties of the previously defined material.

Step

In Abaqus software, the problem is divided into steps. The steps are phases of the history. They contain the type of analysis and additional data, such as external actions and boundary conditions. When a step is running, the algorithm updates the size of the increments automatically until the step is completed, this increments can also be controlled when setting up the step.

In this project the following steps were used:

- Initial step: The initial conditions of the problem, such as boundary conditions, are defined.

- Analysis step: Following the initial step is usually an analysis step. A “static, general” step (classified as “general”) is the analysis applied to most of the cases of study of this project, including cyclic loading. A “buckle” step (classified as “linear perturbation”) is the analysis applied to the buckling analysis in order to design the coupons.

External Actions

The external actions consist of loads or displacements depending on the case: for the cyclic loading and monotonic loading analysis, the external actions are set as displacements. The displacement follows a tabular amplitude that describes the cyclic or monotonic behaviour (see fig. 21). As for the buckling analysis, both load and displacement were applied in different analyses in order to obtain the eigenvalues that determine the load or the displacement that would cause the buckling failure of the

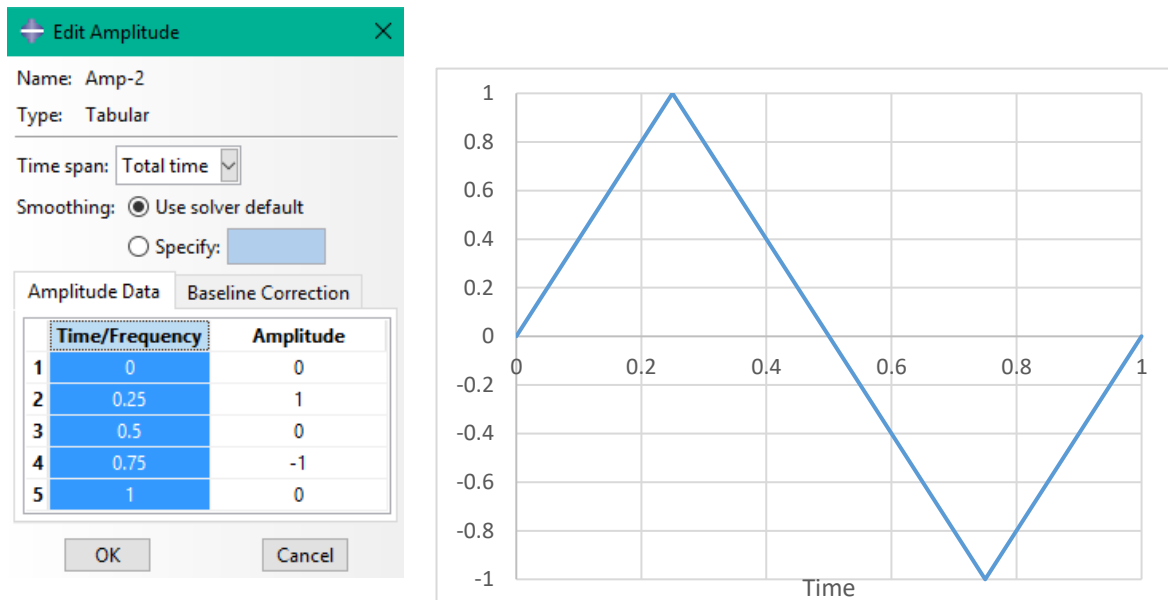


Fig. 21. Example of a tabular amplitude.

Mesh and finite element type

Once the geometry, the material and the section of the element of study are defined, the mesh can be generated along with the finite elements (see fig. 20). The finite elements are joined by nodes and together they form the whole element and describe its behaviour, the smaller the finite elements the more precise are the results, but at the cost of reduced computing performance and increased running time. There are different types of finite elements and, as well as the element size, it affects the precision and computing performance. It is important to balance both element type and element size in order to obtain results with a fairly small error and in a relatively short time.

When talking about 3D finite elements there are several element types that Abaqus supports: Hexahedron, tetrahedron and wedge elements. Each element has a linear or quadratic geometric order, which establishes the number of nodes in each element.

Choosing a specific finite element type depends on many factors, including the shape of the element and the analysis type. Although the geometry of the element and the analyses types in this research project are quite simple, a convergence study was made in order to compare the different element types and choose the adequate one.

Convergence study

Seven monotonic tensile analyses with different mesh configurations were studied. A non-linear stainless steel material is set in the analyses.

It is worth noticing that, although the convergence study is made with monotonic tensile analyses, the resulting element type will be used in the cyclic analyses.

In the following figure, a comparison between three element types is shown in a Stress-Strain and a Reaction force-Displacement graphs (figure 22A and figure 22B respectively). It is important to point out that in these three analyses, the elements are meshed with the default mesh algorithm and with an approximate global size of 3 millimetres, generating a total number of elements of 4526, 14793 and 5767 for Hexahedron, Tetrahedron and Wedge element type respectively.

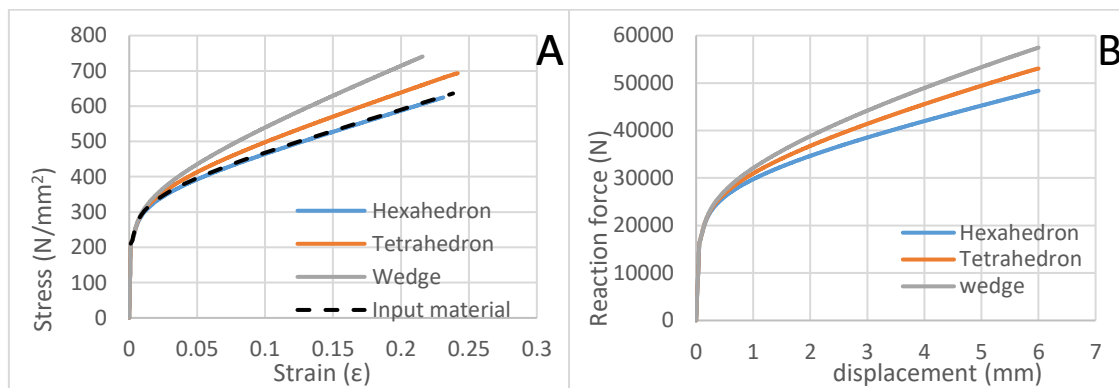


Fig. 22. Comparison between finite element types (global size of 3mm) in Stress-Strain chart (A) and Reaction force-Displacement chart (B) of monotonic analyses.

Although the running times of the three element types are similar (around 10 minutes), it is noticeable that the results differ from each other. When comparing the monotonic analysis with the material curve used in the analysis (input material), the finite element type that follows the correct behaviour is the hexahedron element.

To ensure that the hexahedron is the best option, the analyses were repeated with an approximate global size of 1.5 millimetres generating a total number of elements of 28120, 104984 and 47952 for Hexahedron, Tetrahedron and Wedge element type respectively. As a result, the behaviour of hexahedron of 1.5mm is practically identical to that of the hexahedron of 3mm and the behaviour of the tetrahedron and the wedge elements differs from the hexahedron the same way as their counterparts, but with a smaller error (see figure 23). Therefore it is concluded that the hexahedron finite element is suitable to further analyses.

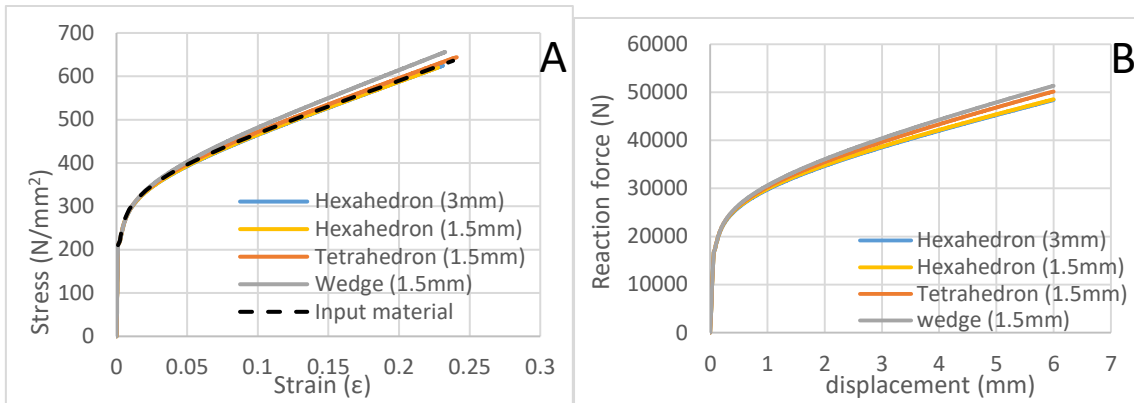


Fig. 23. Comparison between finite element types (global size of 1.5mm) in Stress-Strain chart (A) and Reaction force-Displacement chart (B) of monotonic analyses.

As previously mentioned, each finite element type has a linear or quadratic geometric order, so it is important to compare the difference between a linear hexahedron element and a quadratic hexahedron element including reduced integration and full integration of each one. The comparison of all these cases is shown in figure 24.

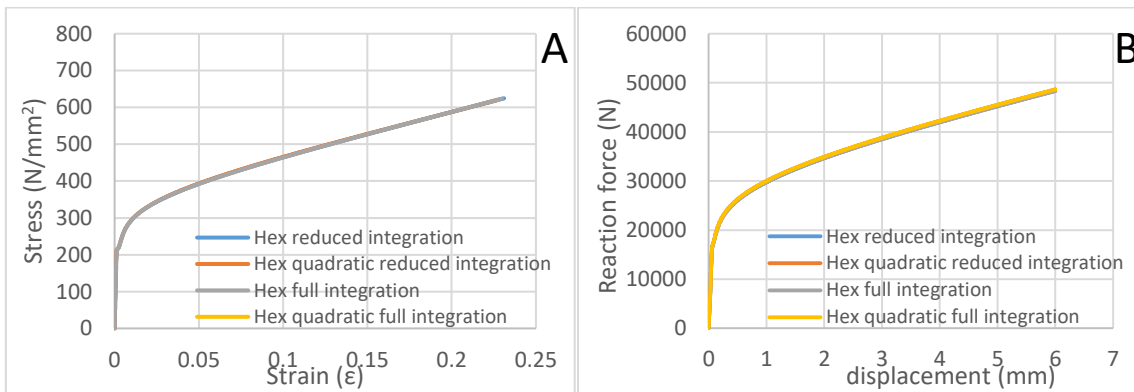
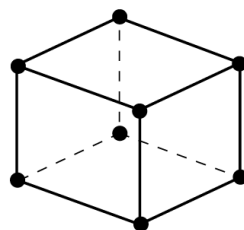


Fig. 24. Comparison between hexahedron geometry order in Stress-Strain chart (A) and Reaction force-Displacement chart (B) of monotonic analyses.

As it is shown, in this particular case and with this size of finite element, changing either the geometric order or the integration method, doesn't have a significant impact on the mechanical behaviour. Therefore, the finite element type that better suits the analysis is the one with better computational performance (the one that lasts less), in this case, the hexahedron with a linear geometric order and with reduced integration method. This element is classified in Abaqus as C3D8R and it is an 8-node linear brick with reduced integration (see fig. 25).



Linear element
(8-node brick, C3D8)

Fig. 25. Finite element C3D8R.

3.4. Obtaining the results

After running all the analyses comes the post-processing phase where all the useful data is extracted. In this phase, it is possible to obtain variables that describe the behaviour of the element and compare them in a chart, as well as show them in a graphical display. The variables of interest in this research project are the ones associated with mechanical behaviours, such as strain, plastic strain, stress, load, reaction force and displacement. There is a value for each variable in each increment of the step, this means that, when obtaining variables in a chart, there are many (X, Y) data pairs as there are increments.

The results has to be extracted from an finite element or a node, in this project the nodes of interest are the ones where the load or displacement is applied and the ones where the boundary conditions are established, as for the finite elements the ones used for obtaining variables are the ones located in the cross-section of the centre of the element of study.

4. EXPERIMENTAL TEST

In this chapter, an exhaustive description of the experimental process is presented; starting with the geometry of the coupons and the instrumentation implemented in the test, and followed by the test set up section which describes the preparation of the coupons and the tests machine, as well as the loading protocols applied.

4.1. Coupon Design

The geometry of the test coupons consists of a cylindrical bar made with hot-rolled austenitic stainless steel, which includes a central region of reduced cross-sectional area (made with a lathe) to constrain the place at which the fracture occurs (see fig. 26).

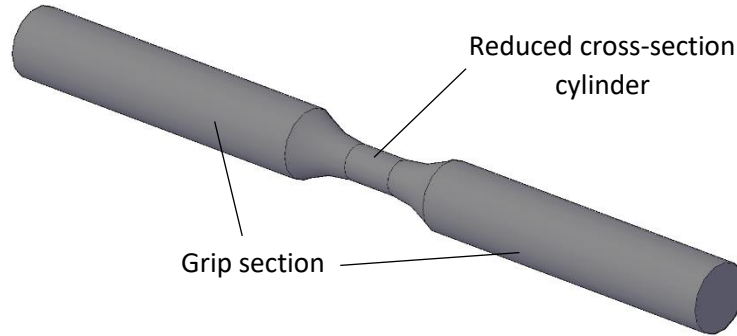


Fig. 26. Coupon scheme.

For the first approach to the geometry of the test coupons, it is necessary to start with the length of the reduced cross-section; in order to do so, preliminary calculations were done. When subjected to compressive strength, the coupon is susceptible to an undesired buckling failure and therefore it is important to prevent it. In the preliminary calculations, the Euler's critical load is taken into account to determine the strain and displacement that would cause the buckling failure of this region at a variety of lengths. With this range; it is possible to select a potential range of lengths that prevent buckling.

Taking as reference different coupons in previous studies and the previously mentioned standards, the dimensions of the reduced cross-section cylinders used in the buckling analysis were 9mm and 10 mm diameter and lengths from 10mm to 50mm, with Young's modulus of 193 and 210GPa.

Considering the unfavourable situation in which the boundary conditions of the central region are pinned supports and, hence, a critical length equal to the member length, the following results are obtained (see table 5, 6, 7 and 8). Equations 12 and 13 are used to determine the critical load and the displacement that would cause buckling.

It is important to notice that these calculations are made assuming an elastic behaviour of the material and not taking into account the non-linearity. This allows to simplify the calculations and the obtained result are conservative.

$$\sigma = \frac{F}{A} ; \sigma = E \cdot \varepsilon ; \varepsilon = \frac{\delta}{L} ; \boxed{F_{cr} = \frac{\pi^2 \cdot E \cdot I}{L_{cr}^2} \quad (12)} ; I_O = \frac{\pi}{4} \cdot r^4 ; A_O = \pi \cdot r^2$$

$$\frac{\pi^2 \cdot E \cdot \frac{\pi}{4} \cdot r^4}{L_{cr}^2} = E \cdot \pi \cdot r^2 \cdot \frac{\delta}{L} \rightarrow \boxed{\delta = \frac{\pi^2 \cdot r^2 \cdot L}{4L_{cr}^2} \quad (13)}$$

Table 5. Critical load, strains and displacement of reduce area region. 10mm diameter. E=193GPa.

r (mm)	L (mm)	δ (mm)	ϵ	$\epsilon\%$	Fcr (kN)
5	10	6.17	0.62	61.69	9350.33
5	15	4.11	0.27	27.42	4155.70
5	20	3.08	0.15	15.42	2337.58
5	25	2.47	0.10	9.87	1496.05
5	30	2.06	0.07	6.85	1038.93
5	35	1.76	0.05	5.04	763.29
5	40	1.54	0.04	3.86	584.40
5	45	1.37	0.03	3.05	461.75
5	50	1.23	0.03	2.47	374.01

Table 6. Critical load, strains and displacement of reduce area region. 9mm diameter. E=193GPa.

r (mm)	L (mm)	δ (mm)	ϵ	$\epsilon\%$	Fcr (kN)
4.5	10	5.00	0.50	49.97	6134.75
4.5	15	3.33	0.22	22.21	2726.55
4.5	20	2.50	0.13	12.49	1533.68
4.5	25	2.00	0.08	7.99	981.56
4.5	30	1.67	0.06	5.55	681.63
4.5	35	1.43	0.04	4.08	500.79
4.5	40	1.25	0.03	3.12	383.42
4.5	45	1.11	0.03	2.47	302.95
4.5	50	1.00	0.02	2.00	245.39

Table 7. Critical load, strains and displacement of reduce area region. 10mm diameter. E=210GPa.

r (mm)	L (mm)	δ (mm)	ϵ	$\epsilon\%$	Fcr (kN)
5	10	6.17	0.62	61.69	10173.93
5	15	4.11	0.27	27.42	4521.74
5	20	3.08	0.15	15.42	2543.48
5	25	2.47	0.10	9.87	1627.83
5	30	2.06	0.07	6.85	1130.43
5	35	1.76	0.05	5.04	830.52
5	40	1.54	0.04	3.86	635.87
5	45	1.37	0.03	3.05	502.41
5	50	1.23	0.03	2.47	406.95

Table 8. Critical load, strains and displacement of reduce area region. 9mm diameter. E=210GPa.

r (mm)	L (mm)	δ (mm)	ϵ	$\epsilon\%$	Fcr (kN)
4.5	10	5.00	0.50	49.97	6675.11
4.5	15	3.33	0.22	22.21	2966.71
4.5	20	2.50	0.13	12.49	1668.78
4.5	25	2.00	0.08	8.00	1068.01
4.5	30	1.67	0.06	5.55	741.68
4.5	35	1.43	0.04	4.08	544.90
4.5	40	1.249	0.03	3.12	417.19
4.5	45	1.11	0.03	2.47	329.63
4.5	50	1.00	0.02	2.00	267.00

An analysis of the results obtained in the previous tables allows to know the maximum length of the reduced cross-section that prevents buckling at certain strain.

On the other hand, the space necessary to attach the instrumentation is determinant to establish the mentioned length. Therefore, a minimum length is necessary to adequately attach a strain gauge.

Considering the above and taking as a reference that the test could reach around 10% of strain amplitude, it is established a potential range of reduced lengths between 15 and 22.5 mm and a diameter of 10mm. As a result, buckling is fairly prevented, the strain amplitude is sufficient for the test and the coupon provides enough space for the strain gauge.

With a first approach of the dimensions established, numerical models were used to perform a buckling analysis and estimate the critical load of the whole coupon, using the nonlinear finite element software Abaqus. In these models, the boundary conditions are fixed supports and are located in the grip section, imitating the jaws of the test machine. Foreseeing that the jaws could be placed at different distances in the grip section and therefore have an impact in the buckling behaviour, the models were executed with a variety of lengths between jaws (L_{jaws}) or coupon span (see fig. 27). The objective of these models is to get loads, displacements and strains that would cause the buckling failure of the whole test coupon in order to set final dimensions for coupons that safely satisfy the requirements of the cyclic test i.e. reach certain strain amplitude without buckling.

It is worth noticing that the jaws of the test machine, which are used to grip the coupon by friction, set the diameter of the grip section at 20mm. And the radius of the transition (radius of fillet) is set at 30mm, this dimension is obtained from previous studies and it satisfies the ASTM E606 / E606M [20] standard.

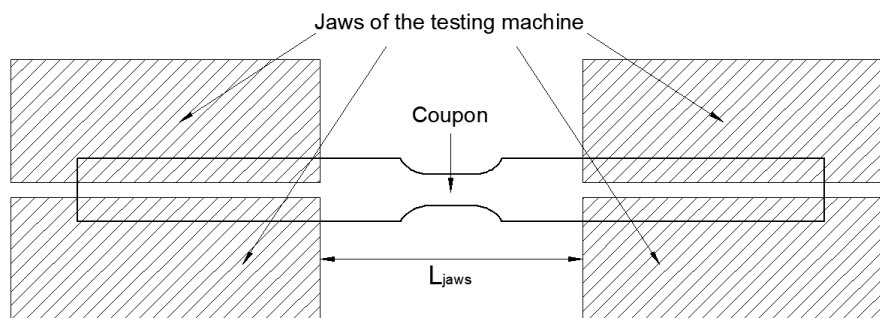


Fig. 27. Scheme of the coupon held by the test machine.

As well as the previous calculations, the models consider an elastic behaviour and were made with Young's modulus of 193 and 210GPa. The following results are shown.

Tables 9, 10, 11 and 12; present the results of the buckle analyses performed in Abaqus. The tables show displacements (δ), strains (ϵ) and loads (F_{cr}) that would cause buckling of the coupon. Figures 28, 29 and 30 show these results in charts for a better representation with the addition of the previous results (critical loads for reduced cross-section cylinders) as a top limit.

Table 9. Critical loads, strains and displacements. 15mm length of reduced cross-section. E=193GPa.

L_{jaws}	δ (mm)	ϵ	Fcr (kN)
69.42	6.32	0.15	2222.30
90.67	6.08	0.13	1899.00
111.92	5.39	0.10	1514.80
133.17	4.56	0.08	1165.00
154.42	3.84	0.06	899.02
175.67	3.28	0.05	709.54
196.92	2.84	0.04	570.94
218.17	2.51	0.03	471.16

Table 10. Critical loads, strains and displacements. 22.5mm length of reduced cross-section. E=193GPa.

L_{jaws}	δ (mm)	ϵ	Fcr (kN)
76.92	5.55	0.11	1659.30
98.17	5.48	0.10	1480.40
119.42	5.09	0.08	1253.70
140.67	4.47	0.07	1013.50
161.92	3.84	0.05	805.49
183.17	3.31	0.04	645.83
204.42	2.87	0.04	524.12
225.67	2.54	0.03	434.57

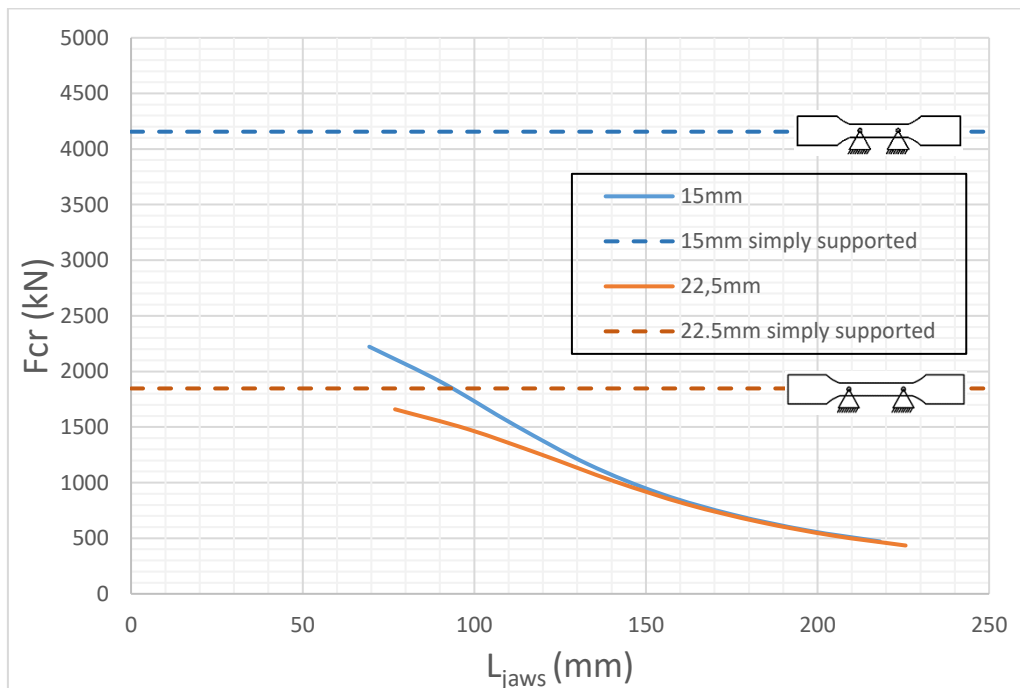


Fig. 28. Variation of critical loads at different lengths between jaws. E=193GPa.

Table 11. Critical loads, strains and displacements. 15mm length of reduced cross-section. E=210GPa.

L_{jaws}	δ (mm)	ϵ	Fcr (kN)
69.42	6.32	0.15	2418.00
90.67	6.08	0.13	2066.20
111.92	5.39	0.10	1648.20
133.17	4.56	0.08	1267.60
154.42	3.84	0.06	978.21
175.67	3.28	0.05	772.04
196.92	2.84	0.04	621.24
218.17	2.51	0.03	512.66

Table 12. Critical loads, strains and displacements. 22.5mm length of reduced cross-section. E=210GPa.

L_{jaws}	δ (mm)	ϵ	Fcr (kN)
76.92	5.55	0.11	1805.40
98.17	5.48	0.10	1610.80
119.42	5.09	0.08	1364.20
140.67	4.47	0.07	1102.80
161.92	3.84	0.05	876.44
183.17	3.31	0.04	702.72
204.42	2.87	0.04	570.29
225.67	2.54	0.03	472.84

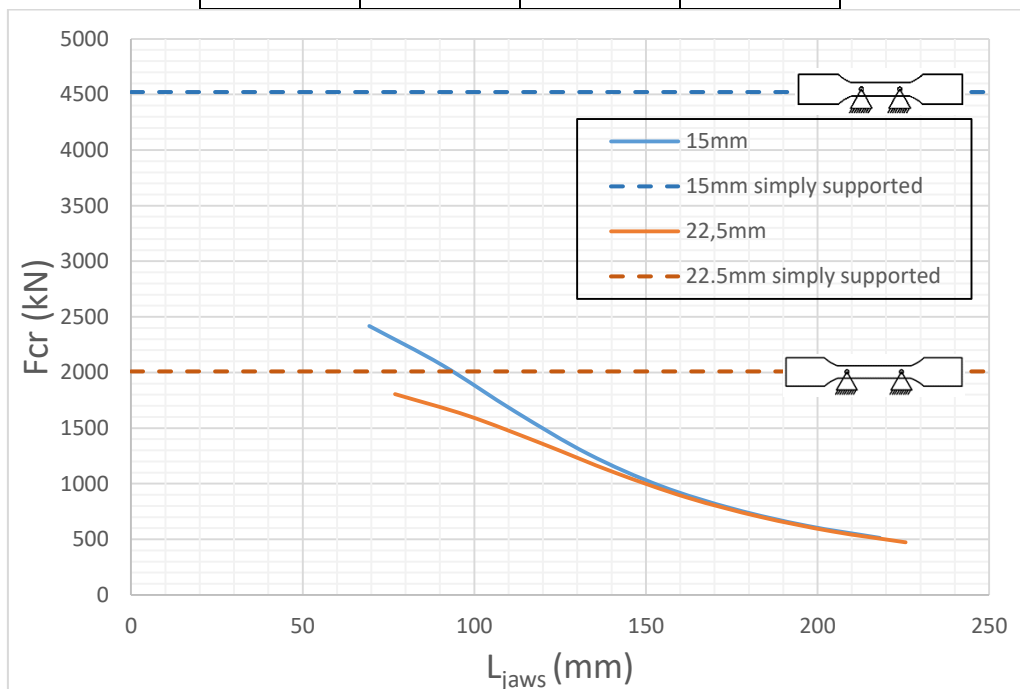


Fig. 29. Variation of critical loads at different lengths between jaws. E=210GPa.

A good way to display the results is with a chart containing the values of strain versus the test coupon span (L_{jaws}) because the strain that causes buckling is not a function of Young's modulus and therefore the chart works for any test coupon of this dimensions regardless of this modulus (see fig. 30).

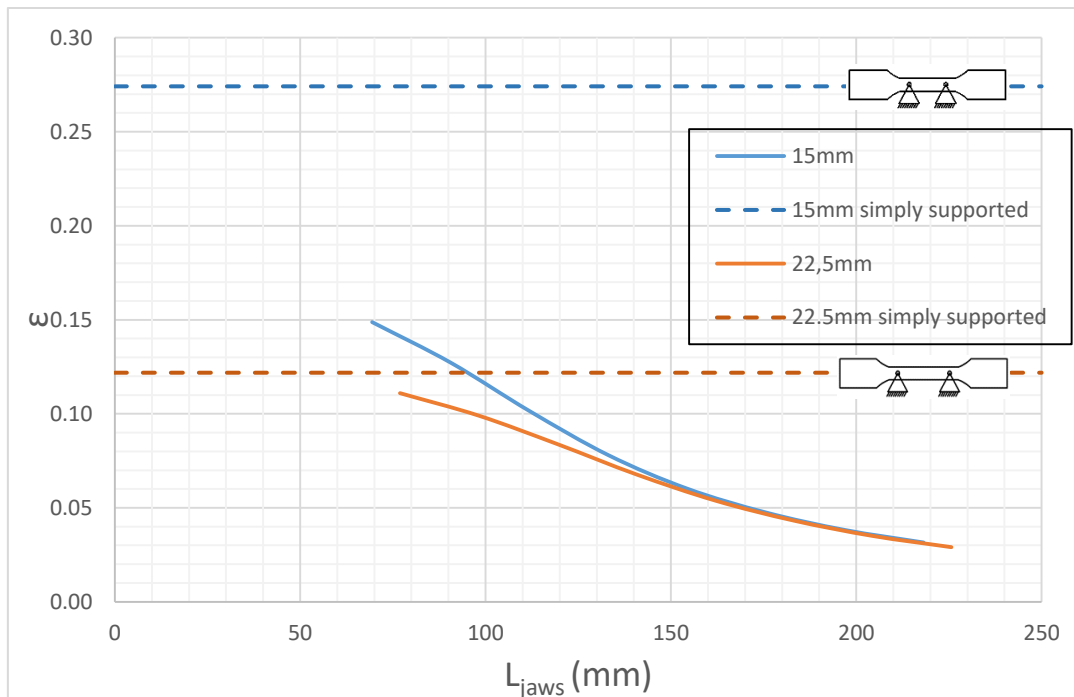


Fig. 30. Variation of strain that would cause buckling at different lengths between jaws.

As it is shown in the results, the test coupon of 15mm of reduced section clearly satisfy the stipulated criteria, giving a wide range of lengths in which the coupon can be subjected to a compression strain of around 10% without buckling. Considering that the length between the grip sections i.e. the minimum length between the jaws of the apparatus, is 48.2mm, the range on which the coupon could reach a strain of 10% without buckling goes from 48.2mm to around 110mm. Whilst the 22.5mm coupon presents a range from 55.7mm to 95mm making it less attractive for the test.

After all the previous results, the most appropriate length of reduced cross-section is 15mm.

When requesting the coupons from the manufacturer, they requested changing the radius of fillet from 30mm to 10mm. This was due to similarities with a kind of coupon that they commonly fabricate for tensile testing following the standard for tensile tests ASTM E8/E8M – 09 [19]. The request was discussed and accepted. Therefore, further analyses with the new geometry (see fig. 33) were made and the following results are obtained (see tables 13 and 14).

Table 13. Critical loads, strains and displacements. 15mm length of reduced cross section and 10mm radius of fillet. $E=193\text{GPa}$.

L_{jaws}	δ (mm)	ϵ	Fcr (kN)
58.05	7.40	0.22	3215.80
83.78	6.80	0.17	2487.30
109.51	5.38	0.11	1701.70
135.24	4.20	0.08	1169.00
160.97	3.40	0.06	845.60
186.70	2.85	0.04	640.73
212.44	2.46	0.03	504.01
238.17	2.17	0.03	408.35

Table 14. Critical loads, strains and displacements. 15mm length of reduced cross section and 10mm radius of fillet. $E=210\text{GPa}$.

L_{jaws}	δ (mm)	ϵ	Fcr (kN)
58.05	7.40	0.22	3499.00
83.78	6.80	0.17	2706.40
109.51	5.38	0.11	1851.60
135.24	4.20	0.08	1271.90
160.97	3.40	0.06	920.09
186.70	2.85	0.04	697.17
212.44	2.46	0.03	548.40
238.17	2.17	0.03	444.32

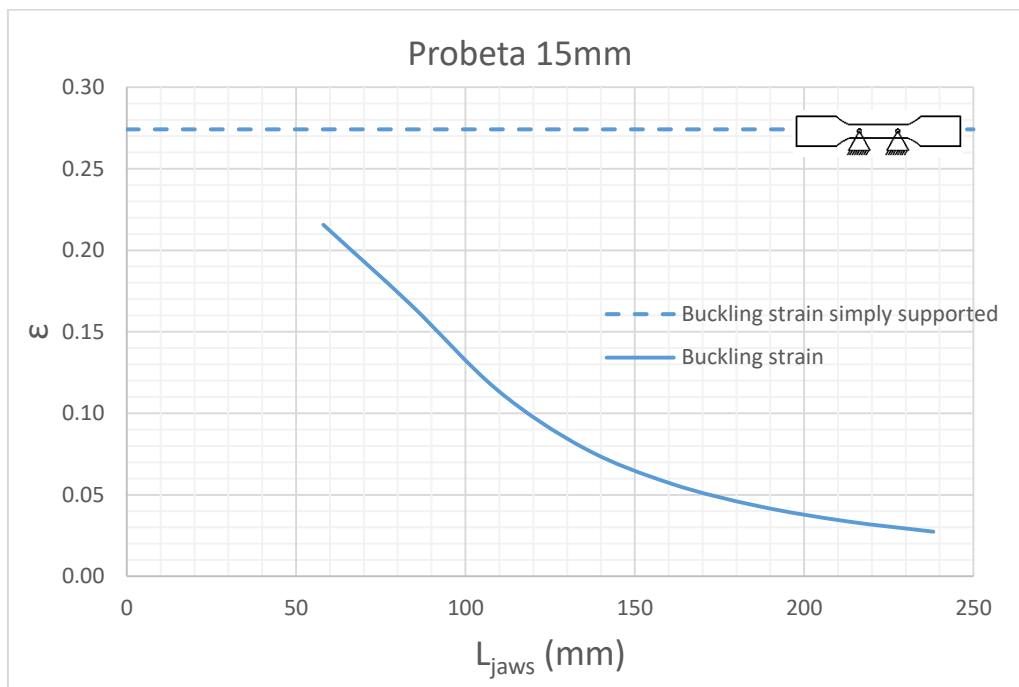


Fig. 31. Variation of strain that would cause buckling at different lengths between jaws.

As it is shown in the previous chart (fig. 31), the final coupon also fulfils the criteria preventing buckling for a coupon span of up to around 115mm at 10% strain.

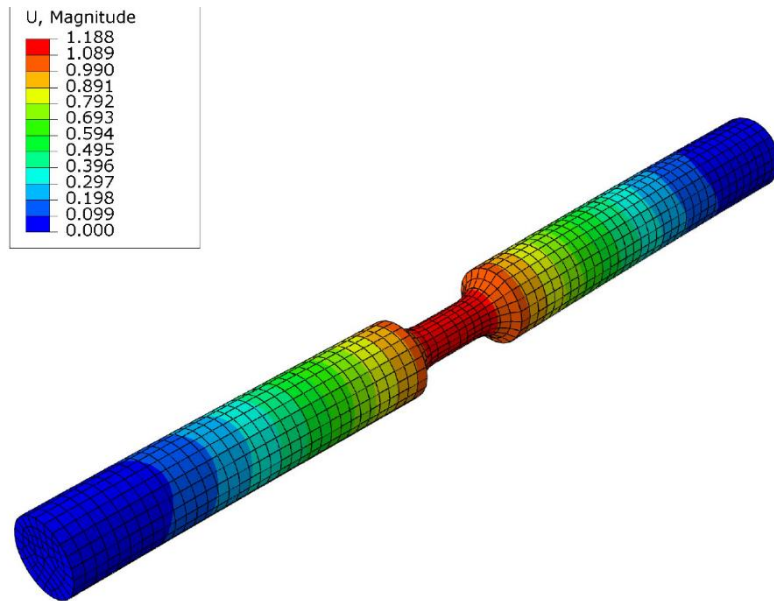


Fig. 32. Example of a buckling analysis results.

Finally, taking into account previous studies, the characteristics of the test apparatus, the load, strain, and displacement from the buckling analysis, the strain amplitude required for the test, and the coupon provider, the final dimensions of the test coupon are established and shown in figure 33. As a result, the actions applied in the test is far from the ones that would cause its buckling.

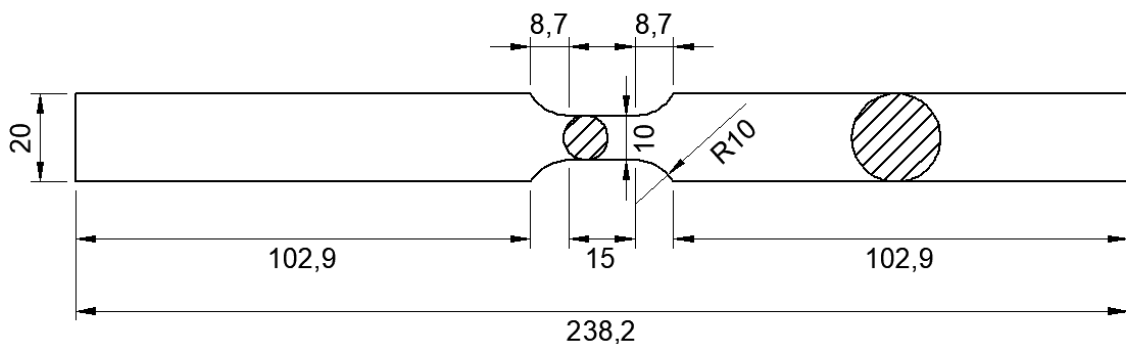


Fig. 33. Dimensions of the designed test coupon (in mm).

4.2. Instrumentation

In this section, all the equipment necessary to perform the tests is described.

Instron 8803

Instron 8803 is a versatile servo-hydraulic axial fatigue testing system with two-column load frame and an actuator of up to 500kN. It performs static and dynamic tests on materials and components providing complete testing solutions to satisfy the needs of advanced materials and component testing, and it is suited for fatigue testing and fracture mechanics (see fig.34).

The testing machine has hydraulic sets of jaws for cylindrical coupons from 5mm to 20mm.

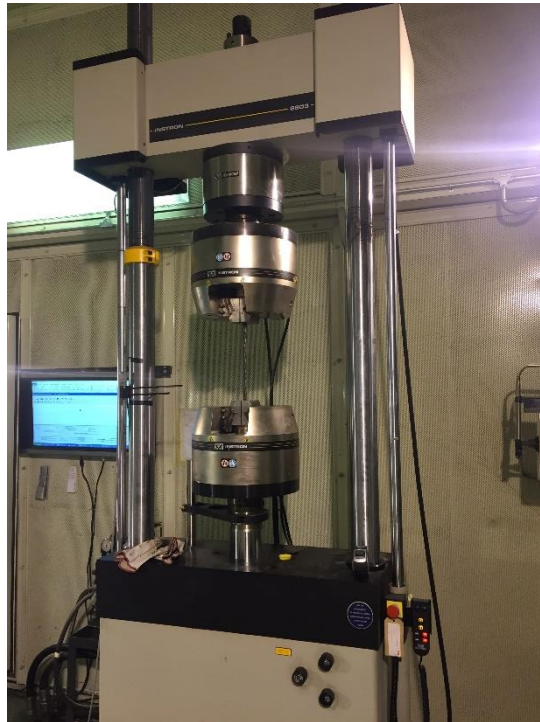


Fig. 34. Intron 8803 testing machine.

Features of interest:

- Double-acting servohydraulic actuator with force capacity up to ± 500 kN.
- High-stiffness, precision-aligned load frame with twin columns and actuator in the lower base or upper crosshead.
- Up to 250 mm of usable stroke.
- Hydrostatic bearing actuators for high side-load resistance and better alignment during testing.

Extensometer

In order to obtain the displacement applied in the test, an extensometer is set up on the test coupon (see fig.35). The extensometer used in this research project is a Clip-On Epsilon Extensometer model 3541-005M-0635M-ST which has a gauge length of 5.0mm and a measuring range of 6.35mm.

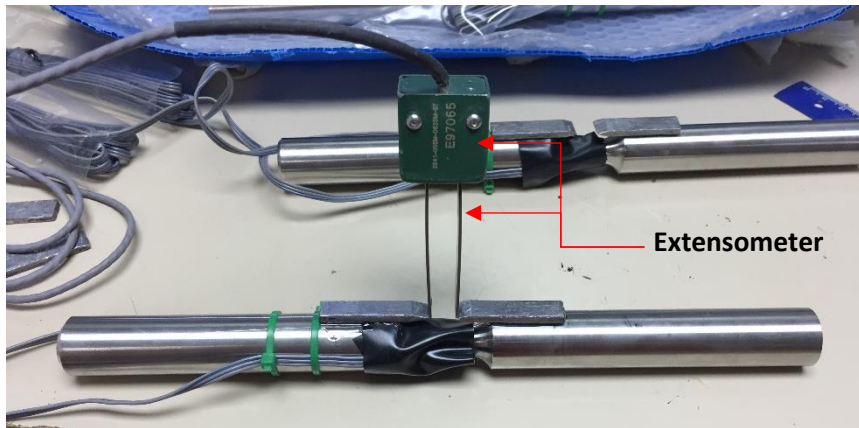


Fig. 35. Coupon with an extensometer.

Strain gauges

In this research project the strain gauges used are post-yield strain gauges model YFLA-5-3LJCT-F (see fig. 36). The gauges have a gauge length of 5mm, a coefficient of thermal expansion of $11.8 \times 10^{-6}/^{\circ}\text{C}$, an electrical resistance of $119.5 \pm 0.5 \Omega$ and a gauge factor of $2.11 \pm 2\%$. They have a strain limit of around 10 and 15% and a fatigue limit of around 100 cycles [40].



Fig. 36. Strain gauges box (left). Strain gauge (right).

Strain gauges are devices used to measure strain on an object. They are formed by small resistances made of alloys, most of them of Cu 55% y Ni 45%. The metallic threads of the gauge are attached to a support material which serves as an insulator and keeps the sensitivity of the metallic threads in one direction (See fig. 37).

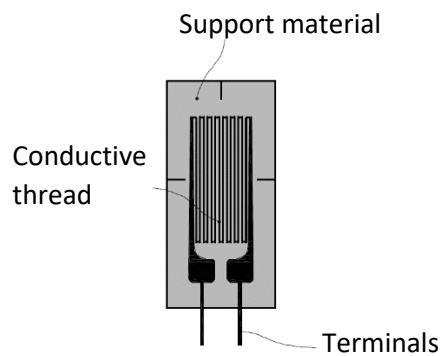


Fig. 37. Unidirectional strain gauge [41].

The gauge is in direct contact with the structure or test subject in a way that it suffers the same deformation. Basically, when the metallic thread of the gauge suffers length variations, its electrical resistance varies as well, and therefore a relationship between the strain and the resistance can be established (see fig. 38).

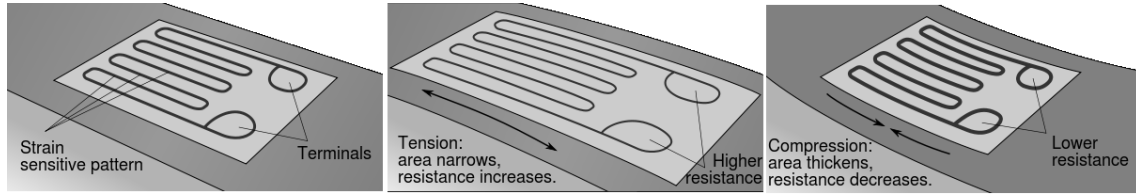


Fig. 38. Visualization of the working concept behind the strain gauge on a beam under exaggerated bending. [42]

The functioning of a strain gauge is based on the Ohm's Law where the electrical resistance of a conductor may be expressed as:

$$R = \rho \frac{L}{A} \quad (14)$$

where ρ is the electrical resistivity, L the length of the conductor and A the cross-section.

After mathematical formulations, a new expression that establishes a relationship between strain and electrical resistance is obtained and given in Eq. (15).

$$\varepsilon = \frac{1}{K} \frac{\Delta R}{R} \quad (15)$$

Where K is a constant named gauge factor that involves the Poisson's coefficient and the Bridgman constant; and $\Delta R/R$ is the variation of the resistance.

To sum up, the strain gauge is an electrical resistance that follows Ohm's law. When subjected to deformation, the materials of which the gauge is made, alter the resistance value. When compressed, the resistance is lower and in tension, the resistance is higher and with the expression Eq. 15 it is possible to establish a relationship between the electrical resistance of the strain gauge and the strain of the material from which it is attached.

Stainless steel coupons

The previously designed coupons (see section 4.1) are provided by the company Roldan/Acerinox (see fig. 40). A total of 5 coupons were provided and their dimensions (see fig. 39) were measured and shown in table 17.

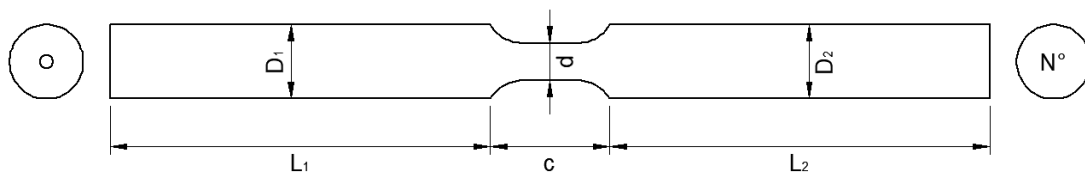


Fig. 39. Measurement nomenclature for the coupons.

Table 15. Coupon measurements.

Coupon	L ₁ (mm)	L ₂ (mm)	c (mm)	D ₁ (mm)	D ₂ (mm)	d (mm)
1	108.68	109.97	31.21	19.98	19.96	10.00
2	108.60	112.70	30.72	19.98	19.95	10.00
3	108.09	111.56	30.77	19.95	19.95	10.02
4	108.39	112.52	30.45	19.96	19.96	10.02
5	109.41	111.42	30.86	19.95	19.96	9.99



Fig. 40. Stainless steel coupons.

Data acquisition system

For data acquisition (DAQ), the system used was the MGCplus (see fig.41). The MGCplus is a DAQ system suitable for acquiring force, strain, displacement, torque, voltage, current, temperature and other parameters in a numerous kind of tests, including fatigue tests. To obtain the data, it uses connection boards with 25pin serial communication ports along with the software Catman which is meant to parameterize and visualize large number of measurements channels. Both the MGCplus and Catman are products of HBM.

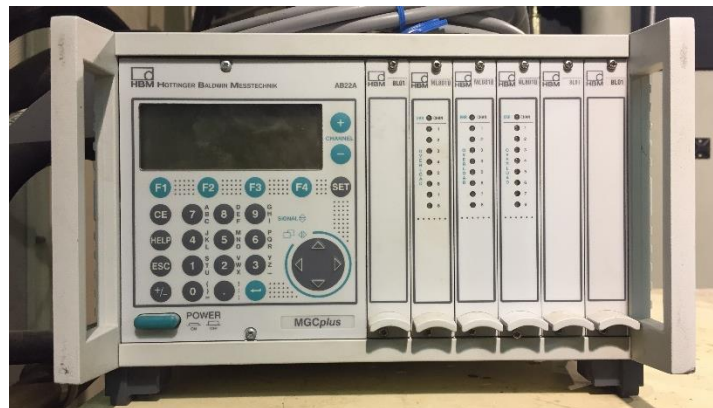


Fig. 41. MGCPlus DAQ system.

4.3. Test set up

Before proceeding to test the coupons, the strain gauges need to be placed in the reduced cross-section of the coupons. In order to do so, it is required to follow a rigorous procedure that will ensure that the strain gauge will indicate reliable and accurate measurements.

- **Surface polishing:**

The surfaces in contact with the strain gauges need to be polished. To do so, the coupon needs to be carefully hold tight with a clamp, and with a rotary tool, the surface is polished. Note that safety equipment is necessary.

It is worth mentioning that, in stainless steels, the finishing is already quite polished and therefore the polishing procedure does not require much time.



- **Surface cleaning:**

Once polished, the leftovers must be removed. A sterile gauze along with degreaser and rubbing alcohol are used to clean the surface and remove any particle. Once clean it is important to avoid touching the surface.



- **Placement of the strain gauge:**

First, it is important to notice that the gauge cannot be touched with bare hands. One way to place the gauge is attaching a cello tape in the face that does not make contact with the coupon and then placing it carefully aligning the centre of the coupon with the guidelines in the gauge. If the gauge is correctly aligned, the tape can be completely glued.

It is worth noticing that due to the dimensions of the reduced cross-section, only two strain gauges are placed per coupon.

- **Adhesion of the strain gauge:**

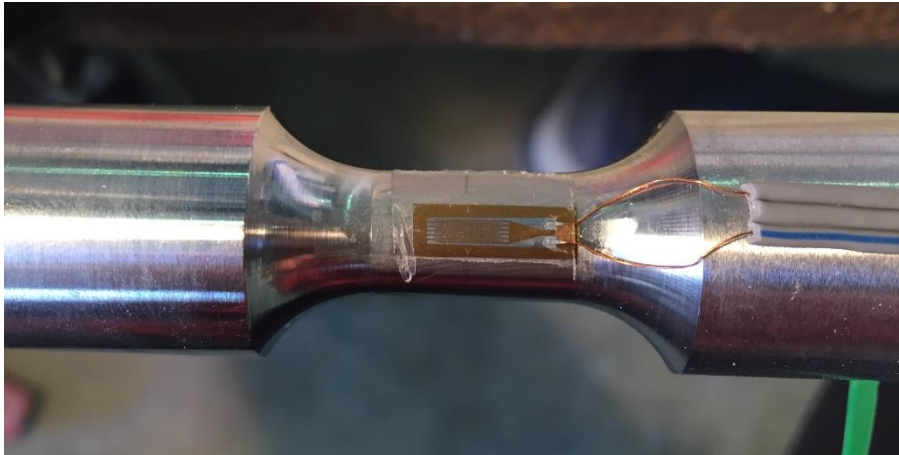
In order to adhere the gauge, a product called cyanoacrylate CN-Y is used. The tape is pulled and a drop of cyanoacrylate is placed in the centre of the gauge and then returned to its place using the previously attached tape.

- **Drying of the adhesive:**

To correctly dry the adhesive and ensure the attachment of the gauge, it is recommended to apply pressure on top of the gauge for about 4 minutes.

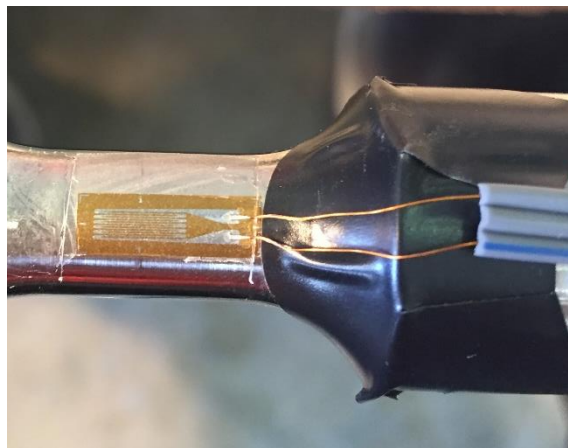
- **Extraction of the cello tape:**

To remove the tape a special care is required, the gauge can easily get stuck in the tape if the cyanoacrylate is not completely dry. If this happens, the process will need to be repeated and apply pressure for a longer time to ensure that the adhesive is dry.



- **Insulation of the strain gauge cables:**

After extracting the cello tape, it is important to insulate the part of the wires that lacks jacket. Although they already have an insulating coating, an insulating tape is used in the coupon surface to avoid any possible contact between the cables and the coupon steel.



If necessary, after completing the steps, a cable tie can be used to secure the cables and prevent the gauge from tearing off. To add the second gauge, the steps are repeated.

- **Resistance testing:**

Once all the strain gauges are in place, it is essential to test the electrical resistance to ensure that it has not been modified by placing it in the stainless steel coupon.

In order to do that, a multimeter is used. The multimeter is set up in electrical resistance measurement (Ω), the black probe gets in contact with the blue cable

and the red probe with each of the grey cables. The electrical resistance must be $119.5 \pm 0.5 \Omega$.

- **Protecting the strain gauge:**

Once the gauge is properly placed and the resistance verified, layers of covering putties are used to protect the strain gauges from the environment. The first putty is made of butyl rubber, is called SB tape and it is a moisture- and water-proofing coating for laboratory environment, it is used as a first coating. The second putty is a vinyl/mastic tyme (VM tape) and is used as a second coating also for moisture sealing.



Finally, two plates are glued to the coupon to facilitate the placement of the extensometer. The Resulting coupon is shown in figure 42.



Fig. 42. Coupon ready for testing.

Once the test coupons were properly equipped, they are ready to be tested using the previously mentioned Intron 8803 testing machine. To proceed with the testing, the machine and the coupon need to be set up following the next steps.

- **Data acquisition set up:**

First, the strain gauge cables are connected to a 25 pin serial cable using an interface breakout board as shown in figure 43 and then plugged into the connection boards of the MGCplus data acquisition system. The extensometer

and the Instron 8803 test machine outputs are plugged directly into the connection board of the MGCplus.

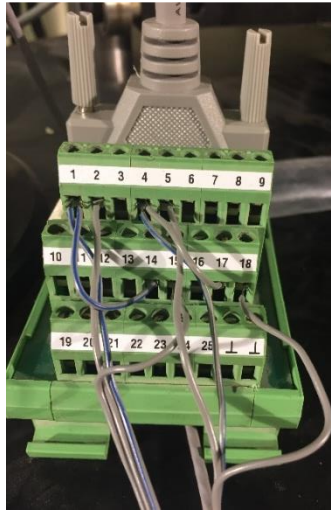


Fig. 43. 25 pin interface breakout with two strain gauges connected.

- **Placement of the coupon:**

To place the coupon in the jaws of the testing machine, first, it is important to remove the cable ties. Next, the coupon is aligned and held between the gaps of the upper jaw at the desired distance and then the upper jaw can be closed using the controller button. Note that the person holding the coupon must be the same pressing the button to avoid accidents. Subsequently, the load actuator must be set up to zero in order to compensate the weight of the jaw system and prevent any force from altering the coupon at the moment of closing the lower jaw.

Once the load is set to zero the lower jaw is closed.

- **Securing the cables:**

Once the test coupon is held by the machine, the cables of the sensors are secured to the machine with a cable tie avoiding them from being accidentally pulled during the test.

- **Attaching the extensometer:**

The extensometer is placed in the coupon using the previously attached plates as shown in figure 44.



Fig. 44. Coupon with extensometer set up in the instron 8803.

These steps grant the precise acquisition of data as well as safety measures.

4.3.1. Graphical user interface (GUI) of the testing machine software

The software used to control the testing machine is called WaveMaker. In this software, each test protocol is established and divided by blocks, in this case, the machine is controlled either by the displacement or by the strain from the strain gauge and each block contains either a displacement rate (speed) or a strain rate. In the user interface (UI) it is shown the values of the load, displacement and strain in real time, thus this values can be monitored while testing (see fig. 45).

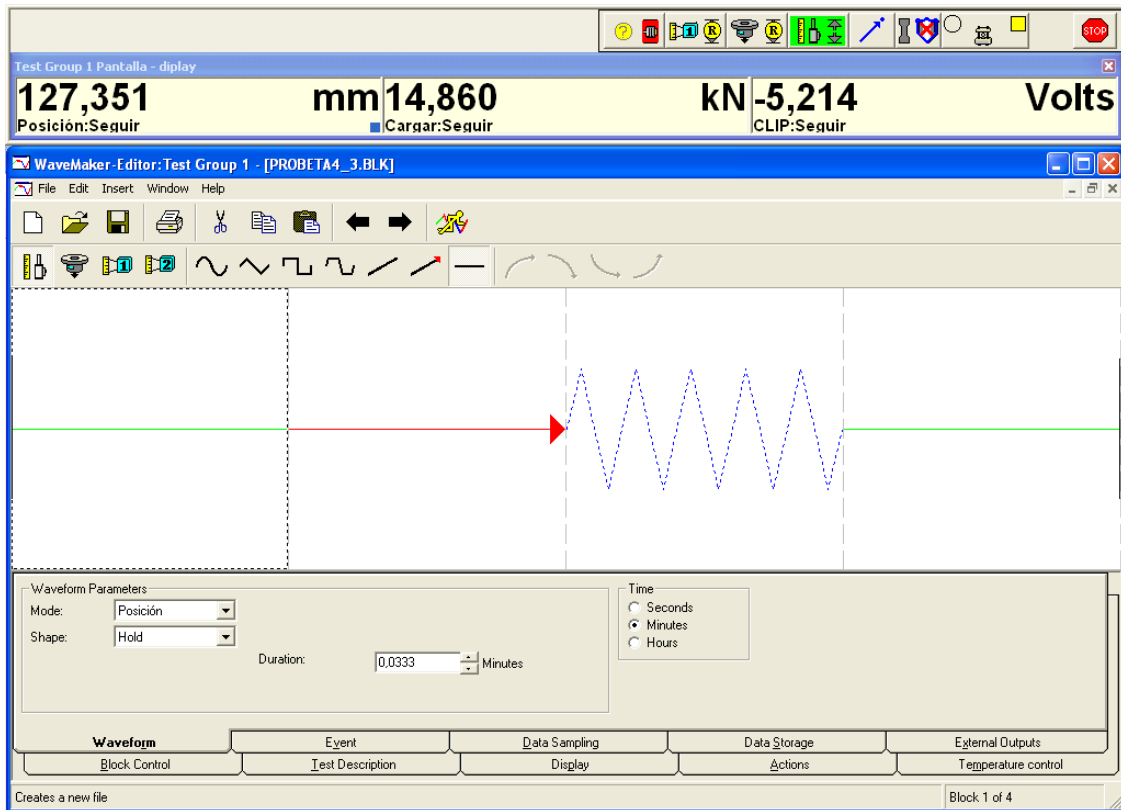


Fig. 45. Screenshot of the testing software WaveMaker.

4.3.2. Loading protocols

Due to the limited number of coupons, the loading protocols employed are dependent on this factor. One of the coupons is destined to a monotonic axial test, this leaves four coupons for the cyclic testing.

The first protocol corresponds to a monotonic tensile test; the second, third and fourth protocols correspond to low-cycle fatigue tests using the companion method at strain amplitudes of $\pm 5\%$, $\pm 3\%$ and $\pm 1\%$ respectively; and the fifth protocol consists of cycle testing using the multiple-step method going through strain amplitudes of $\pm 0.5\%$, $\pm 0.75\%$, $\pm 1\%$, $\pm 2\%$, $\pm 3\%$, $\pm 4\%$ and $\pm 5\%$.

It is important to ensure that the heat generated during the test does not significantly affect the results, therefore the test speed should not exceed a certain value. For the axial monotonic tensile test, the speed selected is the one proposed by Huang and Young [43] for ductile materials (see table 16). With the speeds defined, the loading protocol is established as shown in figure 46.

Table 16. Loading Rates [43].

Strain %	Loading rate (mm/min)
~0-0.15	0.05
0.15-0.5	0.8
0.5	Paused 100s
0.5-2.5	0.8
2.5	Paused 100s
2.5-fracture	0.8

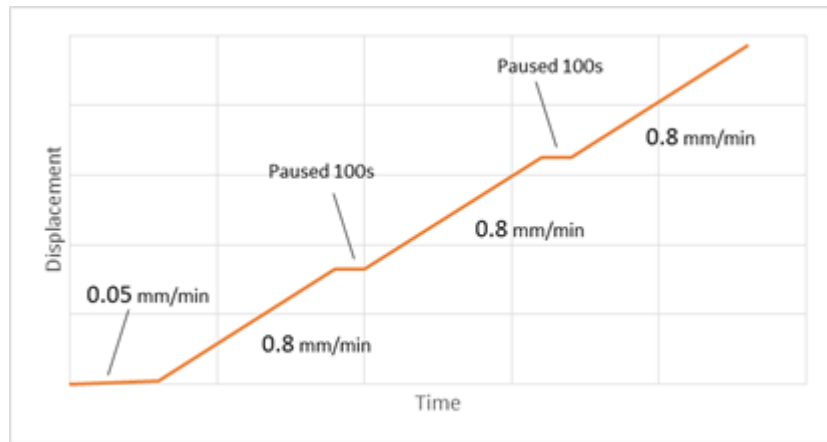


Fig. 46. Loading protocol scheme. First Protocol.

For the rest of the tests, which are strain controlled, the strain rate used to minimize the effect of the temperature is 0.001/s. It is worth noticing that this strain rate is obtained evaluating the previous studies (see section 2.3).

The second, third and fourth protocols consist of repeating cycles of tension and compression at a constant strain amplitude until the fracture of the coupon. The second protocol has a strain amplitude of $\pm 5\%$ strain, the third protocol has a strain amplitude of $\pm 3\%$ and the fourth protocol has a strain amplitude of $\pm 1\%$. In fig. 47 a scheme of the protocols is shown.

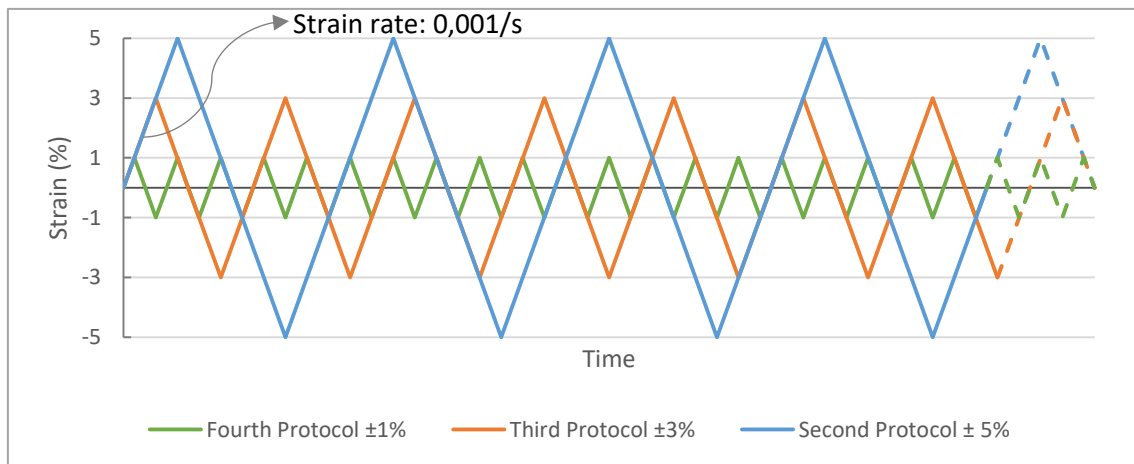


Fig. 47. Companion method loading protocols.

The last protocol consists of step-wise increasing strain amplitude cycles with 10 cycles performed at each amplitude as seen in fig. 48.

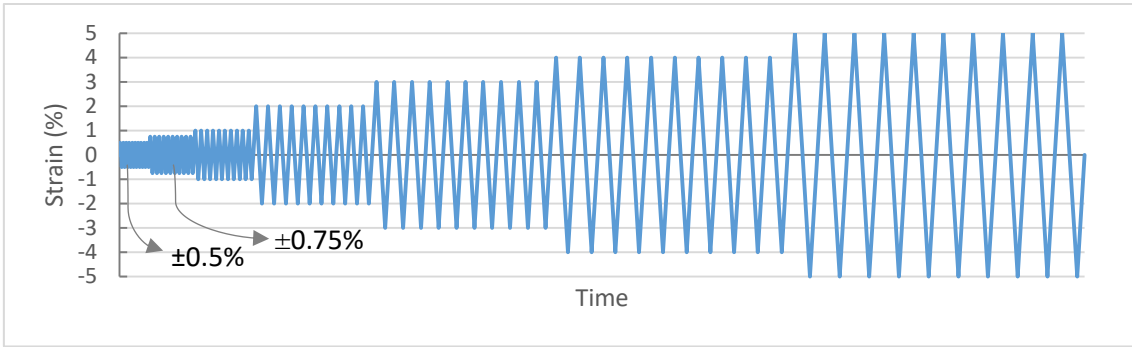


Fig. 48. Fifth loading protocol. Multiple-step method.

Once the loading protocol input is ready, the button “Run” is pressed in the software Wavemaker and the test begins. It is important, before running the test, that the catman software is ready to obtain all the data at the desired frequency.

5. EXPERIMENTAL RESULTS

This chapter presents the result obtained during the test. The results are analysed and formerly, relevant information and properties like a cyclic stress-strain curve and Young's modulus are extracted.

5.1. Test results

First, it is important to highlight that strain-controlled cyclic tests have never been done before in the Structural Technology Laboratory in the Department of Civil and Environmental Engineering at UPC, and the calibration needed for the testing machine to be able to be controlled by a strain gauge (which does not belong to the testing system), was a challenge for the technicians and the researchers involved in this experimental study.

In this section, a brief description of the test development is presented followed by the test results. For an adequate representation of the results, stress-strain curves and data history charts are plotted.

First test: Monotonic tensile

The monotonic tensile test is a common test performed in the laboratory. In this case, the extensometer and strain gauges will reach their limits before fracture. Nevertheless, load and displacement data are measured by the testing machine throughout the whole test.

The coupon behaviour was monitored with a real-time load-displacement chart, and it showed the expected behaviour till the fracture (see fig. 53 and 54). In the following figures the data obtained during the test is plotted.

In figure 49 and 50, the non-linear behaviour of stainless steel can be appreciated; nonetheless, a relatively linear behaviour is shown at the beginning. The material shows a considerable strain hardening and high ductility. The test has a peak load of 53kN (around 675 MPa of ultimate stress) and a load of 36kN at fracture (a stress of 458 MPa at rupture).

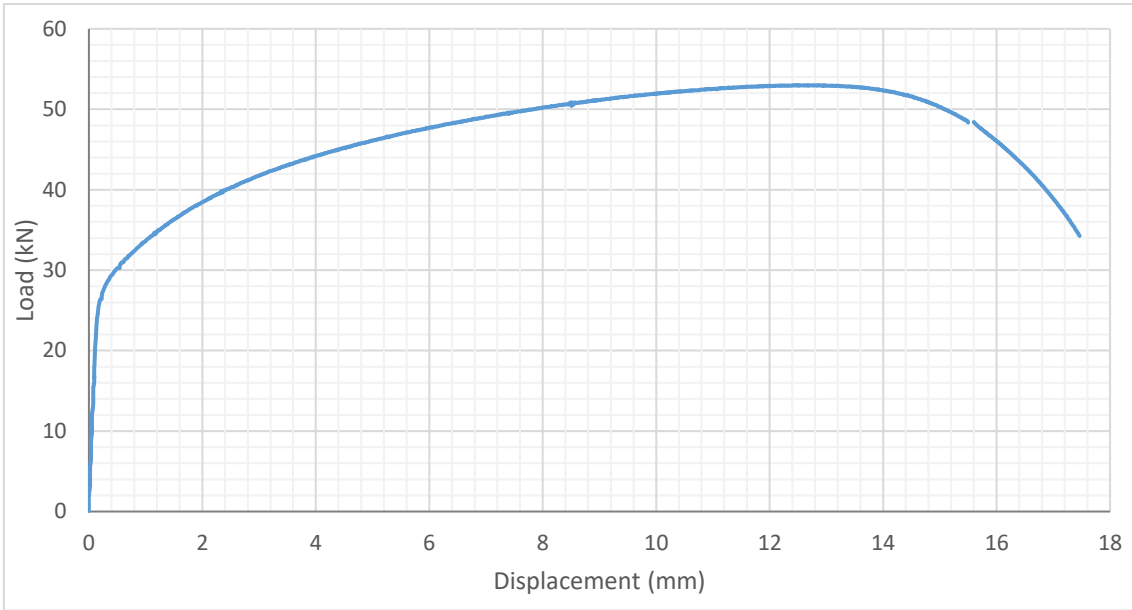


Fig. 49. Load-displacement curve of tensile test. Displacement obtained from the testing machine.

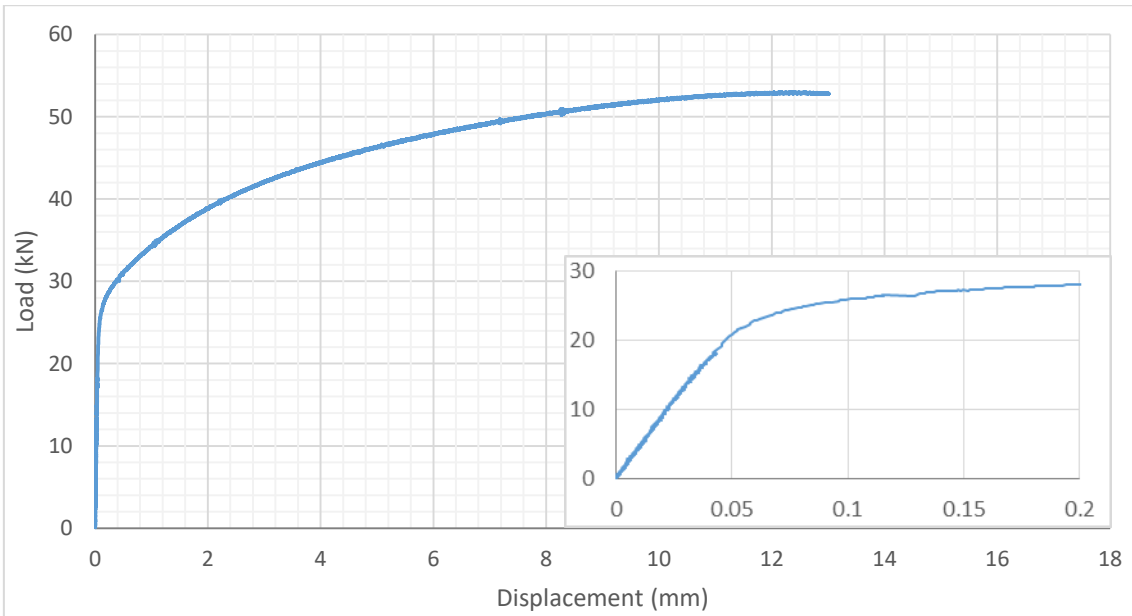


Fig. 50. Load-displacement curve of tensile test. Displacement obtained from the extensometer until its limit.

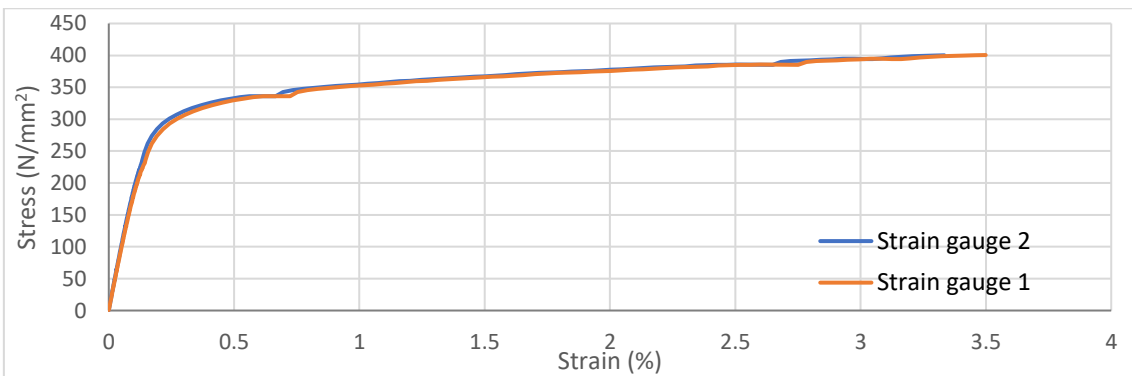


Fig. 51. Stress-strain curve of tensile test. The curve is plotted until the strain gauge fails.

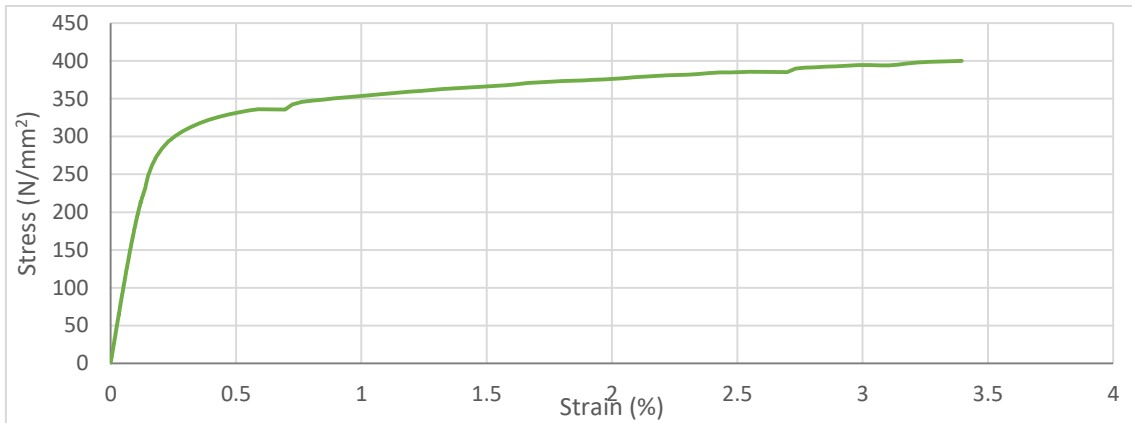


Fig. 52. Stress-strain curve of tensile test with mean values of the strain gauges.

The stress-strain curve shown in figure 52 consists of mean values from the two strain gauges plotted in figure 51 and will be used to obtain the Young's Modulus (E) and the yield strength ($\sigma_{0.2}$).

In the following figures (fig. 53 and 54) the fracture of the coupon is appreciated, in figure 54 a comparison with another coupon is made in order to observe the elongation and the necking.



Fig. 53. Fractured coupon. Monotonic tensile test.



Fig. 54. Tested coupon in contrast with another coupon.

Second test: Cyclic companion $\pm 5\%$

As mention before, the second test consists of cycles at a constant strain amplitude of $\pm 5\%$.

Once the coupon was placed in the Instron 8803 and ready to test, the test protocol was executed. A few seconds after the loading block started, the testing machine performed an abrupt tension load fracturing the coupon immediately resulting in a failed test (see fig.55).



Fig. 55. Fractured Coupon from failed test.

It was figured out that the error was due to a discrepancy between the strain value variation and the load variation, basically, if the load is ascending the strain gauge value must ascend too. If this is not the case (like in the failed test) it can be fixed by switching the +/- cables of the gauge.

After this incident, the tests were rethought and it was decided that the **fourth test would be discarded** and only two tests will be performed at constant strain amplitude, at $\pm 5\%$ and $\pm 3\%$.

Considering the above, the second test has been tried again. This time the test started successfully and 5 cycles were completed until the strain gauge showed a value out of range.

A strain value out of range normally means that the coupon fractured but, when extracting it, the coupon was unaltered to the naked eye and the strain gauges seem to be in good condition (see fig. 56)



Fig. 56. Strain gauges still attached to the coupon after the second test.

It was speculated that the error in the strain gauge value was due to the adhesive being too fragile for cycles at a strain of that magnitude. Nonetheless, in the manufacturer's strain gauges catalogue [40], it is shown that the YF strain gauge series has a fatigue limit of 100 cycles, therefore the reason why the strain gauge did not work remained uncertain.

As the coupon didn't fracture, the material is strengthened, so an attempt to continue the test using a two-component EA-2A adhesive was made. This adhesive takes longer to dry and an oven is needed. By the time the adhesive was dry, it was clear that the strain gauge was not making contact with the coupon and therefore the attempt was discarded (see fig. 57). This may be due to the long drying process and the thick and slippery characteristic of this adhesive.



Fig. 57. Strain gauge attached with two component EA-2A adhesive.

Despite this, the data from the 5 cycles were extracted and used in FE in this research project. The following results are obtained.

Figure 58, shows the values of strain given by the strain gauge employed to control the test. As it can be seen, the strain kept a constant amplitude of $\pm 5\%$ and each cycle takes 200 seconds corresponding to the 0,001/s strain rate. A total of 5 cycles were completed until the strain gauge failed.

Figure 59 shows the data from both strain gauges as a sort of comparative data. Although the secondary gauge started showing values out of range at around 3.5%, it continued showing coherent values when returning to this same strain and therefore creating a gap. When comparing both curves, even though there is missing data, their behaviour is almost identical. It can also be noted that the strain at which the control strain gauge failed was around the same value as that of the secondary strain gauge.

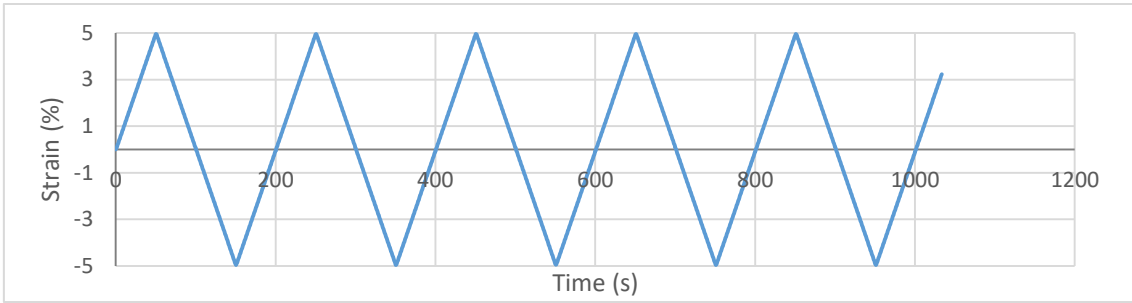


Fig. 58. Strain history of control strain gauge. Companion method. $\pm 5\%$ strain amplitude.

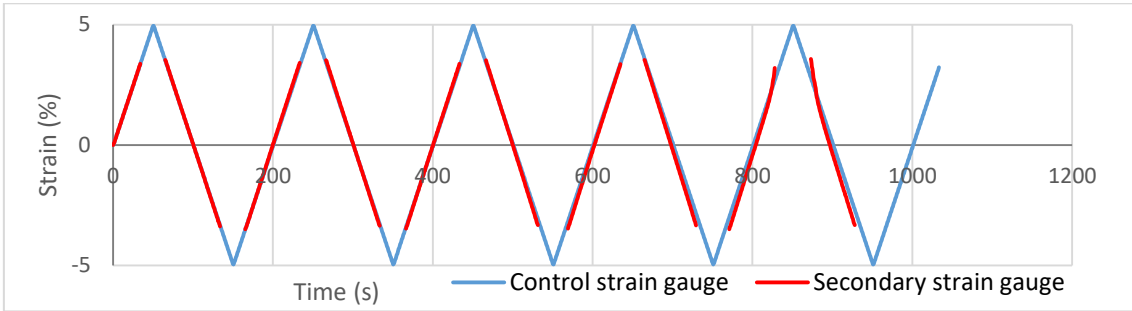


Fig. 59. Strain history of both strain gauges. Companion method. $\pm 5\%$ strain amplitude.

Figure 60 and 61 shows the displacement applied to the coupon throughout the test. The data obtained from the extensometer is considered more accurate and the data obtained from the test machine is used for reference only.

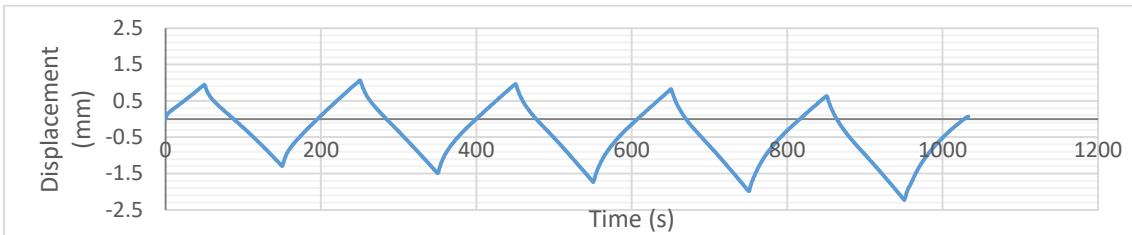


Fig. 60. Displacement history of the Instron test machine. Companion method. $\pm 5\%$ strain amplitude.

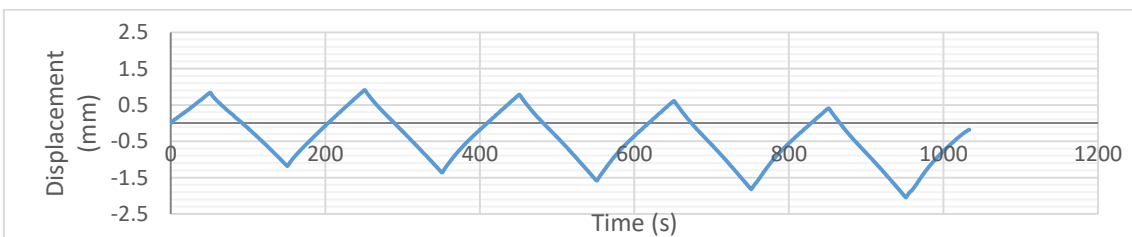


Fig. 61. Displacement history of the extensometer. Companion method. $\pm 5\%$ strain amplitude.

As it can be seen, not only the displacement deviates from the X axis, but also its amplitude increases with each cycle.

In figure 62 and 63, a strong cyclic hardening is observed with the fifth cycle presenting a peak stress close to five times the first peak stress. Stabilisation has not been reached meaning it can be strengthened more. Another important observation is that the mechanical behaviour varies in tension and compression i.e. asymmetric behaviour; in compression, the peak stresses are higher than in tension.

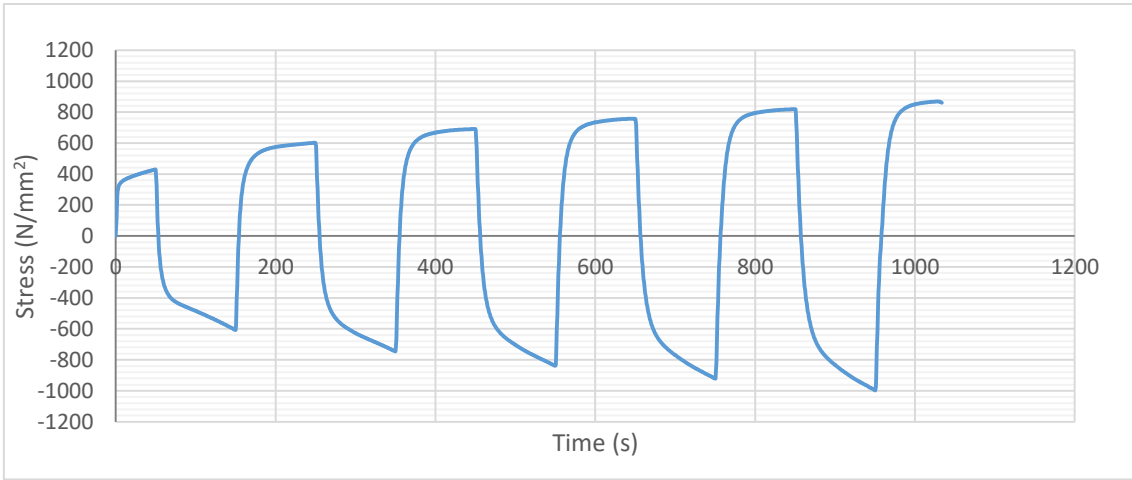


Fig. 62. Stress history. Companion method. $\pm 5\%$ strain amplitude.

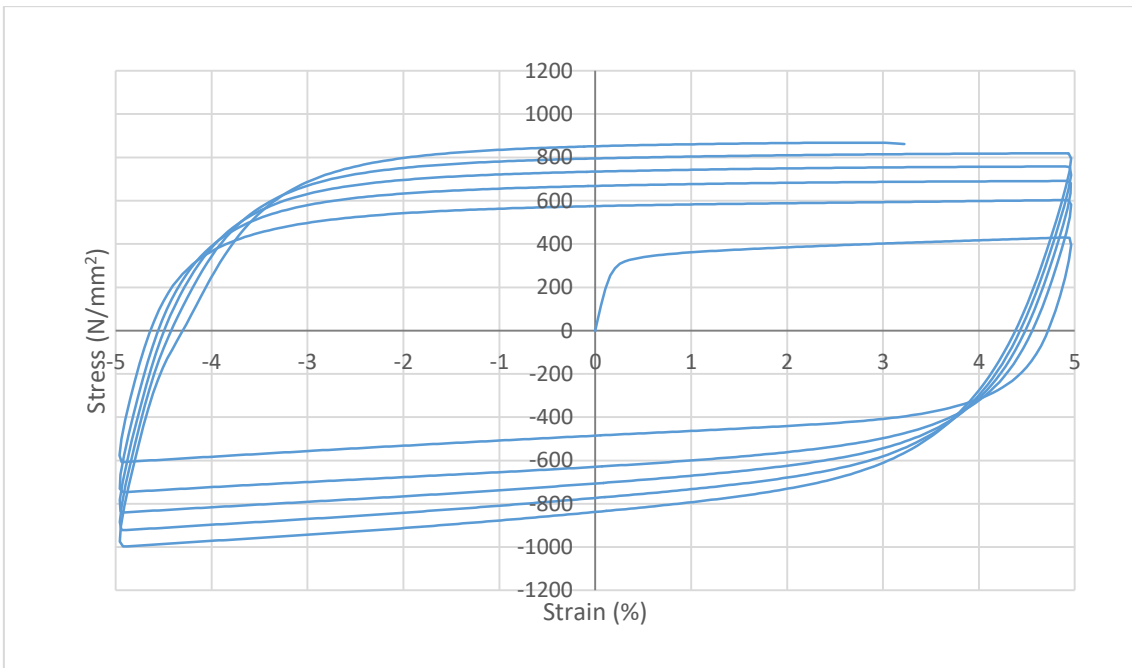


Fig. 63. Strain-Stress curve. Companion method. $\pm 5\%$ strain amplitude.

Figure 64 shows the difference between peak tensile stresses in each cycle. Although only 5 cycles were completed, the peak stresses have large differences from one cycle to another, indicating a considerable level of hardening.

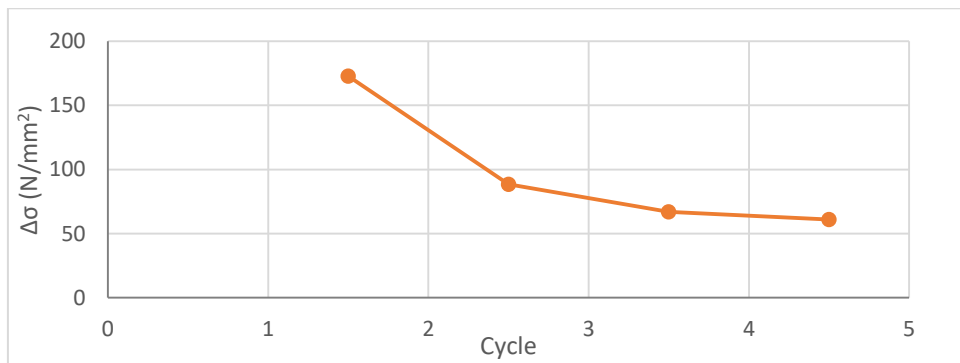


Fig. 64. Variation of peak stresses between cycles. Companion method. $\pm 5\%$ strain amplitude.

Third test: Cyclic companion $\pm 3\%$

Similar to the previous test, the third test was set up at a constant strain amplitude of $\pm 3\%$. After verifying that the load and the strain values were “compatible”, the test was started. The test machine performed 20 successful cycles until the strain gauge showed a value out of range.

After extracting the coupon it was noticed that both the coupon and the strain gauge controlling the test were apparently in a good state, this means that the strain gauges are failing prematurely.

In this case, in order to continue, strain gauges were attached again with the same adhesive (CN-Y) and 6 more cycles could be completed until the same issue occurred.

In total, the coupon was subjected to 26 cycles at a strain amplitude of $\pm 3\%$ without fracturing.

The results are divided into two parts; part 1 corresponds to the first 20 cycles and is exhibited in the charts in blue, and the part 2 corresponds to the followed 6 cycles and is represented in orange.

As the third test is similar to the previous test, the results show the same behaviour. Figure 65, shows the strain kept constant at an amplitude of $\pm 3\%$ and it can be seen that each cycle takes 120 seconds corresponding to the 0,001/s strain rate. A total of 26 cycles (20 in part 1 + 6 in part 2) were completed.

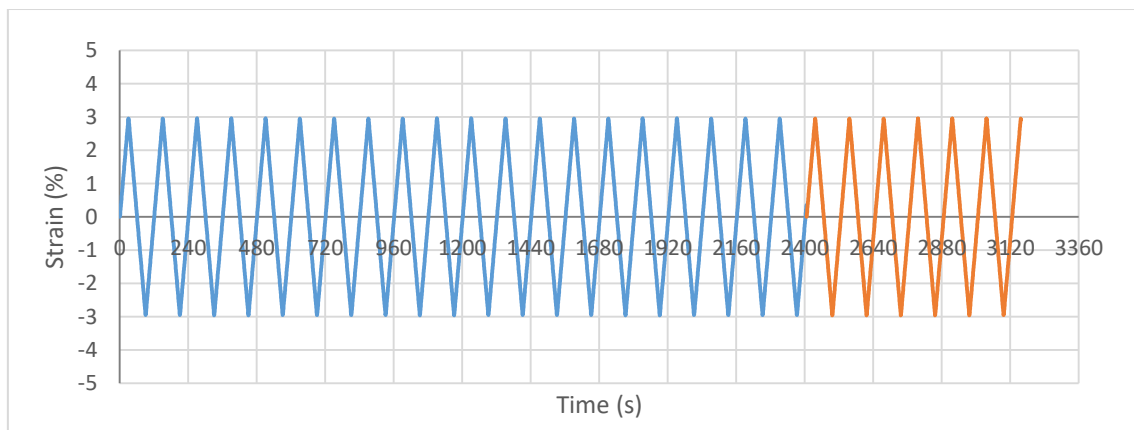


Fig. 65. Strain history of control strain gauge (part 1 + part 2). Companion method. $\pm 3\%$ strain amplitude.

Figure 66 shows the data from the secondary strain gauges. In part 1 the data does not correspond with the control gauge, this may be due to a bad attachment of the gauge. After the test, when extracting the protective coating, the secondary gauge was separated from the coupon, something that did not happen with the control gauge nor in the previous test. In part 2, the secondary strain gauge presents the same issue as the gauges in the previous test, but in this case, the missing data is larger. A comparison between strain gauges could not be made.

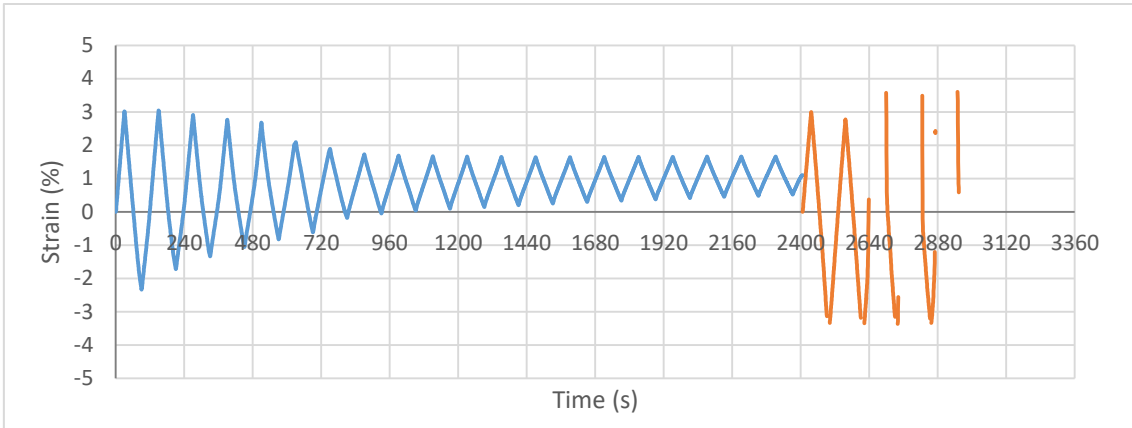


Fig. 66. Strain history of secondary strain gauge (part 1 + part 2). Companion method. $\pm 3\%$ strain amplitude.

Figure 68 and 69 shows the displacement applied to the coupon throughout the test. As well as in the previous test, not only the displacement deviates from the X axis, but also its amplitude increases with each cycle.

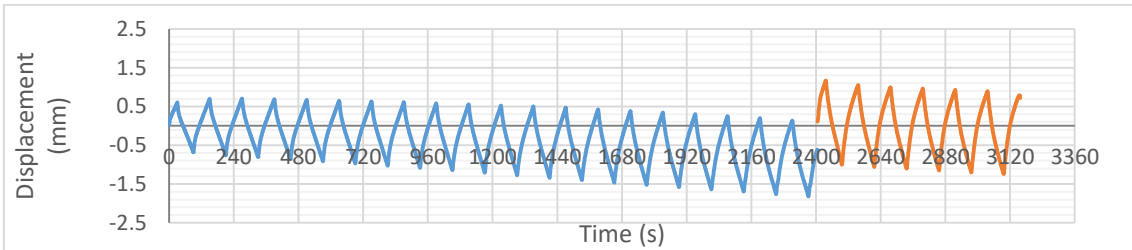


Fig. 67. Displacement history of the Instron test machine. Companion method. $\pm 3\%$ strain amplitude.

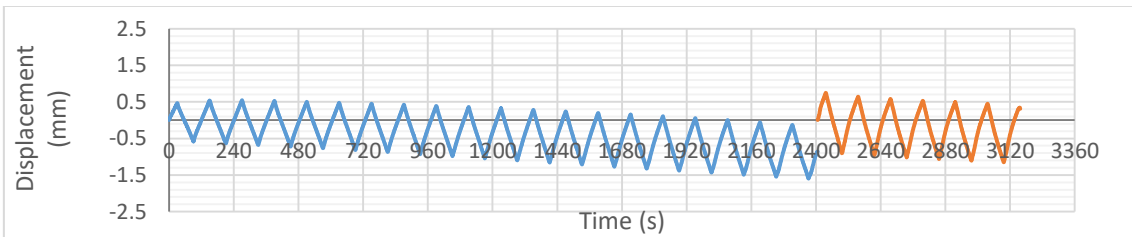


Fig. 68. Displacement history of the extensometer. Companion method. $\pm 3\%$ strain amplitude.

In figures 69 and 70, a strong cyclic hardening is observed; the last peak stress is considerably higher than the first peak stress. It is considered that the hysteresis loops reach stabilization. In this test, the asymmetric behaviour is also presented.

In figure 70, in part 1, a change of slope from the previous test is observed when unloading from compression to tension. In part 2, this change of slope is not observed which implies that this behaviour could be an error from the test machine or the strain gauge.

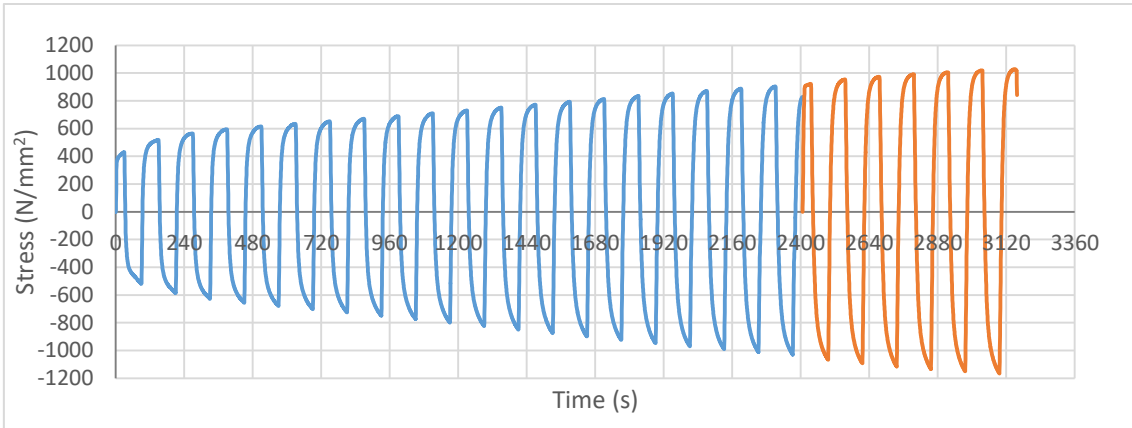


Fig. 69. Stress history (part 1 + part 2). Companion method. $\pm 3\%$ strain amplitude.

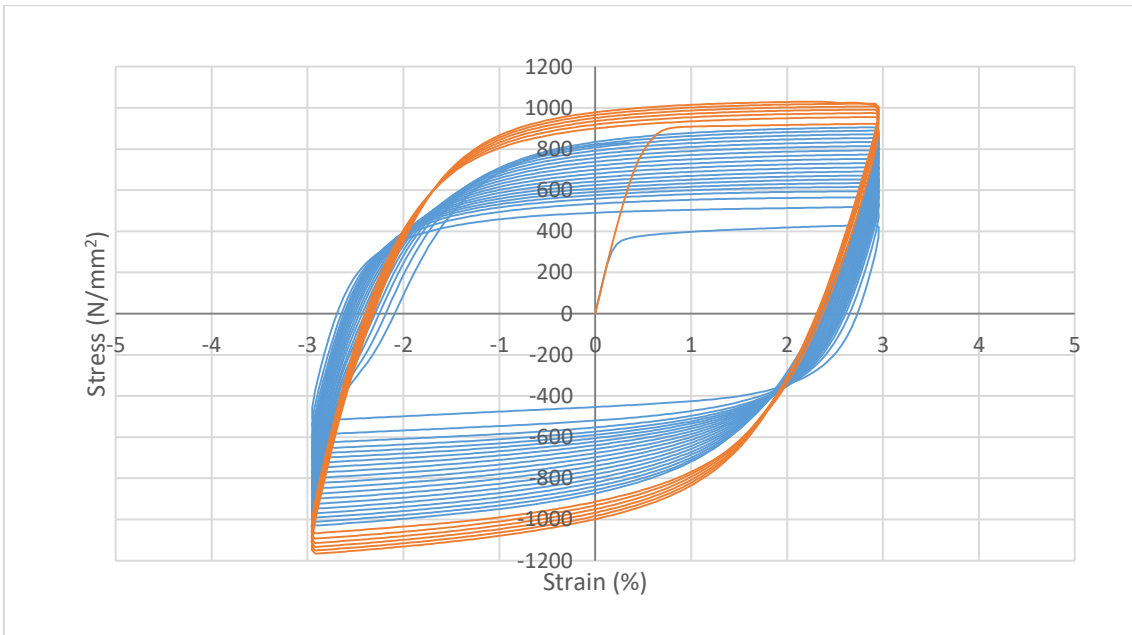


Fig. 70. Strain-Stress curve (part 1 + part 2). Companion method. $\pm 3\%$ strain amplitude.

In figure 71, it can be seen that in the first cycles the peak stresses have large differences but are gradually reduced, after about 6 cycles the differences become fairly constant, and therefore considered stable. An unusual peak is observed between cycle 21 and cycle 22, probably due to the fact that the test is divided into two parts.

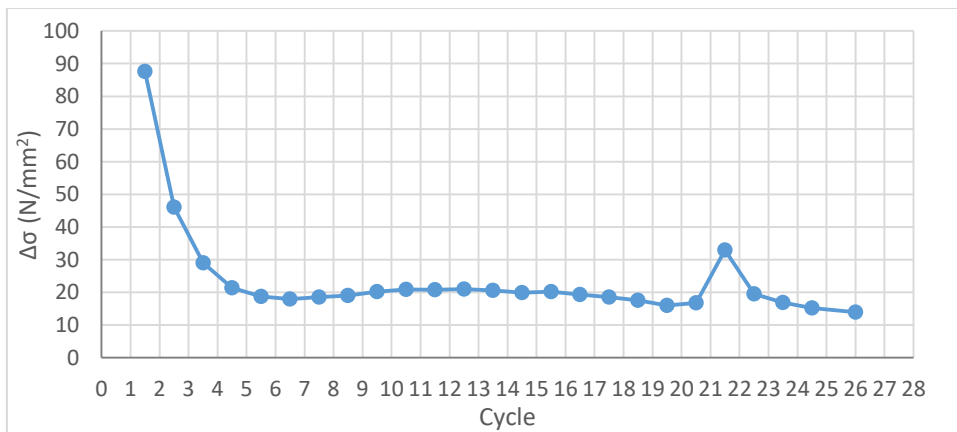


Fig. 71. Variation of peak stresses between cycles. Companion method. $\pm 3\%$ strain amplitude.

Fourth test: Cyclic companion $\pm 1\%$

As explained before, the fourth test was discarded due to the unexpected failure of one of the coupons.

Fifth test: Cyclic multiple-step

As mentioned before, the fifth test consists in a cyclic test using the multiple-step method, going through strain amplitudes of $\pm 0.5\%$, $\pm 0.75\%$, $\pm 1\%$, $\pm 2\%$, $\pm 3\%$, $\pm 4\%$ and $\pm 5\%$.

Considering the previous tests, the results of this test were somewhat better. 53 cycles were completed covering the strain amplitudes of $\pm 0.5\%$, $\pm 0.75\%$, $\pm 1\%$, $\pm 2\%$ and $\pm 3\%$ completely and 3 cycles of $\pm 4\%$. In agreement with the previous tests, the coupon did not fracture.

The following results are obtained.

Figure 72 shows the values of strain given by the strain gauge employed to control the test. As it can be seen, the test kept a constant 0,001/s strain rate while going through all the different strain amplitudes. The blocks of $\pm 0.5\%$, $\pm 0.75\%$, $\pm 1\%$, $\pm 2\%$ and $\pm 3\%$ of amplitude were tested completely plus 3 cycles of $\pm 4\%$ amplitude.

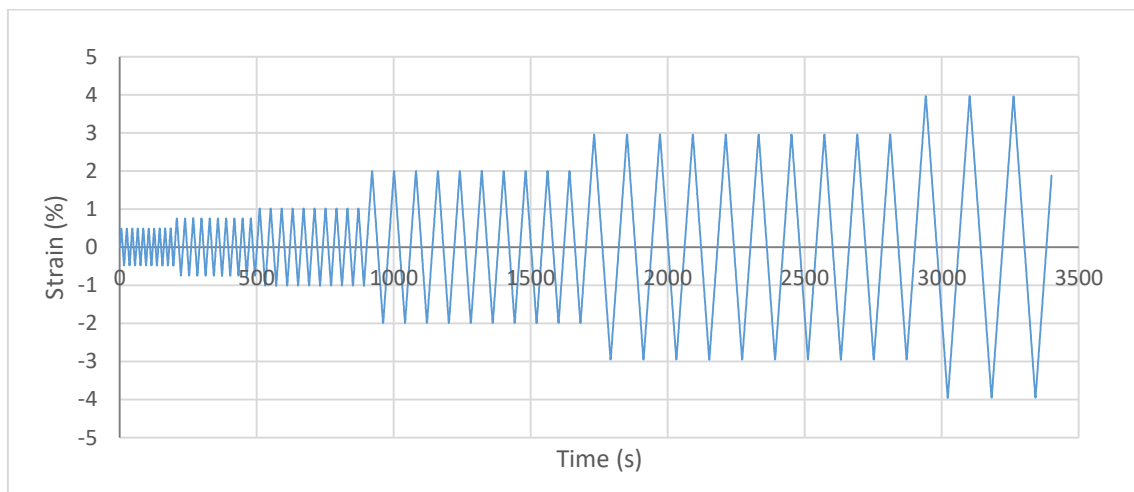


Fig. 72. Strain history of control strain gauge. Multiple-step method.

Figure 73 shows the data from both strain gauges as a sort of comparative data. Both curves follow almost identical paths. The secondary strain gauge showed values out of range in the last three cycles similarly to the second test.

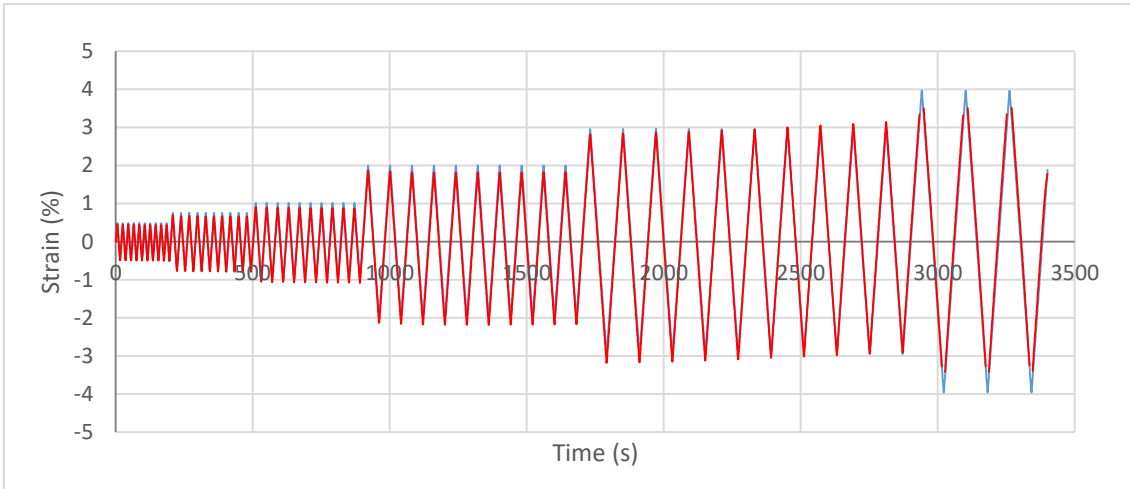


Fig. 73. Strain history of both strain gauges. Multiple-step method.

Figure 74 and 75 show the displacement applied to the coupon throughout the test. The displacement deviates from the X axis and its amplitude increases at each cycle.

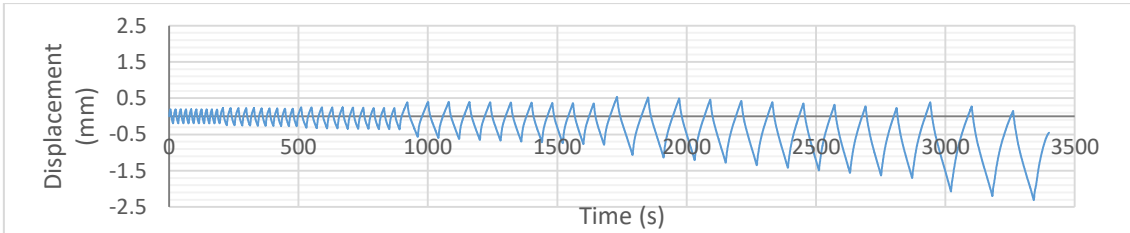


Fig. 74. Displacement history of the Instron test machine. Multiple-step method.

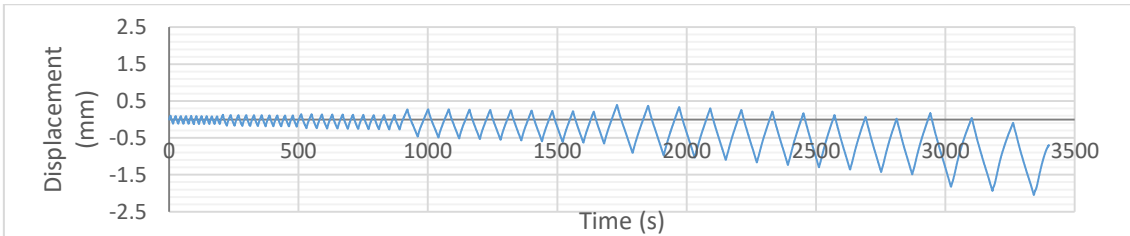


Fig. 75. Displacement history of the extensometer. Multiple-step method.

In figure 76 and 77, a cyclic hardening varies at each amplitude. At strain amplitudes of $\pm 0.5\%$, $\pm 0.75\%$ and $\pm 1\%$ the cyclic hardening is minimum and the loops are stable starting from the second cycle. At $\pm 2\%$, a considerable cyclic hardening and a clear stabilization through the cycles are observed. At $\pm 3\%$, the behaviour is comparable to the previous test. Strong cyclic hardening is observed and more plastic strain seems to be needed in order to reach stabilization. Insufficient data is obtained at $\pm 4\%$, but it is observed a stronger cyclic hardening at the first cycles. In this test, the asymmetric behaviour is also presented.

In figure 77, the change of slope, observed in the last tests, has appeared again in the last block of cycles. This change of slope seems to be related to relatively high strain amplitudes and to the number of cycles.

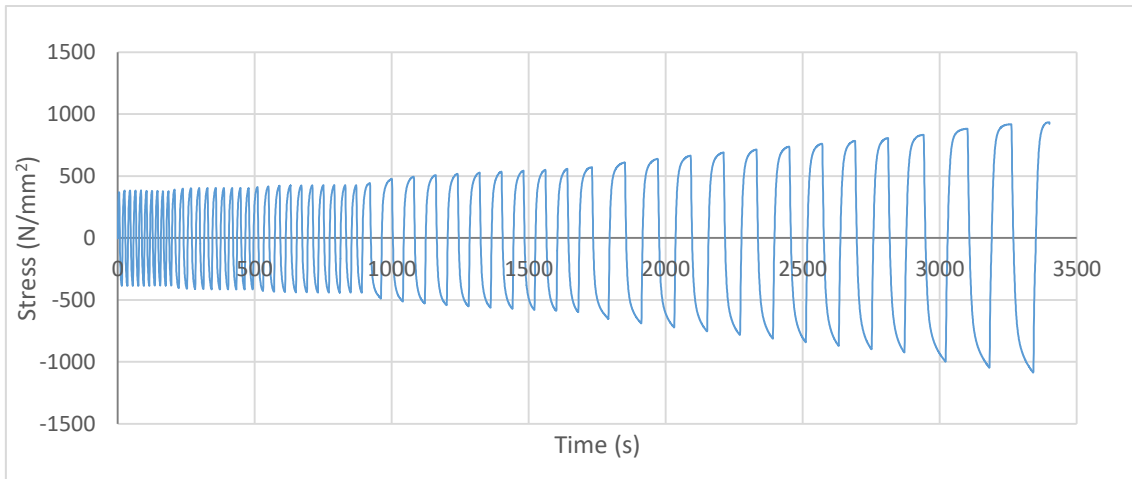


Fig. 76. Stress history. Multiple-step method.

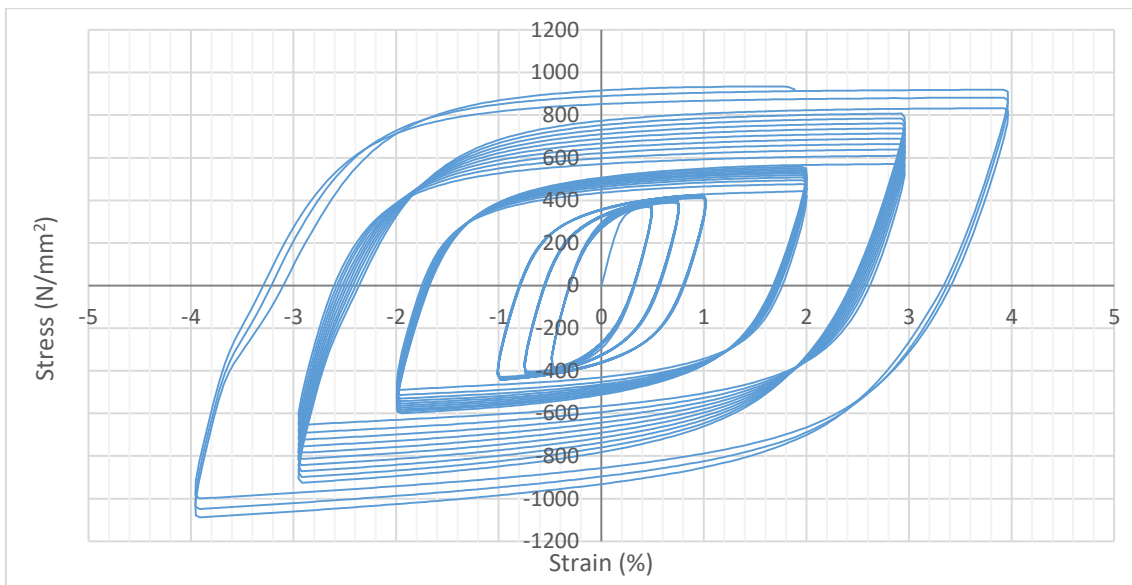


Fig. 77. Stress-strain curve. Multiple-step method.

Figure 78 shows the difference between peak tensile stresses in each cycle. As it can be seen, in the lower strain amplitudes ($\pm 0.5\%$, $\pm 0.75\%$ and $\pm 1\%$), the difference in the peak stresses is very low and the behaviour remains stable starting from the second cycle. On the other hand, for $\pm 2\%$ and $\pm 3\%$, the difference between peak stresses is higher and is reduced gradually each cycle.

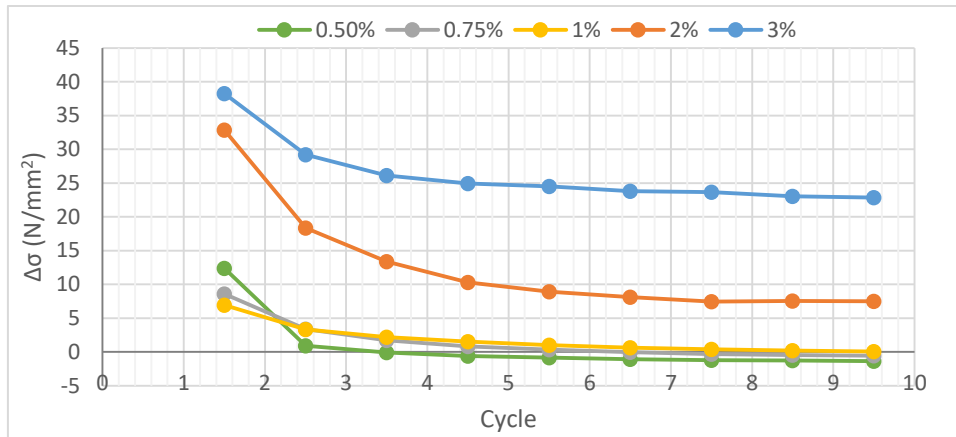


Fig. 78. Variation of peak stresses between cycles. Multiple-step method.

5.2. Results discussion

First, it is important to highlight that the tests were affected by premature failure of the strain gauge and the cyclic tests were unable to reach the failure of the specimen. Nevertheless, general aspects of the tests are listed below.

- It is observed that cyclic hardening, as well as the number of cycles needed to reach stabilization, increases with strain amplitude.
- Differences between tension and compression stresses are present in each test; this means that the material has an asymmetric behaviour.
- Displacement drift is observed in all cyclic tests, this may be due to cross-section area reduction and plastic deformation.
- It is observed that at constant strain amplitude, the displacement amplitude increases with each cycle.
- An unexpected change of slope is observed at the end of each test. The reason for this behaviour is uncertain, but it is guessed that this may possibly be due to the testing machine or the strain gauge.
- In the multiple-step test, “Masing” effect can be observed in the first 3 blocks (strain amplitudes of $\pm 0.5\%$, $\pm 0.75\%$ and $\pm 1\%$) this means that the hysteresis loops at different strain ranges coincide if they are plotted in a relative coordinate system (see fig. 79).

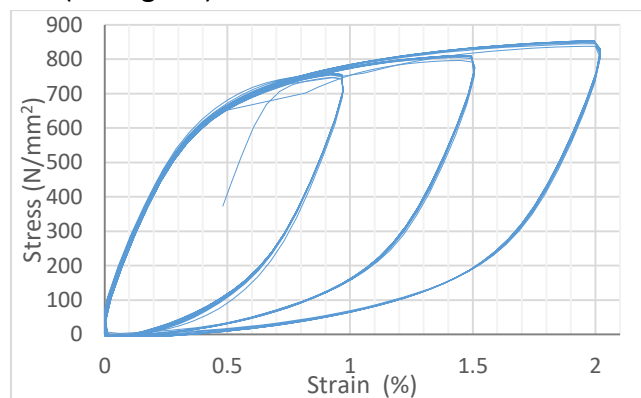


Fig. 79. Relative hysteresis loops from the multiple-step test. Strain amplitudes of $\pm 0.5\%$, $\pm 0.75\%$ and $\pm 1\%$

5.3. Cyclic stress-strain curve

In order to construct the cyclic stress-strain curve (also known as skeleton curve), data pairs (σ, ε) are obtained from half of a stable cycle at each strain amplitude. In this case, the data pairs will be extracted from the last cycle of each amplitude of the Multiple-step method test. In figure 80 these data points (blue points) and the fitted curve following a two-stage model (black) are plotted along with the stress-strain curve obtained from the experimental monotonic tensile test (blue).

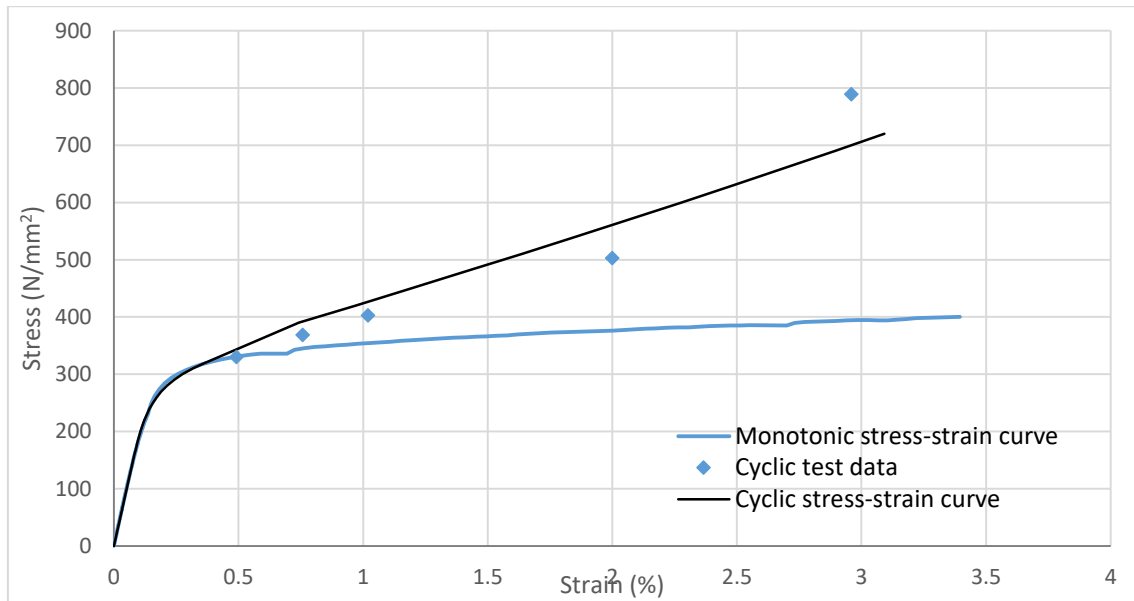


Fig. 80. Comparison of cyclic and monotonic stress-strain curves.

As shown, stainless steel exhibits a considerable level of cyclic hardening, as the strain amplitude increases, the stress rises to values much higher than that of the tensile test.

5.4. Young's modulus and proof stress

The Young's modulus is a material resistance to being deformed elastically when subjected to stress. Basically, it is defined as the ratio of tensile stress to tensile strain of the elastic branch of a material and it can be obtained from a monotonic tensile stress.

In order to calculate Young's modulus, it is important to take into account that initial experimental data sets are usually not representative due to machine-coupon settlement and should not be considered in the calculation.

A Pearson correlation coefficient (r_k) is obtained for groups of 15 experimental points, from point k to point $k+14$. Then a variation between these coefficients is calculated as: $\Delta r_k = (r_k - r_{k-1})/r_{k-1}$. The initial point of the set of representative points is the first one that fulfils the following conditions: $\Delta r_k < 0.5\%$, $r_{k+1} < 0.5\%$, and $\Delta r_{k+2} < 0.5\%$.

It is necessary to ensure that the quantity of points used is sufficient, but also guaranteeing that the points belong to the linear branch of the experimental data, therefore the last point of the set of representative points is the first, after the initial

point, that fulfils the following conditions: N° of points ≥ 15 , $\Delta\sigma = \sigma_j - \sigma_i \geq 60$, $\sigma_j \leq \min(\sigma_u/5 ; 125)$.

Once the set of representative points is defined, Young's modulus is determined by linear regression.

The Young modulus obtained from the stress-strain data of the monotonic tensile test equals to $E = 196119 \text{ N/mm}^2$.

In this research project, the yield strength is defined as 0,2% proof stress ($\sigma_{0.2}$) of the material. In order to obtain this stress, it is necessary to find the stress in which the material has a plastic strain of 0,2% with plastic strain defined as: $\varepsilon_p = \varepsilon - \sigma/E$, where E is the Young's modulus. This can be better represented graphically as the intersection point between the stress-strain curve of the tested material and a line parallel to the Young's modulus that passes through the point with zero stress and 0,2% strain. Figure 81 shows the stress-strain chart along with the Young's modulus slope and the parallel line used to find $\sigma_{0.2}$.

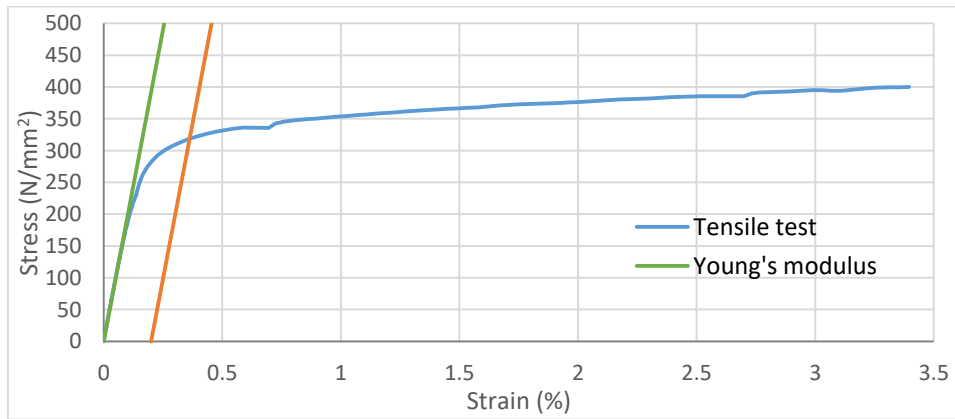


Fig. 81. Graphical representation of the Young's Modulus and proof stress.

The 0,2% proof stress obtained is $\sigma_{0.2} = 319 \text{ N/mm}^2$.

5.5. The Ramberg-Osgood parameters and Mirambell-Real two-stage model

The Ramberg-Osgood and the two-stage model strain hardening coefficients (see section 2.1.5) were obtained (see Eq.(1) and (3)).

$$\varepsilon = \frac{\sigma}{E} + 0.002 \left(\frac{\sigma}{\sigma_{0.2}} \right)^n \quad \text{for } \sigma \leq \sigma_{0.2} \quad (1)$$

$$\varepsilon = 0.002 + \frac{\sigma_{0.2}}{E} + \frac{\sigma - \sigma_{0.2}}{E_y} + \varepsilon_u * \left(\frac{\sigma - \sigma_{0.2}}{\sigma_u - \sigma_{0.2}} \right)^m \quad \text{for } \sigma_{0.2} < \sigma \leq \sigma_u \quad (3)$$

The Young's modulus and the 0,2% proof stress were found in the previous section, the tangent modulus is obtained analogously to Young's modulus and the parameters n and m were calibrated to fit the experimental curve with the minimum error. The error is defined as the sum of the squares of the minimum distances between both functions,

taking into account not only the strain variable, but the stress variable as well (see Eq. (16)) [44].

$$e = \sum_{i \in A} \min_{k \in A} \left\{ \sqrt{\left(\frac{\varepsilon_{exp,k} - \varepsilon_{Eq,i}}{0.01} \right)^2 + \left(\frac{\sigma_k - \sigma_i}{\sigma_1} \right)^2} \right\} \quad (16)$$

Table 17 gathers all the parameters obtained after fitting the experimental curve with the model.

Table 17. Parameters for the two-stage model.

E (MPa)	$E_{0.2}$ (MPa)	$\sigma_{0.2}$ (MPa)	n	m
196119	18072	319	8	2.33

Figure 82 shows the stress-strain curve using the Mirambell-Real two-stage model and in the bottom right, a comparison between the test data and the model is made.

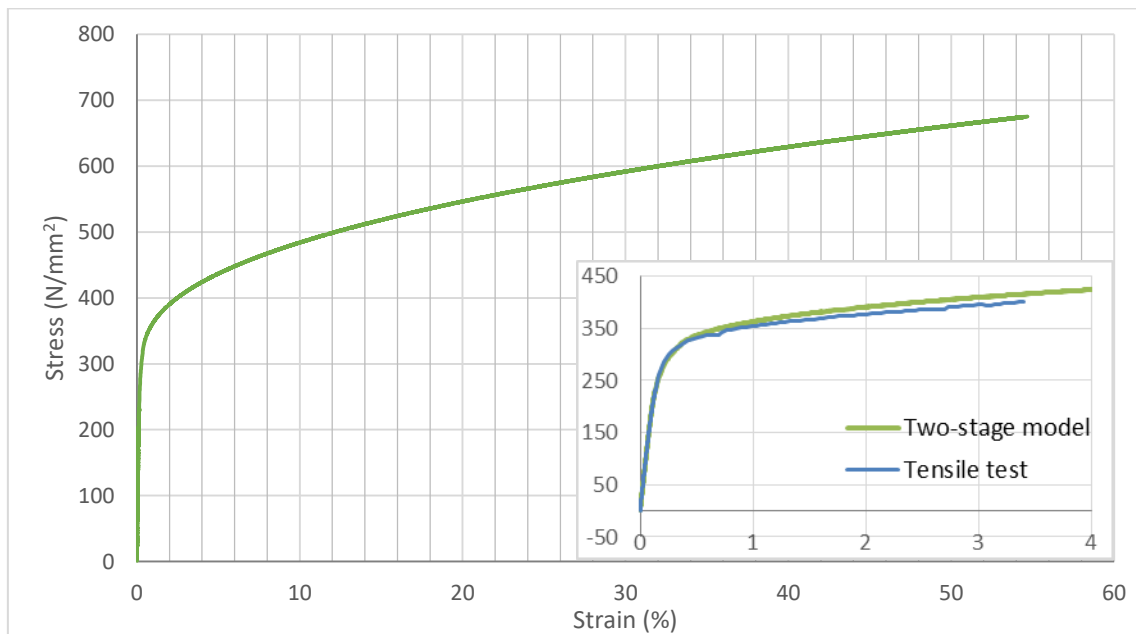


Fig. 82. Stress-strain curve, two-stage model.

5.6. Combined isotropic/kinematic hardening model

As it is mentioned in section 2.1.5, in order to simulate the cyclic behaviour of stainless steel a model that utilizes an isotropic and a kinematic component is needed. In order to understand and analyse the cyclic behaviour of stainless steel and be able to obtain the analytical expressions that define this model, it is necessary to obtain pairs of data points from the hysteresis loops. The procedure to obtain these points is described below.

Isotropic component

The tabular data used in the isotropic component consist of a series of $(\sigma_i^0, \varepsilon_i^p)$ data pairs. The first data points needed are the maximum tensile stress σ_i^t and the maximum compressive stress in the elastic range σ_i^c for each cycle as shown in the figure 7.

In order to obtain the maximum tensile stress in each cycle, first, it is important to note that in the experimental data, the maximum tensile stress of a cycle does not coincide with the maximum plastic strain and the value of the strain corresponding to maximum stress varies in every cycle. Therefore, data pairs of maximum tensile stress and corresponding plastic strain are obtained for every cycle and a mean value of the plastic strains is calculated. Then, values of stresses at that mean plastic strain are calculated at each cycle by linear interpolation. These stresses will be used as maximum tensile stresses σ_i^t .

The maximum compressive stress in the elastic range σ_i^c is calculated similarly to the yield strength, but using the maximum tensile data pairs as the coordinates origin. A plastic strain of 0.2% is considered as the end of the elastic range. For a better understanding, figure 83 shows the graphical method for obtaining σ_i^c .

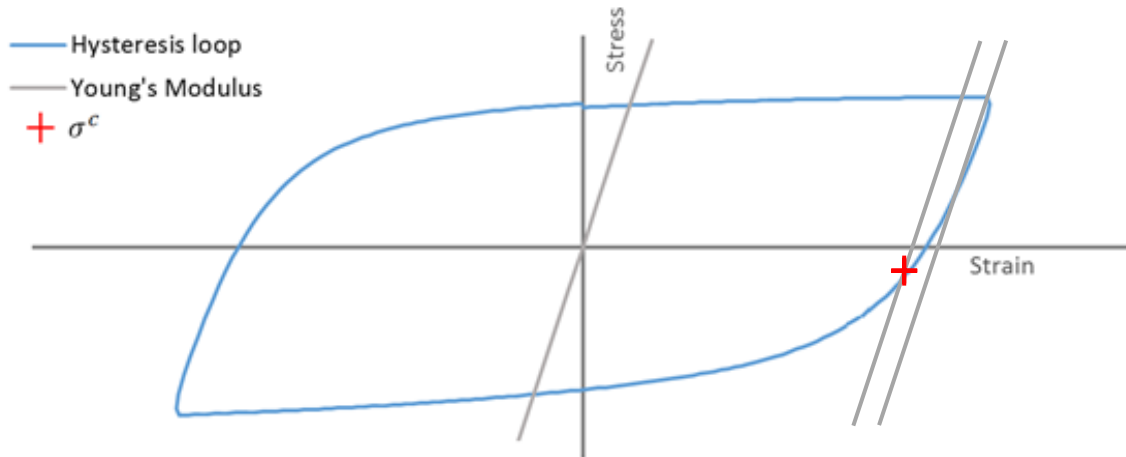


Fig. 83. Example of obtaining the maximum compressive stress in the elastic range.

After σ_i^t and σ_i^c are found, equation (5) is solved and the stresses for the tabular data (σ_i^0) are obtained.

Regarding the strains values for the tabular data (ε_i^p), equations (6) and (7) are used. These values represent the accumulated plastic strain that has occurred until the cycle i .

$$\sigma_i^0 = (\sigma_i^t - \sigma_i^c)/2 \quad (5)$$

$$\varepsilon_i^p = \frac{1}{2}(4i - 3)\Delta\varepsilon^p \quad (6)$$

$$\Delta\varepsilon^p \approx \Delta\varepsilon - 2\sigma_1^t/E \quad (7)$$

Data pairs of $(\sigma_i^0, \varepsilon_i^p)$, were extracted from the constant strain amplitude test at $\pm 3\%$ and $\pm 5\%$ and from the multiple-step method test at strain amplitudes of $\pm 0.5\%$, $\pm 0.75\%$, $\pm 1\%$, $\pm 2\%$ and $\pm 3\%$. The extracted data are plotted (in colours) in figures 84 and 85.

$$\sigma^0 = \sigma|_0 + Q_\infty(1 - e^{-b\varepsilon^p}) \quad (4)$$

Using the exponential formulation described in section 2.1.5 (Eq. (4)), it is possible to obtain analytical parameters that fit the points above. As well as in previous calculations, the curve of the exponential formulation is fitted to the experimental data to obtain the parameter b . The error used to fit the data is analogous to the error used in the two-stage model (see Eq. (15)).

$$e = \sum_{i \in A} \min_{k \in A} \left\{ \sqrt{\left(\frac{\sigma_{exp,k} - \sigma_{Eq,i}}{\sigma|_0} \right)^2 + (\varepsilon_k - \varepsilon_i)^2} \right\} \quad (17)$$

The exponential curves are plotted (in black) along with the experimental data in figures 84 and 85. The parameters are presented in the following table.

Table 18. Parameters for the Isotropic component.

Equation		$\sigma^0 = \sigma _0 + Q_\infty(1 - e^{-b\varepsilon^p})$		
Method	Amplitude	Parameters		
		$\sigma _0$	Q_∞	b
Companion method	$\pm 3\%$	319	327	0.66
	$\pm 5\%$	319	156	3.14
Multiple-step	$\pm 0.5\%$	319	25	198.28
	$\pm 0.75\%$	319	24	269.61
	$\pm 1\%$	319	26	30.85
	$\pm 2\%$	319	82	6.00
	$\pm 3\%$	319	191	3.56

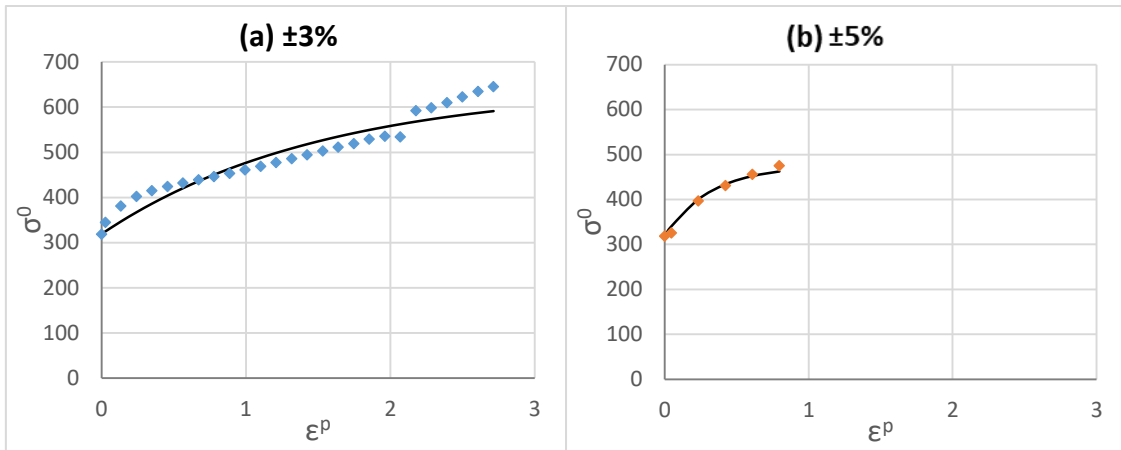


Fig. 84. Input data for Isotropic hardening component obtained from companion method tests at strain amplitudes of $\pm 3\%$ (left) and $\pm 5\%$ (right).

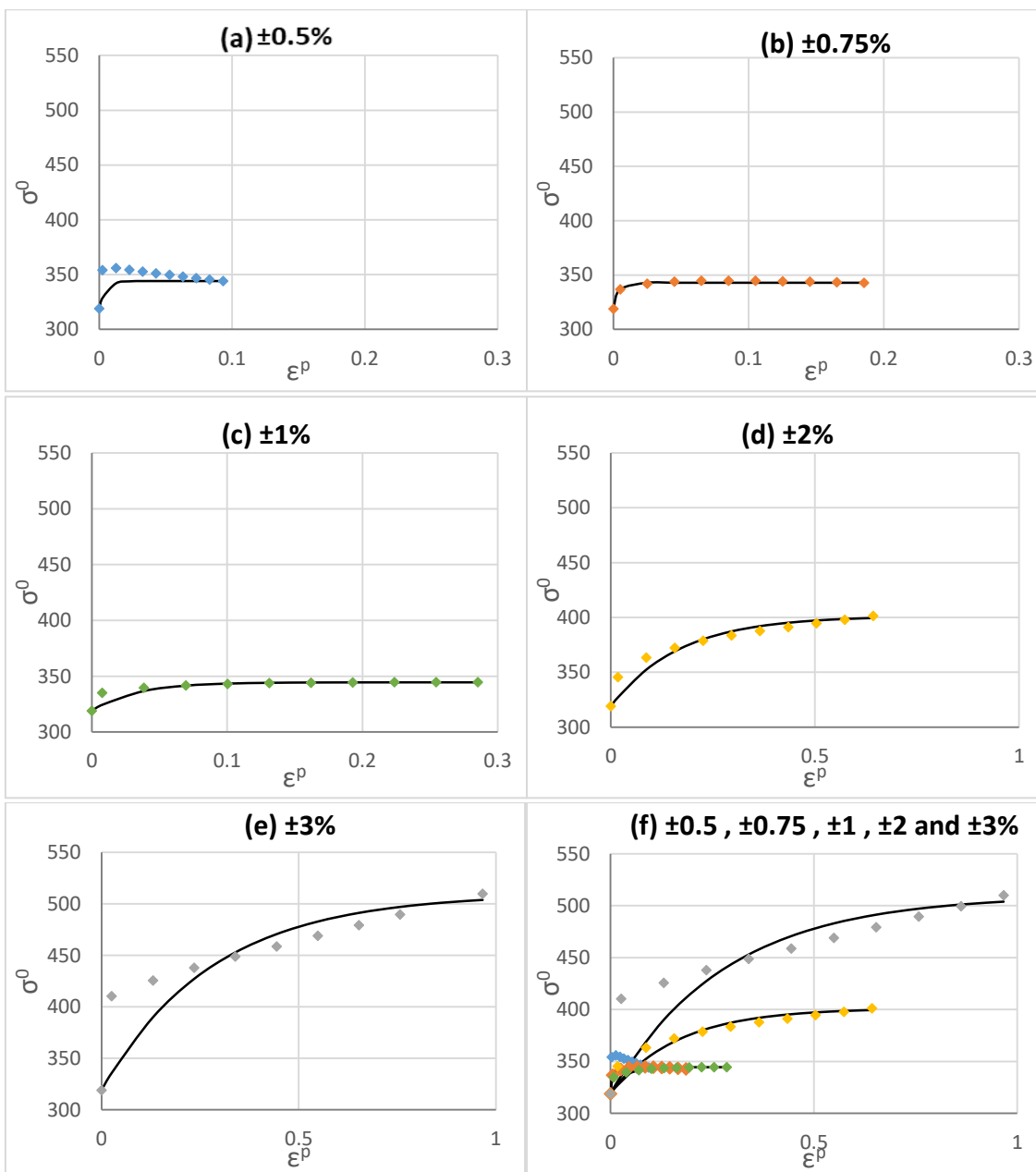


Fig. 85. Input data for Isotropic hardening component obtained from the multiple-step method test.

As it can be seen in the results, the isotropic data shows a cyclic hardening that begins to be noticeable at an amplitude of $\pm 2\%$. At amplitudes of $\pm 0.5\%$, $\pm 0.75\%$ and $\pm 1\%$, in general, hardening appears in the first cycle and practically no changes in stresses develop through the rest of the cycles; this explains the lower values of Q_∞ (low change in the size of the yield surface) and higher values of b (it reaches its maximum value with low plastic strain).

When comparing the parameters between both methods at an amplitude $\pm 3\%$, it can be noticed that the values differ from one another, this is due to the nature of each method. For the multiple-step method, only 10 cycles of data are obtained, this means that the curve could only reach a certain plastic strain and therefore the value of Q_∞ is limited by the stress reached at that last cycle; in the companion method, more plastic strain is developed and the stress reached is higher and the Q_∞ changes.

Despite this discrepancy, it is later shown in the results (section 6.2) that for the first 5 cycles, the numerical models using data for both methods exhibit a behaviour that agrees with the experimental data.

It is worth mentioning that $\sigma|_0$ is defined by Nip et. al. [2] as 0.01% proof stress, however, these values seemed not to fit with the behaviour of the curves. It was later realized that a proof stress of 0.2% (yield strength) fits better the curves and show results that better agrees with the experimental data.

Kinematic component

The tabular data used as input of the kinematic hardening component consist of a series of $(\sigma_i^0, \varepsilon_i^p)$ data pairs. These values of stress and plastic strain are obtained from the stabilized loop as shown in figure 8 and then shifted using Eq. (9). In order to do so, it is necessary to obtain the stress at zero plastic strain (σ_1) of a stabilized loop analogously to the previous case considering a plastic strain of 0.2% as the end of the elastic range (see fig. 86).

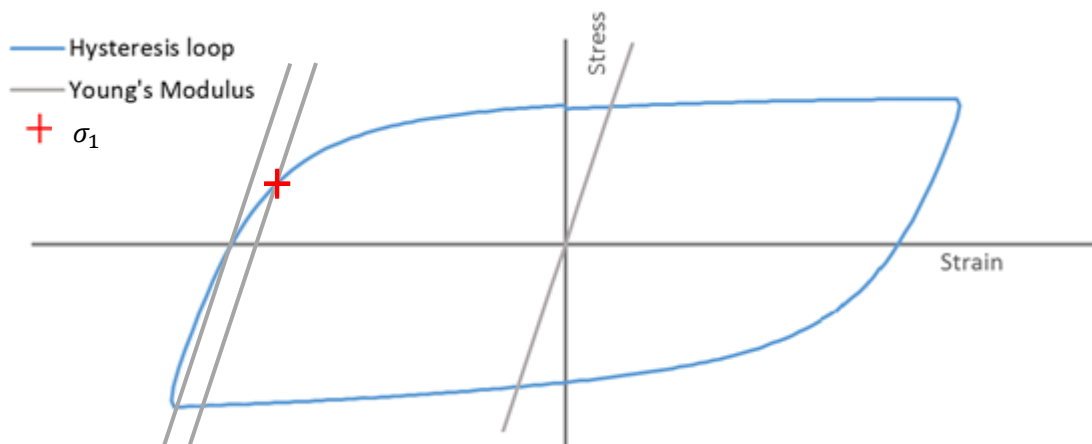


Fig. 86. Example of obtaining the stress at zero plastic strain.

After obtaining σ_1 , the rest of the data points are acquired and then shifted using Eq.(9). Next, the change of backstress α is calculated using Eq.(10). The pairs of data points are plotted (in colours) in figures 87 and 88.

$$\alpha = \frac{C_k}{\gamma_k} (1 - e^{-\gamma \varepsilon^p}) + \alpha_1 e^{-\gamma \varepsilon^p} \quad (8)$$

$$\varepsilon_i^p = \varepsilon_i - \frac{\sigma_i}{E} - \varepsilon_p^0 \quad (9)$$

$$\alpha_i = \sigma_i - \sigma^s \quad (10)$$

For the companion method data, the hysteresis loops considered as stabilized are the tenth loop for $\pm 3\%$ and the last loop for $\pm 5\%$.

An important aspect to highlight is that, although the $\pm 5\%$ amplitude test was considered incomplete, the data was extracted knowing that the results could be conservative as the material could be hardened more.

As well as for the isotropic component, with Eq.(8), it is possible to obtain analytical parameters that describe the curves above. The parameters are obtained by fitting the analytical curve with the experimental curve obtaining the minimum error. The error is defined by the following equation.

$$e = \sum_{i \in A} \min_{k \in A} \left\{ \sqrt{\left(\frac{\alpha_{exp,k} - \alpha_{Eq,i}}{\alpha_1} \right)^2 + \left(\frac{\varepsilon_k - \varepsilon_i}{0.01} \right)^2} \right\} \quad (16)$$

The curves following the parameters obtained by fitting the curves are plotted in black along with the experimental data in figures 87 and 88. The proposed parameters are presented in table 19.

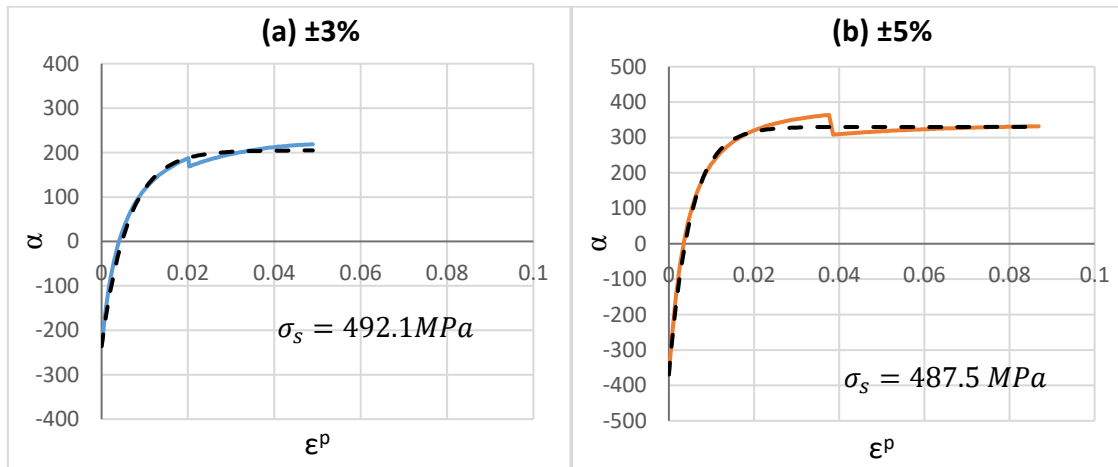


Fig. 87. Input data for kinematic hardening component obtained from companion method tests at strain amplitudes of $\pm 3\%$ (left) and $\pm 5\%$ (right).

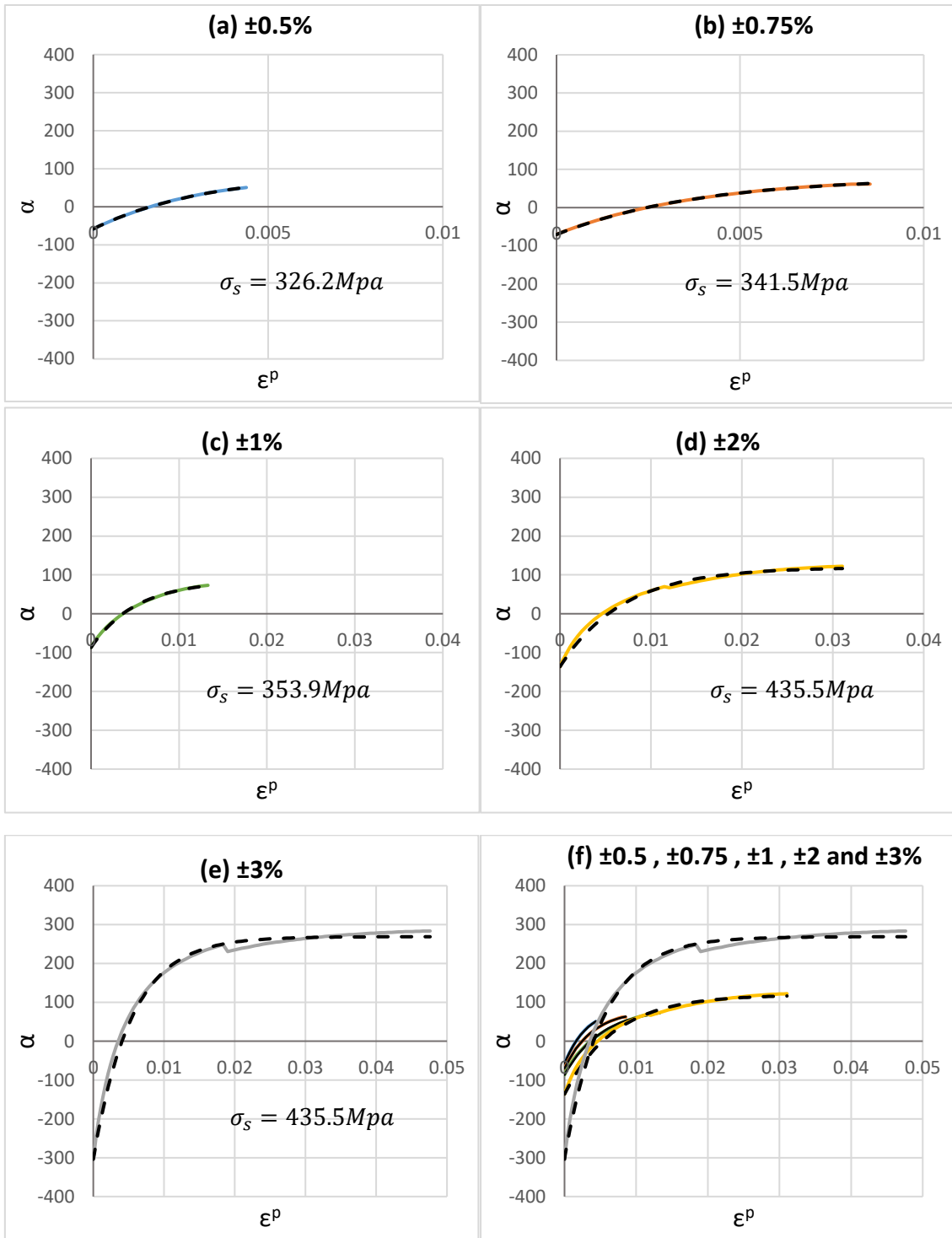


Fig. 88. Input data for kinematic hardening component obtained from the multiple-step method test.

Table 19. Parameters for the kinematic component.

Equation		$\alpha = \frac{C_k}{\gamma_k} (1 - e^{-\gamma \varepsilon^p}) + \alpha_1 e^{-\gamma \varepsilon^p}$	
Method	Amplitude	Parameters	
		C_k	γ_k
Companion method	±3%	33396	162.96
	±5%	67381	206.08
Multiple-step	±0.5%	27736	312.57
	±0.75%	20649	258.73
	±1%	16500	193.28
	±2%	17148	143.84
	±3%	50006	186.04

As it can be seen, the analytical curves fit the experimental curves almost perfectly.

With all the data obtained above in figures 84, 85, 87 and 88 and in tables 18 and 19, it is possible to establish the analytical model and perform numerical simulations.

6. NUMERICAL TEST SIMULATION

In this chapter, a brief explanation of the material input in Abaqus is presented, followed by a sensitivity analysis and formerly, the numerical simulations in contrast with the experimental data are shown. Subsequently, analytical parameters are proposed and compared with previous studies. Finally, the results are discussed and exhibited in the last section of the chapter.

6.1. Material properties

In this section, a brief explanation about the material input used in Abaqus is presented.

The density and the elastic properties are common for all the analyses. In table 20, the values used are exhibited.

Table 20. Common material properties.

Density	7.9×10^{-9}
Young's Modulus	196119
Poisson's Ratio	0.3

In order to define the plastic properties using the combined isotropic/kinematic model, the software Abaqus allows the input of this model in two ways: by defining the analytical parameters or by introducing tabular data points obtained from tests. For a better understanding of this see figure 89.

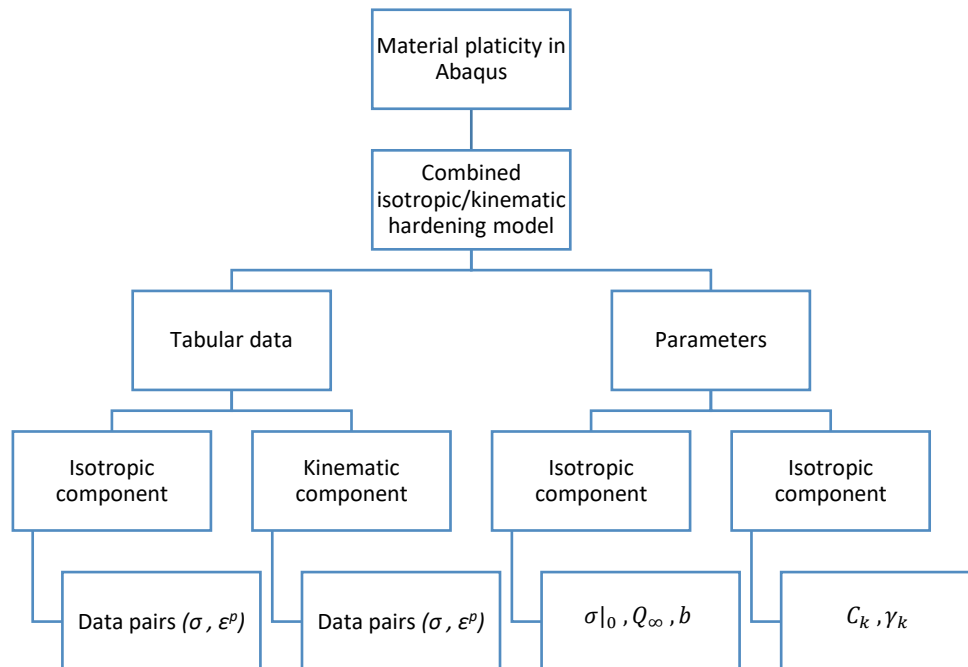


Fig. 89. Plasticity input flow chart

Tabular Data

In order to define the tabular data, two steps are needed.

First, the **kinematic component** is introduced. The data points used in this component are the experimental values exhibited in figures 87 and 88 but instead of using the values of change of backstress (α), the stresses from which they are calculated is introduced (see Eq. (10)).

$$\alpha_i = \sigma_i - \sigma^S \quad (10)$$

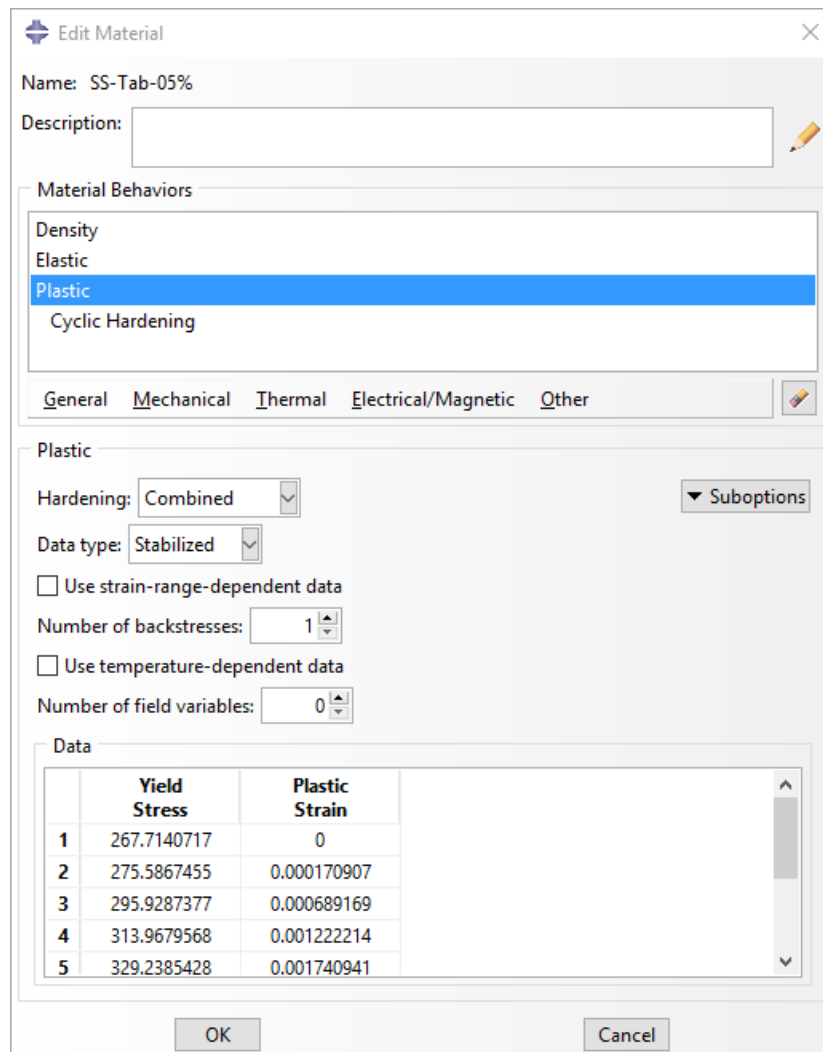
The data is introduced following the procedure below.

For AbaqusCAE (see fig. 90):

Property module: material editor: Mechanical→Plasticity→ Plastic: Hardening: Combined, Data type: Stabilized, Number of backstresses: n

For Input file:

*PLASTIC, HARDENING=COMBINED, DATA TYPE=STABILIZED, NUMBER BACKSTRESSES=n



The screenshot shows the 'Edit Material' dialog box in AbaqusCAE. The 'Name' is 'SS-Tab-05%'. Under 'Material Behaviors', 'Plastic' is selected. The 'Plastic' sub-dialog shows 'Hardening' set to 'Combined', 'Data type' set to 'Stabilized', 'Number of backstresses' set to 1, and 'Number of field variables' set to 0. A table of data is displayed at the bottom:

	Yield Stress	Plastic Strain
1	267.7140717	0
2	275.5867455	0.000170907
3	295.9287377	0.000689169
4	313.9679568	0.001222214
5	329.2385428	0.001740941

Fig. 90. Example of kinematic component material input as tabular data.

Second, the **isotropic component** is defined. In this case the data points used in this component are the experimental values exhibited in figures 84 and 85.

The data is introduced following the procedure below.

For AbaqusCAE (see fig. 91):

Property module: material editor: Mechanical→Plasticity→Plastic: Hardening: Combined: Suboptions→Cyclic Hardening

For Input file:

*CYCLIC HARDENING

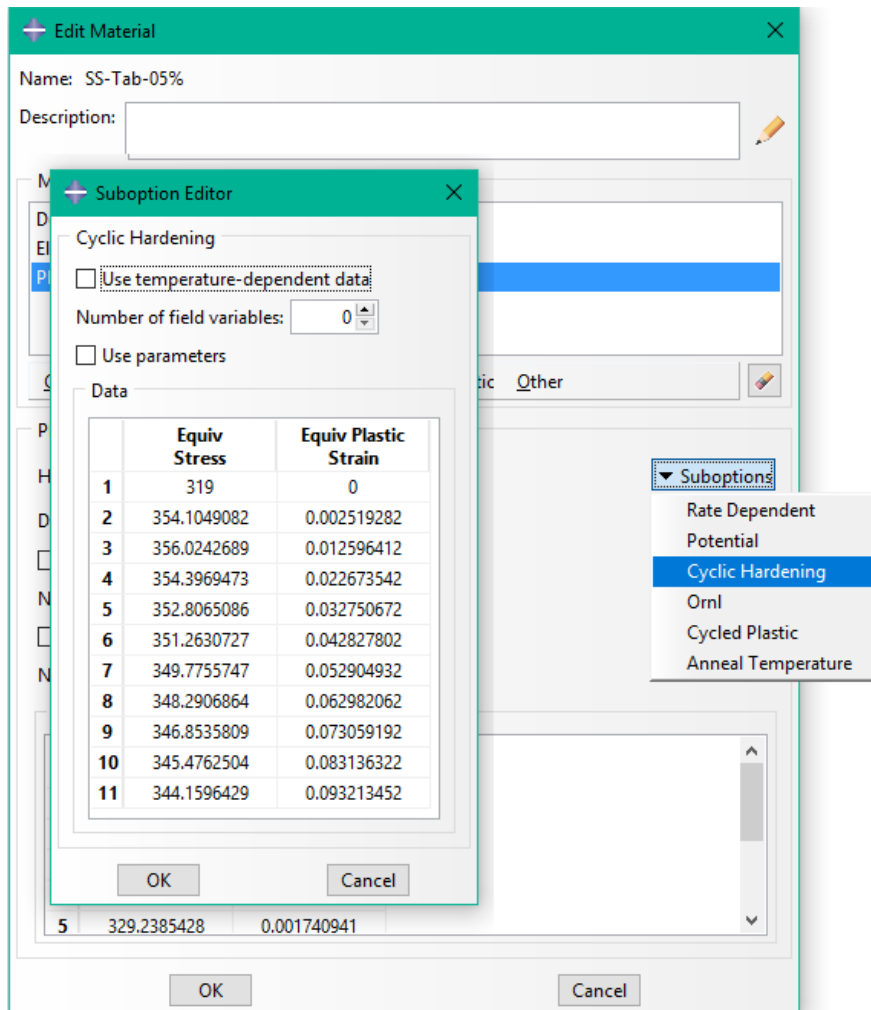


Fig. 91. Example of isotropic component material input as tabular data.

Parameters

As mentioned before, another option for introducing the analytical modes is by defining parameters.

In order to define a combined hardening using parameters, similar steps are needed.

First, the **kinematic component** is defined. The parameters used for the model are exhibited in table 19.

For AbaqusCAE (see fig. 92):

Property module: material editor: Mechanical Plasticity Plastic: Hardening: Combined,
Data type: Parameters, Number of backstresses: n

For Input file:

*PLASTIC, HARDENING=COMBINED, DATA TYPE=PARAMETERS, NUMBER
BACKSTRESSES=n

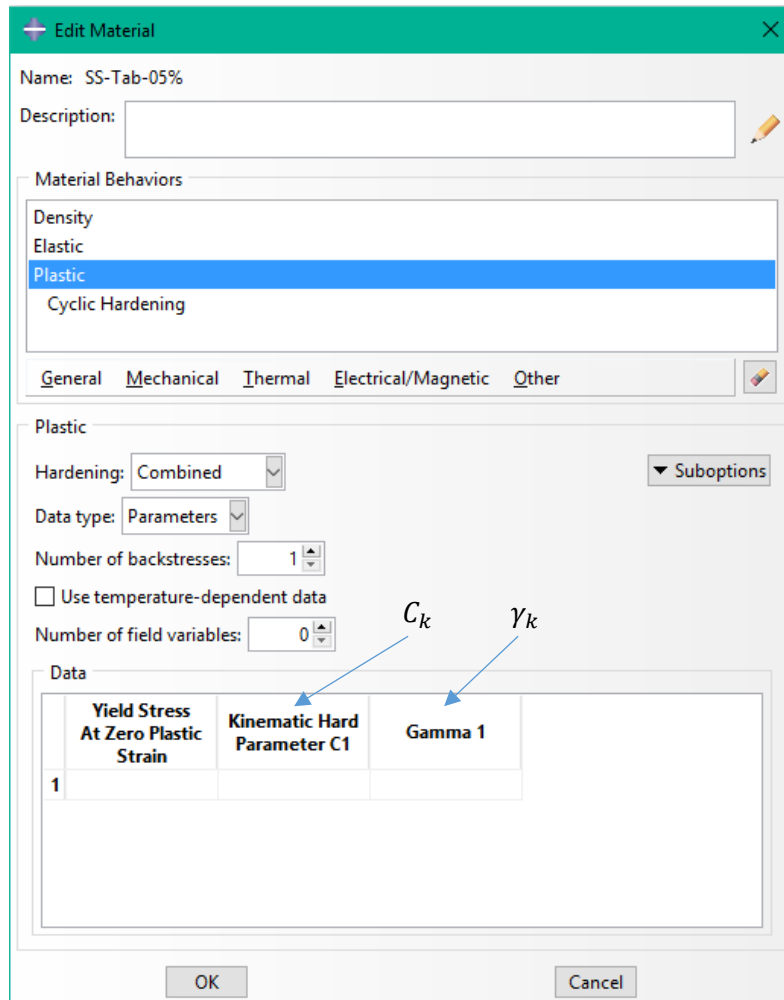


Fig. 92. Example of kinematic component material input using parameters.

Second, the **isotropic component** is defined. The parameters used for the model are exhibited in table 18.

For AbaqusCAE (see fig.93):

Property module: material editor: Mechanical→Plasticity→Plastic: Suboptions→Cyclic
Hardening: toggle on Use parameters.

For Input file:

*CYCLIC HARDENING, PARAMETERS

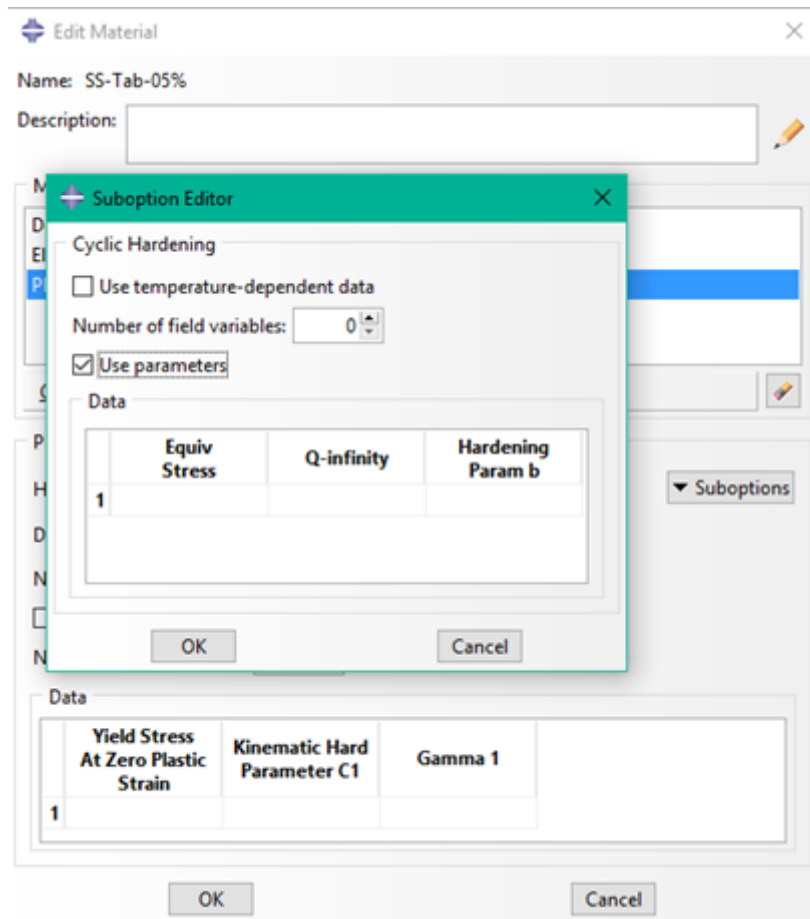


Fig. 93 Example of isotropic component material input using parameters.

It is worth mentioning that, when defining the combined hardening model in Abaqus using experimental tabular data, the software automatically provides the kinematic parameters C_k and γ_k by fitting the curve. In table 21, the kinematic parameters obtained in this study are compared with the ones provided by Abaqus.

Table 21. Comparison between kinematic hardening parameters.

Equation		$\alpha = \frac{C_k}{\gamma_k} (1 - e^{-\gamma \epsilon^p}) + \alpha_1 e^{-\gamma \epsilon^p}$			
Method	Amplitude	Parameters			
		Abaqus		Fitted curve	
		C_k	γ_k	C_k	γ_k
Companion method	±3%	36697	173.78	33396	162.96
	±5%	71712	206.00	67381	206.08
Multiple-step	±0.5%	28966	312.57	27736	312.57
	±0.75%	21799	258.73	20649	258.73
	±1%	17817	193.28	16500	193.28
	±2%	19150	155.80	17148	143.84
	±3%	55096	199.45	50006	186.04

As it can be seen, the parameters are very similar.

6.2. Sensitivity analysis

In this section, parameters that define the cyclic plasticity of the material in Abaqus, are studied and compared. In order to do so, different models were executed with different plastic material characteristics.

The first set of models will be comparing the influence of the parameter b from the isotropic component of the Chaboche model at different displacement amplitudes. In order to do so, the parameters of the kinematic component along with Q_∞ , are kept constant (see Eq. (4)).

$$\sigma^0 = \sigma|_0 + Q_\infty(1 - e^{-b\varepsilon^p}) \quad (4)$$

The second set of models will be comparing the influence of the parameters C_k and γ_k from the kinematic component of the model (see Eq. (8)), to do so, the parameters of the isotropic component are kept constant.

$$\alpha = \frac{C_k}{\gamma_k}(1 - e^{-\gamma\varepsilon^p}) + \alpha_1 e^{-\gamma\varepsilon^p} \quad (8)$$

For these analyses, the external action consists of a displacement applied at the end of the coupon (with the opposite end fixed) following three different periodic functions given in figure 94.

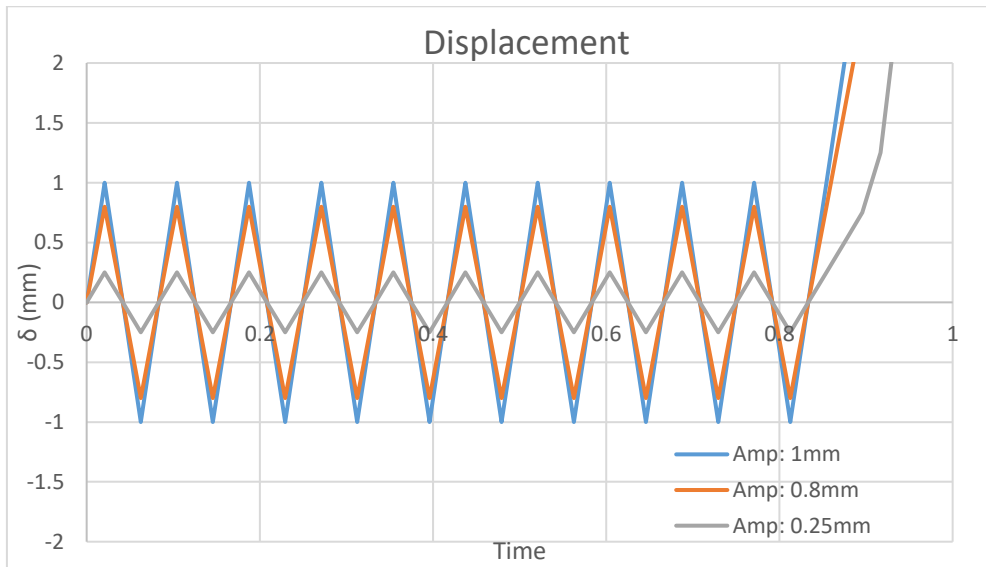


Fig. 94. Displacement functions.

To make the comparisons, stress history and stress-strain charts are employed since they adequately represent the mechanical behaviour of the material.

Isotropic component parameter b

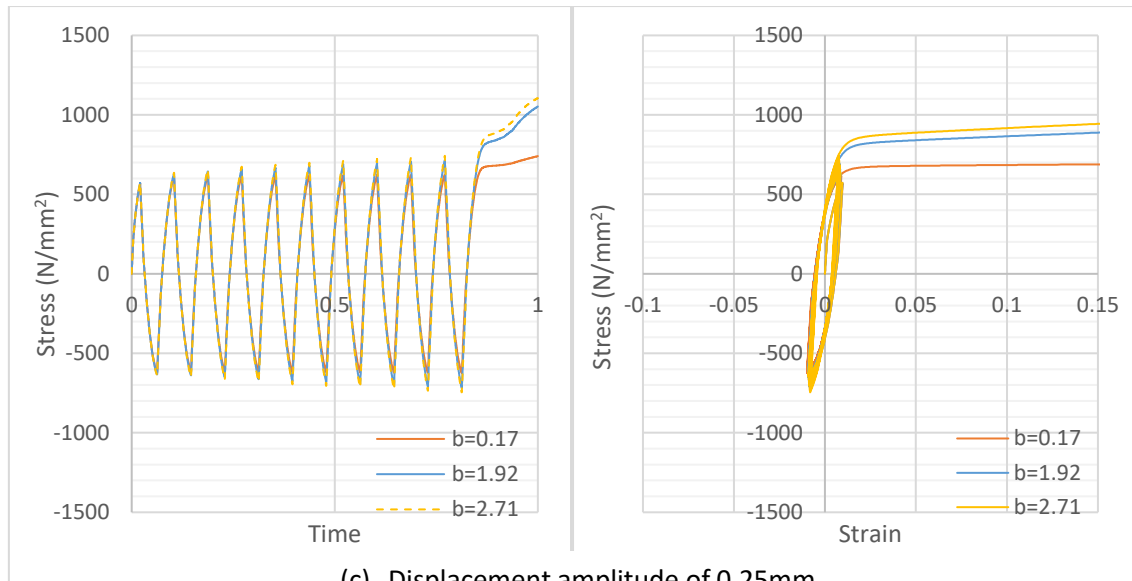
As it is mentioned in section 2.1.5, the parameter b (see Eq. (4)) defines the rate at which the size of the yield surface changes as plastic straining develops. This means that the larger b is, the less plastic strain is needed in order to reach stabilization at a maximum

yield surface. To understand this behaviour several analyses were made using the parameters in table 22 at the mentioned displacement amplitudes.

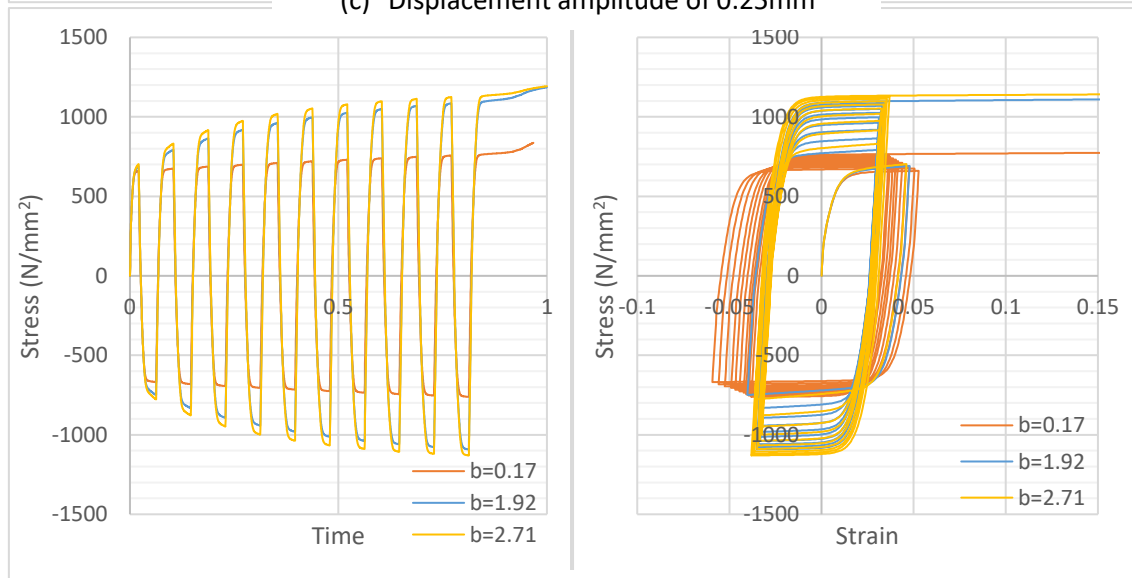
Table 22. Parameters for comparison of "b".

		Isotropic component parameters		Kinematic component parameters	
$\sigma _0$ (N/mm ²)	Q_∞ (N/mm ²)	b		C_k (N/mm ²)	γ_k
210	500	0.17		110000	250
		1.92			
		2.71			

As it can be seen in the results shown in figure 95, the parameter b influences the stabilization; the curves with higher b shows great increment of stress in the first cycles.



(c) Displacement amplitude of 0.25mm



(d) Displacement amplitude of 0.8mm

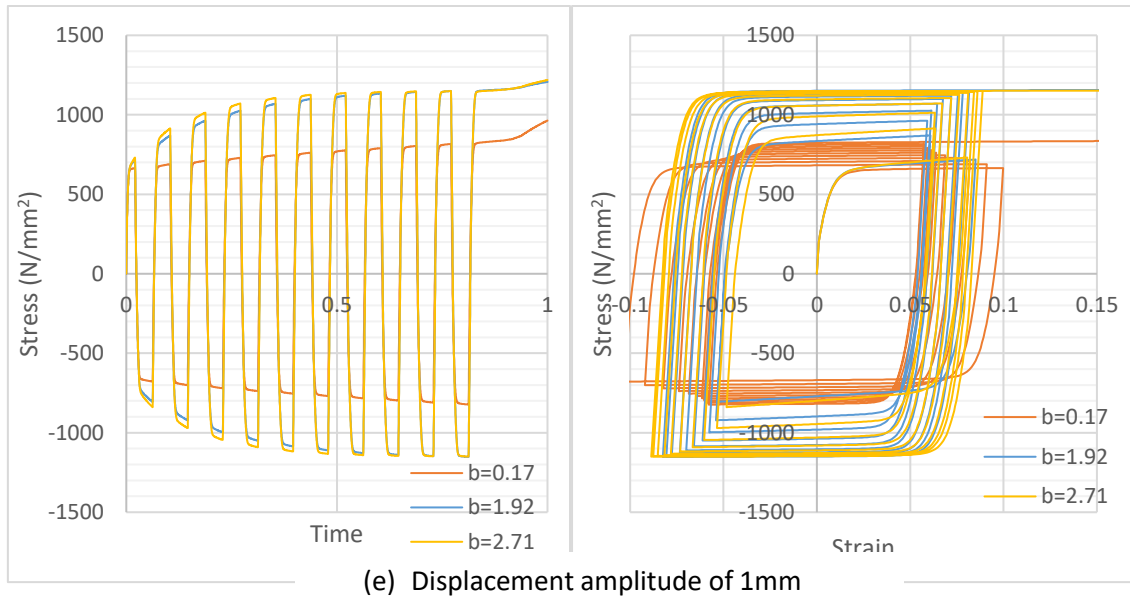


Fig. 95. Stress-time and stress-strain charts for comparison of hardening parameter “b”.

Kinematic component parameters C_k and γ_k

C_k is the initial kinematic hardening modulus and γ_k determine the rate at which the kinematic hardening moduli decrease with increasing plastic deformation. This means that a higher C_k translates to higher stresses at lower plastic strain; and a higher γ_k means a sharper reduction of stress over plastic strain and lower stresses at higher plastic strain. As well as in the previous section, several analyses were made to understand this behaviour using the parameters in table 23.

Table 23. Parameters for comparison of “ C_k ” and “ γ_k ”.

$\sigma _0$ (N/mm ²)	Isotropic component parameters		Kinematic component parameters	
	Q_∞ (N/mm ²)	b	C_k (N/mm ²)	γ_k
210	500	0.17	110000	250
			110000	125
			55000	250

As shown in the results in figure 96, reducing the parameter γ_k by half (orange curve) results in double stresses; in the stress-strain chart, the orange and blue curves have the same initial slope, but it can be seen that before reaching the strain amplitude, the blue curve is closer to an horizontal line than the orange curve. Reducing the parameter C_k by half (green curve) reduces the initial slope and, with the same γ_k , the stresses reached are less than those of the blue curve.

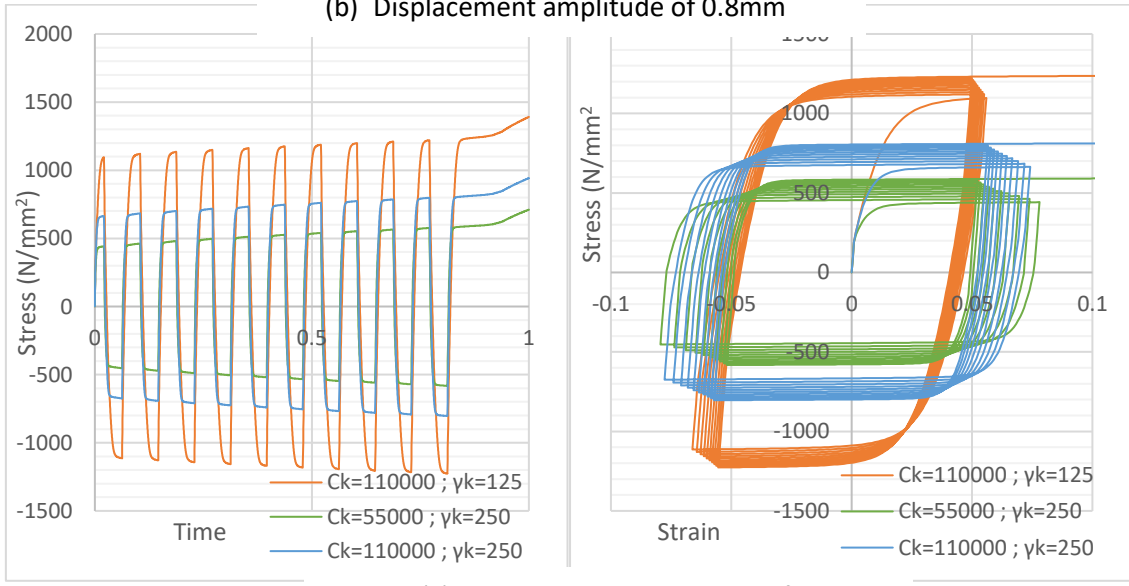
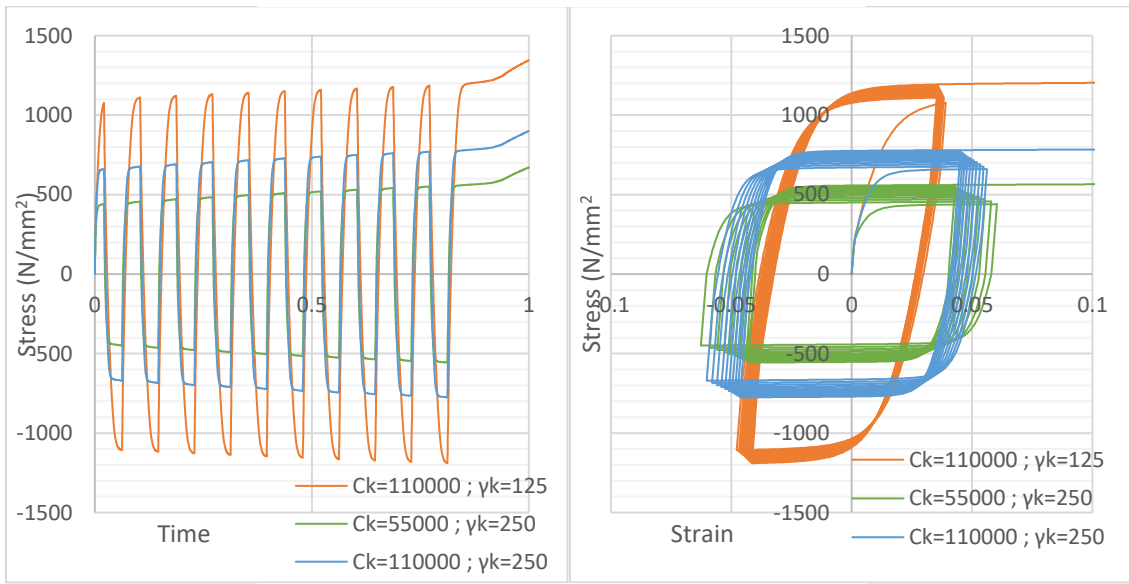
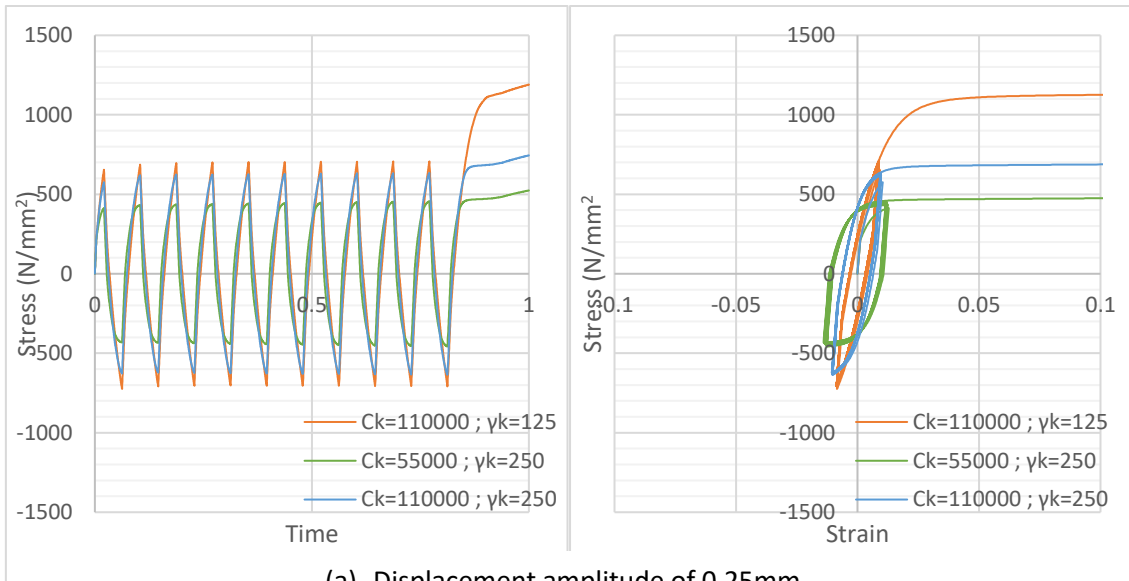


Fig. 96. Stress-time and stress-strain charts for comparison of hardening parameters "Ck" and "γk".

6.3. Correlation between FE models and experimental tests

Once the material input is set, a displacement is applied aiming to obtain a specific strain and the numerical simulations of all the coupons tested were performed in Abaqus. The numerical simulations were performed using both tabular data and parameters as material input of the combined hardening model as explained in section 6.1.

First, the numerical simulations using tabular data will be compared with their experimental counterparts using stress-strain charts and formerly, providing a table with ratios between the peak stresses (σ_{FE}/σ_{exp}) of experimental and simulated curves.

The shape of the curves and the tension peak stresses will be taking into account to observe the similarities between the FE simulation and the experiment.

Strain amplitude of $\pm 5\%$

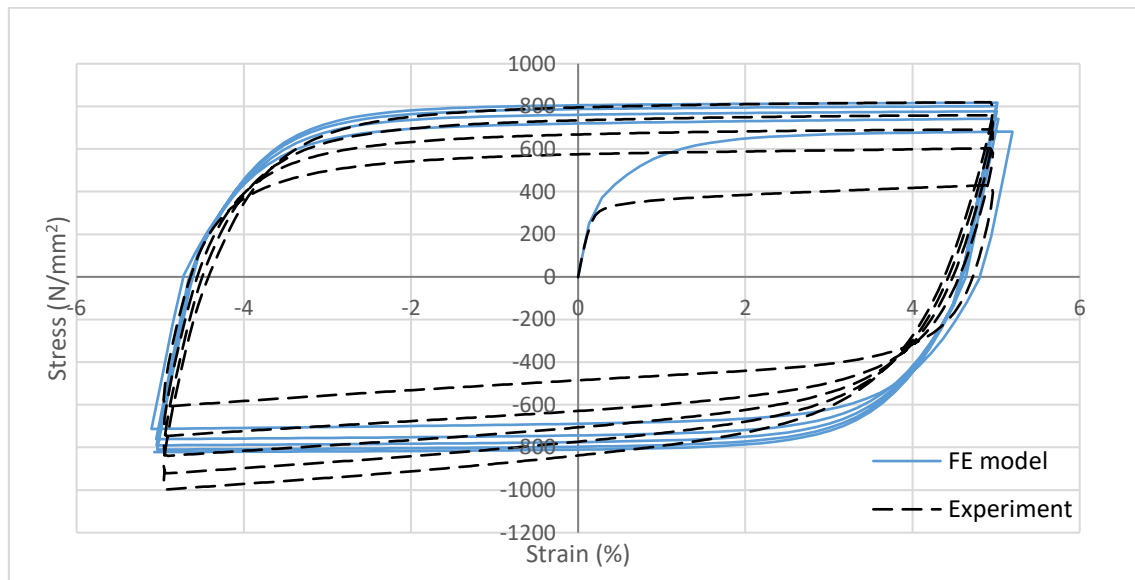


Fig. 97. Experimental and FE simulated stress-strain hysteresis curves in the first 5 cycles of $\pm 5\%$ strain amplitude test (companion method).

Table 24. Ratio between simulated and experimental peak stresses for the first 5 cycles of $\pm 5\%$ strain amplitude (companion method).

Cycle	FE model peak stress (N/mm ²)	Experiment peak stress (N/mm ²)	σ_{FE}/σ_{exp}
1	681.8	430.1	1.585
2	742.0	602.9	1.231
3	776.8	691.3	1.124
4	801.0	758.2	1.056
5	817.3	819.1	0.998

As it can be seen in figure 97 and table 24, the degree of roundedness agrees with the experimental behaviour, however the peak stresses at the first cycles does not completely agree with the experiment.

Strain amplitude of ±3%

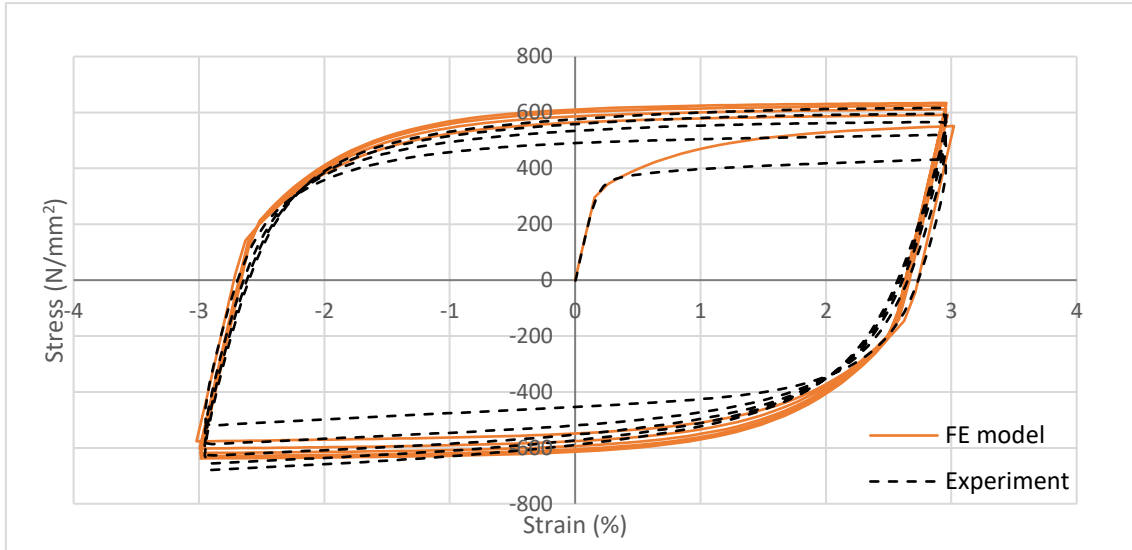


Fig. 98. Experimental and FE simulated stress-strain hysteresis curves in the first 5 cycles of ±3% strain amplitude test (companion method).

Table 25. Ratio between simulated and experimental peak stresses for the first 5 cycles of ±3% strain amplitude (companion method).

Cycle	FE model peak stress (N/mm ²)	Experiment peak stress (N/mm ²)	σ_{FE}/σ_{exp}
1	551.2	431.8	1.277
2	591.3	519.4	1.138
3	611.3	565.5	1.081
4	624.3	594.5	1.050
5	633.9	615.8	1.029

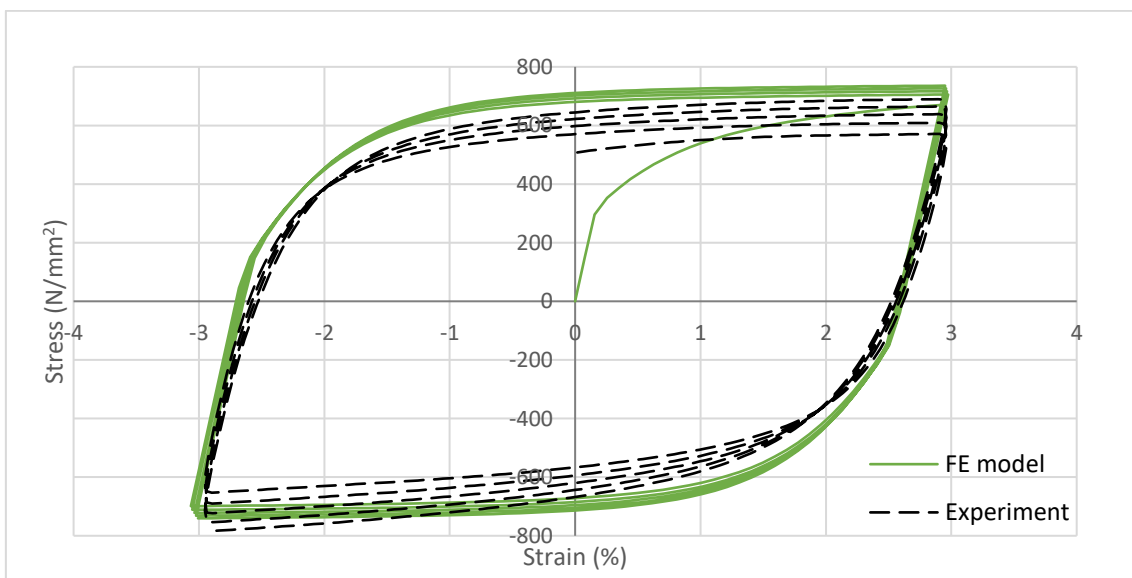


Fig. 99. Experimental and FE simulated stress-strain hysteresis curves in the first 5 cycles of ±3% strain amplitude test (multiple-step method).

Table 26. Ratio between simulated and experimental peak stresses for the first 5 cycles of $\pm 3\%$ strain amplitude (multiple-step method).

Cycle	FE model peak stress (N/mm ²)	Experiment peak stress (N/mm ²)	σ_{FE}/σ_{exp}
1	670.8	571.0	1.175
2	705.6	609.3	1.158
3	716.9	638.5	1.123
4	726.7	664.6	1.093
5	735.9	689.6	1.067

In figure 98 and table 25, a great agreement with the shape and peak stresses is shown, however the first cycles slightly differ from the experimental data. On the other hand, the simulation involving multiple-step method shows more differences with the experiment than the simulation involving companion method.

Strain amplitude of $\pm 2\%$

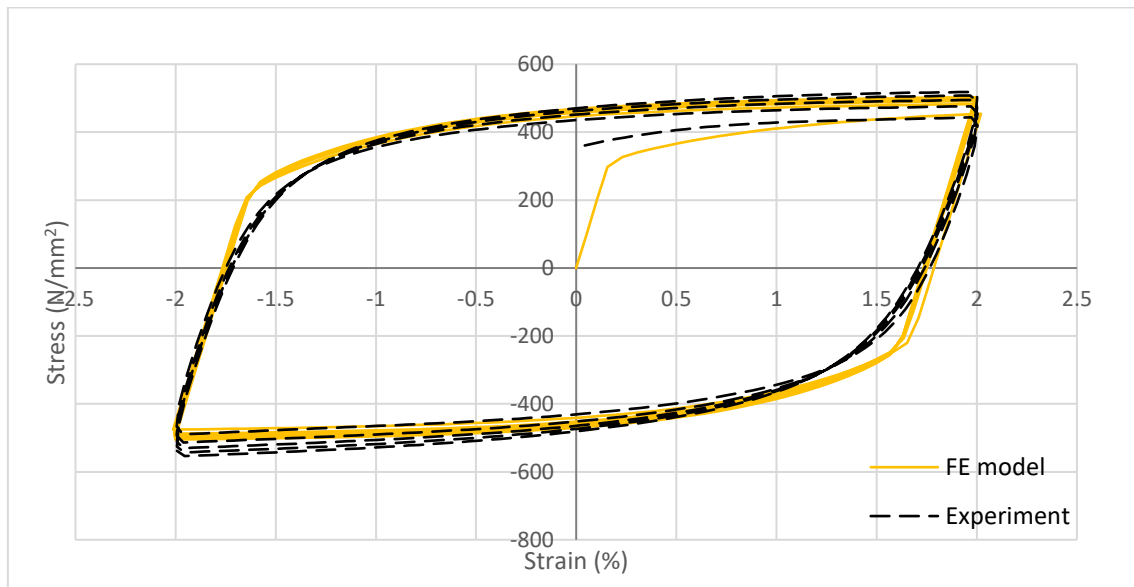


Fig. 100. Experimental and FE simulated stress-strain hysteresis curves in the first 5 cycles of $\pm 2\%$ strain amplitude test (multiple-step method).

Table 27. Ratio between simulated and experimental peak stresses for the first 5 cycles of $\pm 2\%$ strain amplitude (multiple-step method).

Cycle	FE model peak stress (N/mm ²)	Experiment peak stress (N/mm ²)	σ_{FE}/σ_{exp}
1	454.4	443.3	1.025
2	482.7	476.2	1.014
3	491.7	494.5	0.994
4	498.0	507.9	0.980
5	502.8	518.2	0.970

Table 27, show that the peak stresses are practically identical and figure 100 also shows good agreement between simulated and experimental tests.

Strain amplitude of $\pm 1\%$

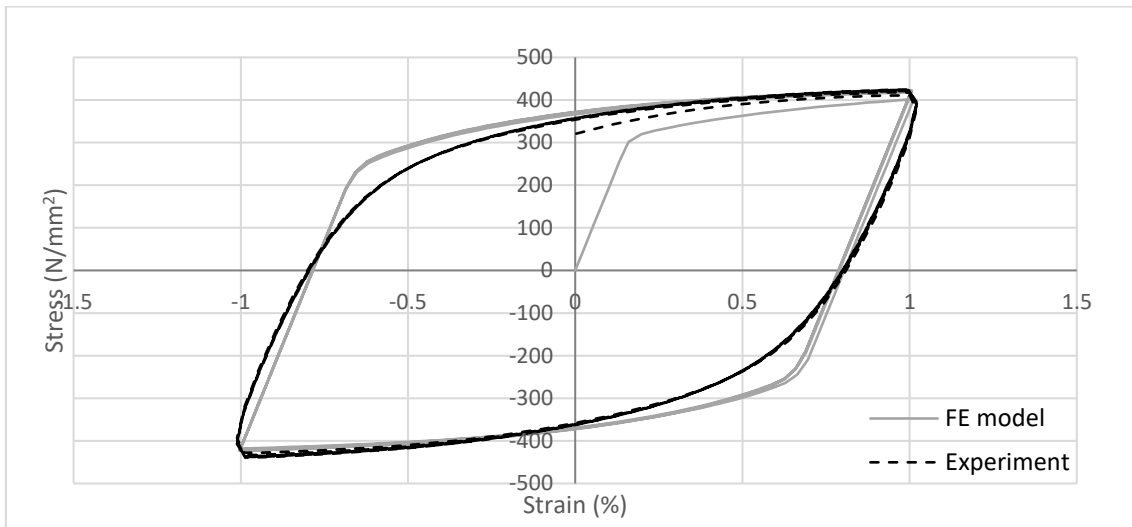


Fig. 101. Experimental and FE simulated stress-strain hysteresis curves in the first 5 cycles of $\pm 1\%$ strain amplitude test (multiple-step method).

Table 28. Ratio between simulated and experimental peak stresses for the first 5 cycles of $\pm 1\%$ strain amplitude (multiple-step method).

Cycle	FE model peak stress (N/mm ²)	Experiment peak stress (N/mm ²)	σ_{FE}/σ_{exp}
1	401.5	410.8	0.977
2	418.4	417.7	1.002
3	420.7	421.0	0.999
4	422.0	423.2	0.997
5	422.8	424.7	0.995

As it is shown in figure 101 and table 28, the similarity between the simulated model and the experimental behaviour is fairly high.

Strain amplitude of $\pm 0.75\%$

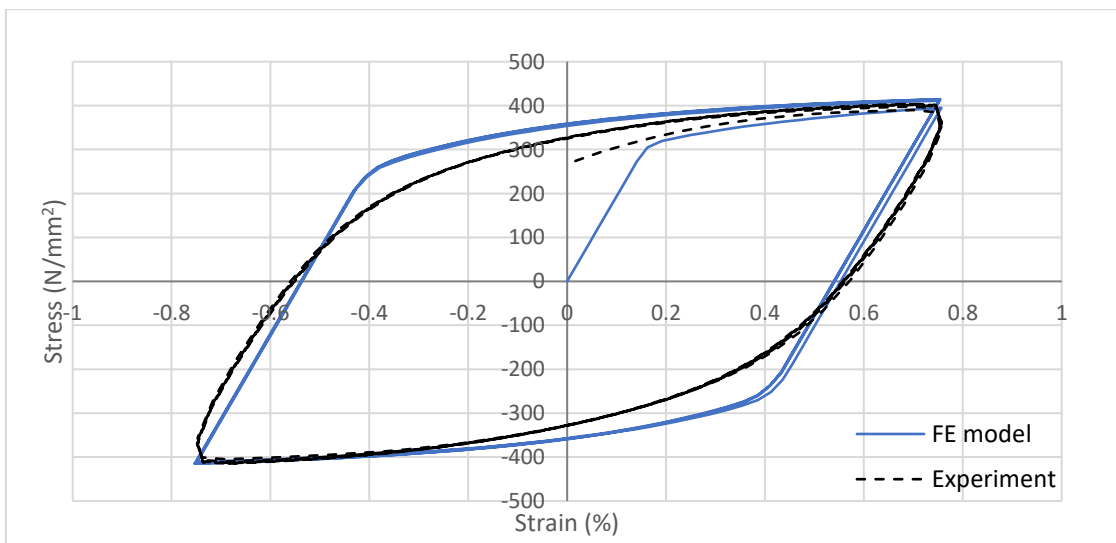


Fig. 102. Experimental and FE simulated stress-strain hysteresis curves in the first 5 cycles of $\pm 0.75\%$ strain amplitude test (multiple-step method).

Table 29. Ratio between simulated and experimental peak stresses for the first 5 cycles of $\pm 0.75\%$ strain amplitude (multiple-step method).

Cycle	FE model peak stress (N/mm ²)	Experiment peak stress (N/mm ²)	σ_{FE}/σ_{exp}
1	394.9	389.6	1.014
2	411.2	398.2	1.033
3	413.4	401.6	1.029
4	414.2	403.3	1.027
5	414.5	404.1	1.026

Figure 102 and table 29 shows results similar to the previous case.

Strain amplitude of $\pm 0.5\%$

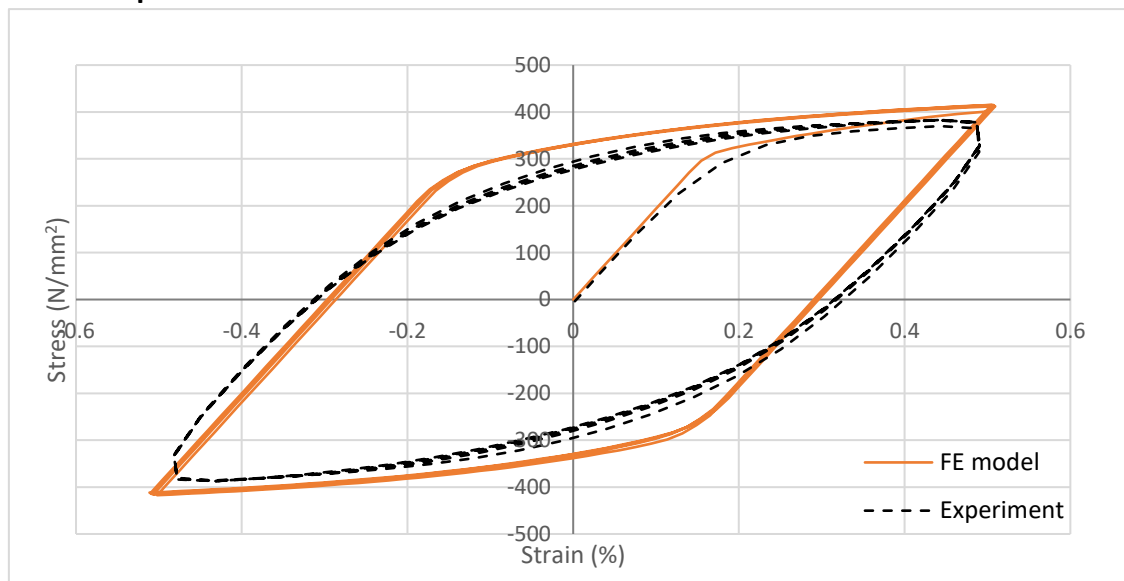


Fig. 103. Experimental and FE simulated stress-strain hysteresis curves in the first 5 cycles of $\pm 0.5\%$ strain amplitude test (multiple-step method).

Table 30. Ratio between simulated and experimental peak stresses for the first 5 cycles of $\pm 0.75\%$ strain amplitude (multiple-step method).

Cycle	FE model peak stress (N/mm ²)	Experiment peak stress (N/mm ²)	σ_{FE}/σ_{exp}
1	401.3	369.9	1.085
2	415.1	382.3	1.086
3	414.8	383.2	1.082
4	413.6	383.1	1.080
5	412.3	382.5	1.078

In figure 103 and table 30 it can be seen, although the simulation describes the general behaviour, its agreement with the experiment is not as good as in previous cases.

After determining that the FE models agree with the experimental tests, the same analyses were executed, this time using the parameters exhibited in tables 18 and 19. The results are exhibited in figures 104 and 105.

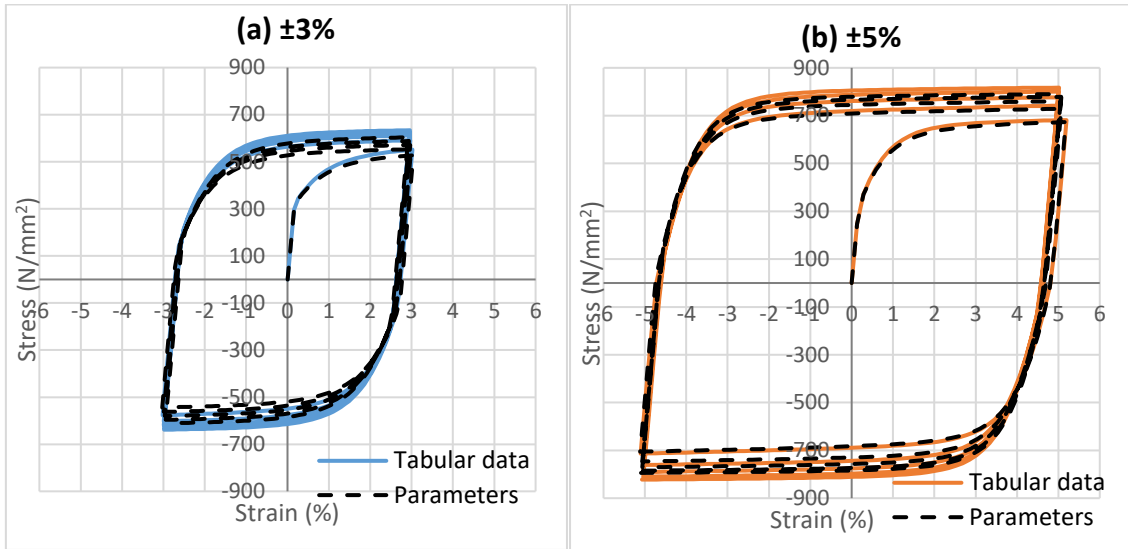
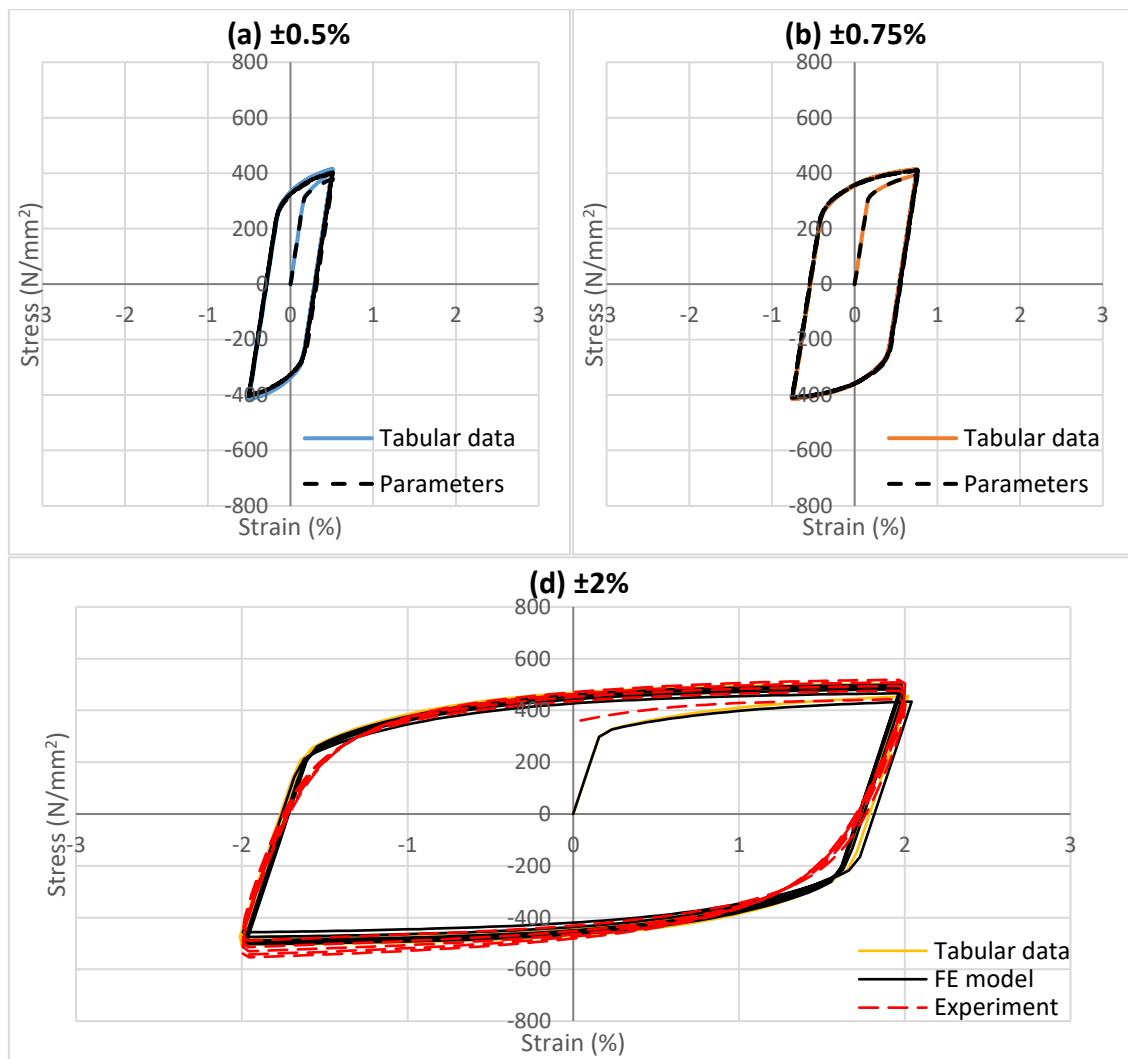


Fig. 104. FE simulated stress-strain hysteresis curves using tabular data and parameters. Data obtained from companion method tests.



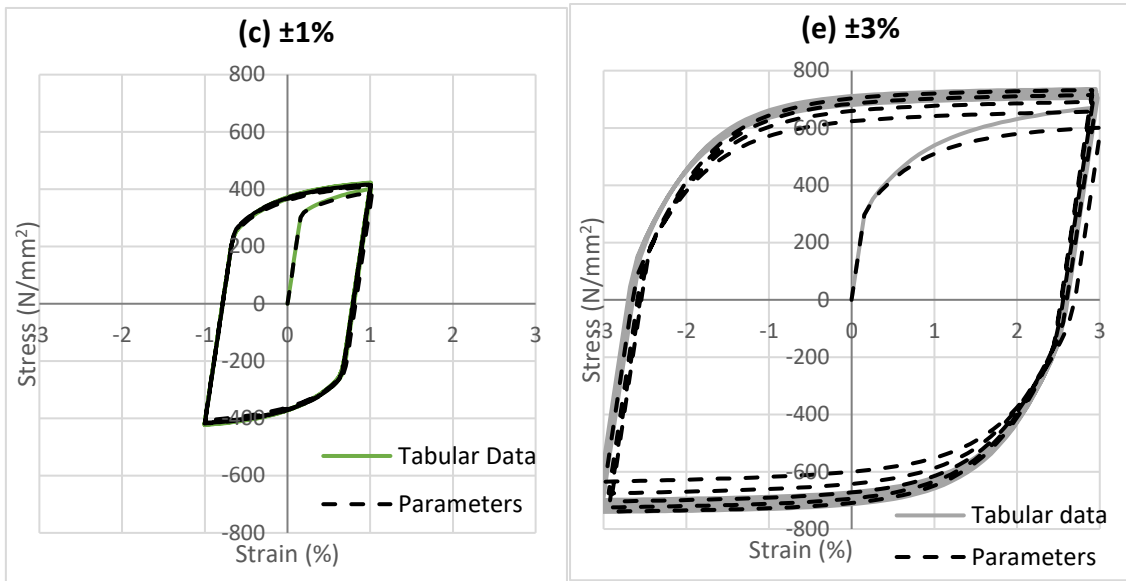


Fig. 105. FE simulated stress-strain hysteresis curves using tabular data and parameters. Data obtained from multiple-step method tests. Additionally Fig. 105 (d) shows the experimental curve.

As shown in figures 104 and 105, The hysteresis loops obtained from a material input using tabular data and parameters are practically identical. This way the parameters are validated and in table 31, the parameters proposed for further research are shown.

Table 31. Proposed parameter values.

Steel Grade	Young's Modulus (N/mm ²)	Yield Strength (N/mm ²)	Amplitude (%)	Combined hardening parameters				
				$\sigma _0$ (N/mm ²)	Q_∞ (N/mm ²)	b	C_k (N/mm ²)	γ_k
EN 1.4301	196119	319	±0.5%	319	25	198.28	27736	312.57
			±0.75%	319	24	269.61	20649	258.73
			±1%	319	26	30.85	16500	193.28
			±2%	319	82	6	17148	143.84
			±3%	319	327	0.66	33396	162.96
			±5%	319	156	3.14	67381	206.08

It is worth mentioning that the parameters for the strain amplitude of ±3% are the ones obtained from the companion method test because the model exhibited better agreement with the experimental data than that of the multiple-step method.

It should be noted that the parameters tend to vary with each type of coupon even at the same strain amplitude.

The sensitivity analysis in section 6.2, not only helps to establish the criteria to round and display the values, but also serves as a base point to perform comparisons between different sets of values.

The values in table 31 are compared with the values obtained in previous studies that are shown in table 3.

In general, the parameters have the same order of magnitude with some exceptions in the isotropic hardening parameters (Q_{∞} and b). This may be due to the fact that the data is extracted from only 10 cycles and not enough accumulated plastic strain has been developed to construct the complete exponential curve. Nevertheless, this affects the simulation when a higher number of cycles is applied to the specimen.

6.4. Results discussion

In the previous section, results are shown from figure 94 to figure 100. In general, the obtained FE models are in good agreement with the experimental results, and in tables 23 to 29, the similarity between the FE models and the experiments is quantified by calculating the ratio σ_{FE}/σ_{exp} for each cycle. It is noted that the models that better fit their experimental counterparts are the models corresponding to strain amplitudes of $\pm 2\%$ and $\pm 1\%$ (fig. 97 and fig. 98 respectively).

At lower strains, the numerical model results are very sensitive to the parameter $\sigma|_0$ from the isotropic component. This value takes into account the linear range of the material behaviour and, for stainless steel, its effect is more variable. A more detailed study about the effect of this parameter is proposed for future research.

At higher strains, the degree of roundedness and the shape of the curve is simulated successfully, nonetheless, the peak stresses ratio shows larger discrepancies.

7. CONCLUSIONS AND RECOMMENDATIONS

In this chapter, final conclusions regarding the experimental tests and its comparison with the numerical simulations are presented. Subsequently, recommendations for future research are given.

7.1. Conclusions

In order to introduce stainless steel in earthquake-resistant structures, it is necessary to comprehend its cyclic plasticity when subjected to a small number of large displacements. In order to accomplish this, an extensive study considering both experimental investigations and numerical modelling is necessary.

For this reason, the main objective of this work consisted of understanding the cyclic behaviour and low-cycle fatigue of austenitic stainless steel by performing experimental tests, and identifying an analytical model that adequately simulates its behaviour. The material studied was 1.4301 austenitic stainless steel, which was subjected to experimental tests performed in the Structural Technology Laboratory in the Department of Civil and Environmental Engineering at UPC.

After a literature review, it was observed that a combined Isotropic/kinematic hardening model known as Chaboche model was the best suited for simulating the cyclic plasticity of non-linear materials such as stainless steels.

The tests performed were low-cycle fatigue tests using companion method and multiple-step method. Two tests were executed at strain amplitude of $\pm 5\%$ and $\pm 3\%$ using the companion method and one test was executed using multiple-step method going through strain amplitudes of $\pm 0.5\%$, $\pm 0.75\%$, $\pm 1\%$, $\pm 2\%$, $\pm 3\%$, $\pm 4\%$. Also, a monotonic axial tensile test was made in order to obtain general properties of the material. The development of these test is presented in chapter 4 and their results in chapter 5.

As a conclusion regarding the tests, first, it is worth mentioning that the cyclic tests were complex, and instrumentation is an important aspect to take into account and can be determinant to the correct development of the cyclic tests. Second, in chapter 5, the results obtained were, in general, satisfactory; although the obtained data was affected by premature failure of the strain gauge. Regarding the mechanical behaviour, stainless steel showed a considerable level of cyclic hardening that increases with strain amplitude and as well as an asymmetric behaviour. It was also observed that at constant strain amplitude, the displacement amplitude increases with each cycle and also deviates from the axis.

In addition to the experimental tests, numerical finite element models were necessary to adequately fulfil the objectives of this study, these models were performed using the general-purpose Software Abaqus. Before executing the numerical models, a convergence study was employed in order to acquire the finite element best suited for the analyses.

With the experimental results, it was possible to extract necessary data to define an analytical model and simulate the material using Abaqus. The FE models were executed and the results are shown in chapter 6. It was determined that the models were in good agreement with the experimental results and formerly the analytical parameters that simulate the material behaviour were proposed. With this parameters (see table 31), further researchers will be able to perform numerical simulations of a similar material without the need to perform tests.

Table31. Proposed parameter values.

Steel Grade	Young's Modulus (N/mm ²)	Yield Strength (N/mm ²)	Amplitude (%)	Combined hardening parameters				
				$\sigma _0$ (N/mm ²)	Q_∞ (N/mm ²)	b	C_k (N/mm ²)	γ_k
EN 1.4301	196119	319	±0.5%	319	25	198.28	27736	312.57
			±0.75%	319	24	269.61	20649	258.73
			±1%	319	26	30.85	16500	193.28
			±2%	319	82	6	17148	143.84
			±3%	319	327	0.66	33396	162.96
			±5%	319	156	3.14	67381	206.08

It is worth noticing that in order to correctly predict the material behaviour, it is necessary to anticipate the strain range in the analysis and use the parameters corresponding to that anticipated strain range.

In the next section, general recommendations are presented.

7.2. Recommendations for future research

Now as this line of research has taken its first steps in the UPC, it is highly recommended that the tests are repeated with larger number of coupons in order to expand the currently limited data about the cyclic plasticity and low-cycle fatigue of austenitic stainless steel.

It is worth to take into account different types of coupons with different material like flat coupon of cold formed stainless steel, and also perform both axial and bending low-fatigue tests.

An additional suggestion is regarding the instrumentation. The devices used in the experimental test must be selected with great care, especially the strain gauges. It is important to employ post yield strain gauges that are able to resist fatigue at strain amplitudes of around ±7%.

It is highly recommended that the companion method is used to obtain representative data of the cyclic behaviour of stainless steel and to adequately obtain data for the analytical models.

References

- [1] Steel Construction Institute. *Design Manual for Stainless Steel*. Fourth Edition. 2017. ISBN 978-1-85942-233-5.
- [2] Nip, K., Gardner, L., Davies, C., & Elghazouli, A. (2010). Extremely low cycle fatigue tests on structural carbon steel and stainless steel. *Journal of Constructional Steel Research*, 66(1), 96-110.
- [3] Zhou, F., & Li, L. (2016). Experimental study on hysteretic behavior of structural stainless steels under cyclic loading. *Journal of Constructional Steel Research*, 122, 94-109.
- [4] Steel Construction Institute. *Design Manual for Stainless Steel - Commentary*. Third Edition. 2007.
- [5] European Committee for Standardization. (2015). *EN 10088-1 Stainless steels - Part 1: List of stainless steels*.
- [6] European Committee for Standardization. (2006). *EN 1993-1-4 Eurocode 3. Design of steel structures. Part 1-4: General rules. Supplementary rules for stainless steel*.
- [7] International Stainless Steel Forum. *Stainless steels for lecturers and students of architecture and civil engineering*. Retrieved 2017, from <http://www.worldstainless.org/training/Architecture%20and%20Civil%20Engineering>.
- [8] SCI Steel Knowledge. (2010). *Cala Galdana Bridge*. Retrieved 2018, from <http://www.worldstainless.org/news/show/365>.
- [9] Nickel Institute. (2002). *Compost Building Uses Stainless Steel*. Retrieved 2017 from <https://www.nickelinstitute.org/NickelUseInSociety/MaterialsSelectionAndUse/ArchitectureBuildingAndConstruction/CompostBuildingUsesStainless.aspx>.
- [10] Arrayago, I., Real, E. and Gardner, L. (2015). Description of stress-strain curves for stainless steel alloys. *Materials and Design*, 87, 540–552.
- [11] Ramberg, W., & Osgood, W. (1943). Description of stress-strain curves by three parameters. *Technical Note No. 902*. Washington, D.C., USA: National Advisory Committee for Aeronautics.
- [12] Hill, H. (1944). Determination of stress-strain relations from "offset" yield strength values. *Technical Note No. 927*. Washington, D.C., USA: National Advisory Committee for Aeronautics.
- [13] Mirambell, E. and Real, E. (2000). On the calculation of deflections in structural stainless steel beams: an experimental and numerical investigation. *Journal of Constructional Steel Research*, 54 (4), 109-133.
- [14] Rasmussen, K.J.R. (2003). Full-range stress-strain curves for stainless steel alloys. *Journal of Constructional Steel Research*, 59 (1), 47-61.

- [15] Chaboche, J.L. (2008). A review of some plasticity and viscoplasticity constitutive theories., *International Journal of Plasticity*, 24(10), 1642-1693.
- [16] ABAQUS. (2015). ABAQUS/Standard user's manual and ABAQUS CAE manual. Simulia Dassault Systèmes. France.
- [17] SEI/ASCE 8-02. (2002). Specification for the design of cold-formed stainless steel structural members. American Society of Civil Engineers (ASCE), Reston, US, 2002.
- [18] AS/NZS4673. (2001). Cold-formed stainless steel structures. Sydney: Standards Australia; 2001.
- [19] ASTM. (2010). E8/E8M. Standard test methods for tension testing of metallic materials.
- [20] ASTM. (2012). E606/E606M. Standard test method for strain-controlled fatigue testing.
- [21] European Committee for Standardization. (2001). EN 10002-1. Metallic materials - Tensile testing - Part 1: Method of test at ambient temperature.
- [22] Borja, R. (2013). *Plasticity Modeling & Computation*. California: Springer.
- [23] Black, J., & Kohser, R. (2012). *DeGarmo's Materials and Processes in Manufacturing* (Eleventh Edition ed.). John Wiley & Sons.
- [24] Oliver, X., & Agelet de Saracibar, C. (2010). *Mecánica de los medios continuos para ingenieros*. Barcelona: Edicions UPC.
- [25] Schijve, J. (2009). *Fatigue of Structures and Materials*. Delf: Springer.
- [26] Coffin, J. L. (1953). A study of the effects of cyclic thermal stresses on a ductile metal. *Transactions of ASME* 1954, 76, 931-50.
- [27] Manson, S. (1954). Behavior of Materials Under Conditions of Thermal Stress. *National Advisory Commission on Aeronautics: Report 1170*. Cleveland: Lewis Flight Propulsion Laboratory.
- [28] Krawinkler, H., Zohrei, M., Lashkari-Irvani, B., Cofie, N. and Hadidi-Tamjed, H.. (1983). Recommendations for Experimental Studies on the Seismic Behavior of Steel Components and Materials. *John A. Blume Earthquake Engineering Center Technical Report 61*. Stanford Digital Repository.
- [29] Stephens, R., Fatemi, A., Stephens, R., & Fuchs, H. (2000). *Metal Fatigue in Engineering*. New York: John Wiley & Sons.
- [30] Dahlberg, M., & Segle, P. (2010). Evaluation of models for cyclic plastic deformation - A literature study. SSM Research report 2010:45. Swedish Radiation Safety Authority.
- [31] Jiang, Y., & Sehitoglu, H. (1994). Cyclic ratcheting of 1070 steel under multiaxial stress states. *International Journal of Plasticity*, 10, 579-608.

- [32] Mahmoudi, A., Badnava, H., & Pezeshki-Najafabadi, S. (2011). An application of Chaboche model to predict uniaxial and multiaxial ratcheting. *Engineering Procedia*, 10, 1924-1929.
- [33] Shakeri, A. (2017). Isotropic-Kinematic Cyclic Hardening Characteristics of Plate Steels. *International Journal of Steel Structures*, 17(1), 19-30.
- [34] Roy, S., Goyal, S., Sandhya, R., & Ray, S. (2013). Analysis of Hysteresis Loops of 316L(N) Stainless Steel under Low Cycle Fatigue Loading Conditions. *Procedia engineering*, 55, 165-170.
- [35] Wang, Y., Chang, T., Shi, Y., Yang, L., & Liao, D. (2014). Experimental study on the constitutive relation of austenitic stainless steel S31608 under monotonic and cyclic loading. *Thin-Walled Structures*, 83, 19-27.
- [36] Dutta, A., Dhar, S., & Acharyya, S. (2010). Material characterization of SS 316 in low-cycle fatigue loading. *Journal of Materials Science*, 45(7), 1782-1789.
- [37] Chaboche, J. (2008). A review of some plasticity and viscoplasticity constitutive theories. *International Journal of Plasticity*, 24(10), 1642-1693.
- [38] L. Logan, D. (2012). *A First Course in the Finite Element Method*. Stamford: Cengage Learning.
- [39] Kleiber, M., & Oñate, E. (1999). *Archives of Computational Methods in Engineering. State of the art reviews*. Barcelona: CIMME. Vol. 6, n°2.
- [40] Tokyo Sokki Kenkyujo Co., Ltd. (2017). *Strain Gauges Catalog 2017*.
- [41] Blanco, E., Oller, S., & Gil, L. (2007). *Análisis experimental de estructuras*. Barcelona: CIMME.
- [42] *Wikimedia Commons*. (s.f.). Retrieved 2018 from <https://commons.wikimedia.org/wiki/File:StrainGaugeVisualization.svg>.
- [43] Huang, Y., & Young, B. (2014). The art of coupon tests. *Journal of Constructional Steel Research*, 96, 159-175.
- [44] Westeel, R. (2012). Análisis Comparativo De Expresiones Analíticas para Modelizar El Comportamiento Tenso-Deformacional No Lineal Del Acero Inoxidable. Universitat Politècnica de Catalunya, Barcelona.
- [45] Both, I., Zub, C., Stratan, A., & Dubina, D. (2017). Cyclic behaviour of European carbon steels. *ce/papers*, 1. 3173-3180. EUROSTEEL 2017, Copenhagen, Denmark.
- [46] *Visualization of the working concept behind the strain gauge on a beam under exaggerated bending*. (s.f.). Retrieved 2018 from https://en.wikipedia.org/wiki/Strain_gauge#/media/File:StrainGaugeVisualization.svg.